N° d'ordre 05 ISAL 0076 Année 2005

Thèse

Synthèse de réponse impulsionnelle en imagerie ultrasonore pour l'estimation vectorielle du deplacement

Impulse response synthesis in ultrasound imaging for vectorial displacement estimation.

présentée devant
L'Institut National des Sciences Appliquées de Lyon

Le 18 octobre 2005

pour obtenir
le grade de docteur

Ecole doctorale : Mécanique Energie Génie-Civil Acoustique

Spécialité : Acoustique
par
Hervé LIEBGOTT

Jury

DELACHARTRE Philippe	Directeur
HARBA Rachid	Rapporteur
JENSEN Jørgen A.	Rapporteur
JUTTEN Christian	Rapporteur
POURCELOT Léandre	Président
VRAY Dider	Directeur
WILHJELM Jens E.	Directeur

Remerciements

Tout d'abord je tiens à remercier les professeurs Rachid Harba, Christian Jutten et Jørgen A. Jensen qui ont été rapporteurs de ma thèse. Le temps qu'ils ont passé à la lecture de la thèse et leurs remarques m'ont permis d'enrichir le manuscrit. Je remercie le professeur Léandre Pourcelot pour avoir accepté d'être membre de mon jury.

Ces trois années de thèse ont été pour moi l'occasion de travailler avec des gens extraordinaires que je souhaite remercier.

J'aimerais également dire un grand merci à Philippe Delachartre qui m'a encadré pendant ces trois années. Il a été le formateur dont j'avais besoin. Il a su me communiquer sa passion pour l'imagerie ultrasonore tout en m'inculquant méthode et rigueur. Au delà du travail scientifique, j'ai aussi apprécié ses qualités humaines en particulier lors de ses visites au Danemark.

Je tiens encore à remercier le professeur Didier Vray, responsable de l'équipe Imagerie Ultrasonore du CREATIS qui a aussi participé à l'encadrement de mon travail.

During my PhD I have had the opportunity to work during two periods of three months each at the Technical University of Denmark. I would like to thank Jens E. Wilhjelm who has supervised my work during my stays in Lyngby. It has been a great chance to meet him. He has made my integration in the research group at the department extremely easy. The energy he has used for translating my written communications into real English has also been really valuable.

I also would like to thank Professor Jørgen A. Jensen head of the Center for Fast Ultrasound Imaging for the opportunity he has given me to work with the RASMUS scanner. I have also learned a lot thanks to the Wednesday meetings and to his expertise in the domain of ultrasound imaging.

I would like to thank all members of the center, Morten, Kim, Svetoslav, Louise, Malene, Niels and Jacob with whom it was nice to speak about ultrasound, or have more cultural discussion… I also would like to thank Borislav with whom I shared office during my second stay at DTU. I am also grateful to Henrik Laursen who always found solutions for my informatics problems.

I would like to thank particularly Fredrick Gran and Jesper Udesen, the co-inventors with me of a new method called the « Propagating circles ». More than a scientific collaboration is born during my stay in Denmark, and a real friendship is born with Fredrick, Jesper, Cillia, Lisbeth and her family.

Tak!

J'aimerais remercier l'ensemble des membres du CREATIS. Tout d'abord Isabelle Magnin directrice du centre qui m'a accueilli depuis mon DEA en 2002. L'ensemble des permanents, et plus particulièrement Christian, Olivier, Denis, et Elisabeth membres de l'équipe Imagerie Ultrasonore, ainsi que Marc qui a souvent su faire preuve de patience.

Je souhaite remercier l'ensemble des doctorants qui font l'ambiance des pauses café, par ordre d'apparition: Jérémie, Julien, Sabin, Jean Martial, Ghada, Bruno, Vilo, Bud, So, Simone et les autres… avec qui nous avons partagé de grands moments.

Je n'oublie pas André et Sébastien qui m'ont toujours dépanné en cas de soucis matériel, ainsi que l'ensemble de l'équipe informatique. De même j'adresse mes remerciements à l'ensemble du secrétariat qui sait me redonner le sourire quand j'en ai besoin.

J'aimerais dire un grand merci à tous mes colloques. La vie de notre petite famille du 1 rue de Bruxelles prend fin en même temps que cette thèse, mais ça aura été une très belle histoire. Merci Rémoche, Mathilde, Mathias, Braloux, Katia, Eric, JD et Nicolas. Et bonne chance au Japon à Aurélie et Adrien.

Je souhaite également remercier l'ensemble de ma famille pour son soutien et la confiance qu'ils m'ont toujours témoignée.

Je remercie Colette pour ses Kougelhof.

Enfin j'adresse toute ma gratitude à Julie. Elle a toujours été à mes côtés durant cette période, pendant laquelle le stress et le travail ne m'ont sans doute pas rendu aussi disponible qu'elle l'aurait souhaité.

Ce travail de thèse et en particulier mon échange au Danemark ont été possible grâce aux aides financières de la Région Rhône Alpes, du ministère de l'Education Nationale, du Programme Lavoisier du ministère des Affaires Etrangères et du Service de Coopération Universitaire et Scientifique de l'Ambassade de France Au Danemark dirigé par Patrick Nedellec.

Et que ceux que j'aurais oubliés acceptent mes plus plates excuses.

Nomenclature

x, y, z :	spatial variables, lateral, axial and azimuthal respectively
$\otimes$	tensorial product
$\mathbf{A}^T$	is the transposition of $\mathbf{A}$ according to tensorial algebra
grad	is the gradient operator
$\sigma_{i,j}$	is the component of the stress tensor situated in line i and column j
λ and μ	are the Lamé constants
E	is the Young's modulus
ν	is the Poisson's ratio
$d(x, y, z)$	is a spatial distribution of scatterers
$h(x, y, z)$	is the spatial point spread function (PSF)
$r(x, y)$	is the reference image
$s(x, y)$	is the strain images
$\tilde{r}(x)$	is the complex lateral rafio frequency signal (RF) associated to $r(x)$
$\boldsymbol{\Delta} = [\Delta x, \Delta y]$	is the 2D displacement field
$\hat{\boldsymbol{\Delta}} = \left[\hat{\Delta} x, \hat{\Delta} y\right]$	is the estimated 2D displacement field
$\underset{x,y,z}{\otimes}$	is the convolution over the variables x, y and z
u, v, w :	are the spatial frequencies associated with x, y, z
$F\{g(x)\}$:	is the Fourier transform of the function $g(x)$
$H\{g(x)\}$:	is the Hilbert transform of the function $g(x)$
$H_x\{g(x, y)\}$:	is the Hilbert transform in the direction x of the image $g(x, y)$
$R_{rs}(X)$:	is the classical correlation
$\tilde{R}_{rs}(X)$:	is the complex cross-correlation
$\tilde{R}_{rr}(X)$:	is the complex auto-correlation
$\Phi\left(\tilde{R}_{rs}(X)\right)$:	is the phase of the complex correlation
$\left\|\tilde{R}_{rs}(X)\right\|$: I	is the envelope of the complex correlation
$P_{\tilde{r}}(u)$:	is the spectral density

Content

Résumé en Français

Introduction

L'élastographie ultrasonore est une méthode d'imagerie médicale basée sur l'échographie et dont le but est de fournir au médecin une image des caractéristiques élastiques du milieu. Bien entendu on pense naturellement au module d'Young qui représente la dureté du milieu. Mais tout autre paramètre d'élasticité, dont le lien avec le développement de certaines pathologies a été montré, serait un bon candidat. On peut citer entre autres le cancer du sein pour lequel des nodules plus rigides que le reste du sein se développent. On pourrait alors utiliser l'eslastographie pour la détection précoce de ces nodules dès leur apparition. Ou dans le cas de la plaque d'arteriosclérose pour laquelle l'élastographie serait un complément diagnostique. Elle permettrait surtout d'évaluer le risque de rupture de la plaque. En effet ce risque est fortement lié au contraste d'élasticité entre la plaque et l'artère elle-même.

L'approche choisie dans ce travail est celle dite statique, telle que présentée par Ophir dans [1]. Deux images d'un même milieu sont acquises, l'une lorsque le milieu est au repos, l'autre après l'avoir soumis à une contrainte mécanique externe. Par traitement du signal et de l'image on estime le déplacement ou la déformation au sein du milieu.

Les images du déplacement ou de la déformation peuvent être directement interprêtées, elles donnent en effet une information sur la dureté locale du milieu : un milieu plus dur se déforme moins qu'un milieu mou. Mais une image quantifiée d'un paramètre absolu tel que le module d'Young serait une information bien plus simple à interpréter pour le médecin.

Une des difficultés majeure pour l'élastographie réside dans l'estimation précise de la composante latérale du déplacement ou de la déformation. L'image ultrasonore conventionelle conduit à une importante différence de précision entre le déplacement axial estimé et le déplacement latéral.

La contribution principale de cette thèse se situe dans l'approche faite du problème. Alors que l'ensemble de la communauté utilise des images conventionelles délivrées par des échographes commerciaux, nous nous intéressons à la formation de l'image. On va même plus loin, en intervenant sur le système d'imagerie, en l'adaptant, et en synthétisant une réponse impulsionelle dédiée pour l'estimation latérale du déplacement. On montre que cette approche permet d'augmenter grandement la précision de l'estimation latérale du déplacement.

La thèse se compose de 4 chapîtres et d'une conclusion.

Chapitre 1 : Etat de l'art

Le chapitre 1 de cette thèse, après une courte introduction, présente la motivation clinique de notre projet.

La deuxième partie de ce chapitre présente les notions de mécanique permettant de comprendre le comportement d'un solide élastique linéaire soumis à une contrainte externe. Le tenseur des déformations est relié au tenseur des contraintes par le tenseur d'élasticité (1-3). Le tenseur d'élasticité

fait intervenir les constantes de Lamé (1-4) qui sont elles-même liées au module d'Young et au coefficient de Poisson par les relations (1-5) et (1-6). La loi d'équilibre de Newton permet d'exprimer le problème direct d'élasticité. Dans cette partie on note l'importance d'une connaissance de plusieurs composantes de déplacement ou de déformation pour bien définir le problème d'élasticité qui est clairement multidimensionnel comme le montrent les équations (1-10) et (1-11).

La troisième, et plus importante partie de ce chapitre présente un ensemble des méthodes d'estimation de mouvement en traitement du signal et de l'image, qui ont déjà été présentées dans la littérature. Les méthodes de mise en correspondance par blocs (block mathcing) sont présentées, les méthodes de rayons multiples, de flow optique et enfin les méthodes dites de phase latérale.

Le principe des méthodes de mise en correspondance par blocs est de sélectionner un motif dans une image de départ et de retrouver sa position dans l'image du milieu déformé en comparant le bloc initial à un certain nombre de blocs dans une région d'intérêt de la deuxième image. La taille des blocs[2], le critère de ressemblance ou de dissemblance utilisé [3], le type de données utilisées (Radio Fréquence (RF) ou enveloppe) [4], certaines limites ou solutions générales ainsi que de récentes application des méthodes de *block matching* en échographie sont présentées[5] [6]. Le principe de la méthode est donné Figure 1-1.

Dans les méthodes à rayons multiples, une même partie du milieu est imagée sous différents angles de tir. On effectue ensuite des estimations 1D le long de chaque angle de tir, et l'information issue de chaque estimation est combinée avec celle des autres angles pour projeter le déplacement total sur les deux axes principaux de l'image ultrasonore. Cette méthode a été utilisée par Tanter *et.al*. [7], et Jensen a utilisé une méthode que l'on peut également classer ici dans[8] et [9]. Cette approche est illustrée Figure 1-3.

Dans le flow optique, l'idée de base est de considérer le niveau de gris d'un pixel constant au cours du temps, ou constant pour plusieurs acquisitions [10]. On suit en quelque sorte les motifs entre les images. Cette condition n'est pas suffisante pour estimer le déplacement. Il faut introduire une condition supplémentaire. Une hypothèse souvent utilisée est la *contrainte de lissage.* Cette contrainte exprime le fait que la variation de déplacement est lente entre deux pixels voisins, ainsi les discontinuités sont évitées. L'estimation du flow optique se fait par combinaison de ces deux contraintes.

Enfin ce chapitre présente les méthodes de *phase latérale.* Il s'agit là d'introduire dans la direction latérale de l'image une notion de phase, du même type que celle des signaux Radio Fréquences (RF) composant les colonnes des images ultrasonores conventionnelles. C'est ainsi que des oscillations latérales ont été utilisées pour l'estimation des vitesses du sang [11]. Plus récemment, une phase latérale synthétique a été introduite dans des images échographiques dans le cadre d'une étude sur l'élastographie [12]. Des signaux complexes latéraux ont été calculés à partir d'images ultrasonores RF conventionnelles.

Ces dernières méthodes sont très intéressantes et ont été le point de départ de notre travail.

Chapitre 2 : Imagerie ultrasonore et formation de voies

Dans ce chapitre les notions liées à la formation de l'image échographique, et les notions de formation de voies sont présentées.

L'imagerie échographique se passe en deux phases principales : une phase d'émission et une autre de réception. Tout d'abord une onde acoustique est générée par un transducteur piézoélectrique excité par un signal électrique. L'onde se propage dans le milieu et la présence d'hétérogénéités dans le milieu conduit à la génération d'échos. Ces échos se propagent à leur tour dans le milieu, et ils sont détectés par le transducteur ultrasonore, qui, à la fin de l'émission, est passé en mode réception. Il est donc « à l'écoute » des échos provenant du milieu. Le signal reçu par le transducteur est amplifié et démodulé. Ce signal donne une information sur la géométrie du milieu. En effet l'échelle de temps, qui correspond à l'instant d'arrivée des échos permet, si on considère la vitesse des ultrasons constante dans le milieu, de donner une information sur la profondeur des structures qui ont généré les échos. L'amplitude des échos donne une information sur l'échogénéité locale dans le milieu. Ce signal de base s'appelle une ligne A, ou, s'il n'est pas démodulé, signal RF. Ce principe est donné Figure 2-1.

Lorsque le transducteur est fixe et le milieu est en mouvements on peut faire une image mode M (comme mouvement) ou l'on voit la profondeur des échos, et par conséquent celle des structures anatomiques, varier au cours du temps. Si par contre on translate le transducteur au dessus d'un milieu immobile, on fait une image mode B (comme brillance) qui est l'image échographique classique. On peut voir une image mode M sur la Figure 2-2 et une image mode B sur la Figure 2-3.

La formation de l'image, telle qu'elle a été décrite ici, peut également s'écrire sous la forme d'une équation de convolution faisant apparaître la réponse impulsionnelle du système (il s'agit de l'image obtenue lorsque l'on image une hétérogénéité ponctuelle unique) et la distribution des hétérogénéités dans le milieu (2-6). Une réponse impulsionnelle est donnée Figure 2-9. Cette convolution est limitée aux parties du milieu où la réponse impulsionnelle peut être considérée constante. Ce modèle linéaire permet également de donner simplement la forme d'une image d'un même milieu qui aurait subit une translation rigide, équation (2-12).

L'obtention de ligne A, qui se faisait au départ avec un transducteur unique, se fait aujourd'hui avec des transducteurs comportant plusieurs éléments. On utilise réellement des antennes acoustiques. Plusieurs éléments sont excités à des instants séparés par une certaine loi de retard, afin de focaliser l'énergie émise dans une région du milieu. En réception il s'agit de sommer les contributions de l'ensemble des éléments. En pondérant en plus les contributions de chaque élément, on peut agir sur la forme de la réponse impulsionnelle du système, il s'agit du principe de la formation de voies qui dans le cas de l'onde émise est représenté Figure 2-7. Suivant les applications envisagées, on ne souhaite pas forcément les mêmes caractéristiques de réponse impulsionnelle. Il s'agit alors de choisir judicieusement les paramètres du formateur de voies.

Nous présentons dans ce chapitre une méthode permettant de contrôler la forme de la réponse impulsionnelle à partir d'une fonction d'ouverture en réception. Cette méthode est basée sur le principe de réciprocité [13] [14]. Il suffit de calculer, à la position des éléments de la sonde, le profil de pression produit par une sonde qui serait placée à la profondeur d'étude. La pondération utilisée pour cette sonde est le profil de pression espéré. Il s'agit en fait de *rétro-propager* le profil de pression souhaité. Il est important de noter que le résultat obtenu dépend de la profondeur d'exploration à laquelle on se situe.

On donne également les résultats de l'approximation de Fraunhofer [15]. Cette approximation conduit à une relation de transformée de Fourier entre le champ acoustique et la fonction d'ouverture de la sonde. C'est une approximation qui n'est valable que dans la zone focale de la sonde. Cette approche bien que moins précise, comme nous le montrons à travers une simulation, permet toutefois d'interpréter simplement les résultats obtenus lors de la conception d'un formateur de voies.

Une comparaison entre les deux approches de conception du formateur de voies est donnée Figure 2-12 et Figure 2-14.

Pour finir, la validation globale de notre approche système est présentée. Il s'agit d'une comparaison entre des images obtenues avec le logiciel de simulation d'images échographiques Field II développé par Jensen [16], et les images obtenues grâce à notre approche, Figure 2-18 et Figure 2-19. On montre que lorsque la réponse impulsionnelle est contrôlée, les deux approches donnent des images très ressemblantes. Les différences qui subsistent viennent de la difficulté à donner une expression analytique exacte de la réponse impulsionnelle.

Chapitre 3 : Estimation latérale du déplacement par une méthode 2 fois 1D

Ce chapitre présente réellement le cœur de la thèse et du travail effectué. L'articulation se fait de la manière suivante. On montre comment le choix d'un estimateur spécifique du déplacement latéral conduit à modifier la formation de l'image échographique. On montre qu'une réponse impulsionnelle présentant des oscillations latérales est mieux adaptée à l'estimation latérale du déplacement qu'une réponse impulsionnelle conventionnelle.

On choisit dans un premier temps de s'intéresser aux signaux latéraux d'une image ultrasonore. C'est à partir ce ces signaux que l'on va estimer le déplacement latéral entre les images échographiques.

On se fixe également d'estimer le déplacement latéral à partir de la phase de l'intercorrelation complexe entre le signal de référence et le signal déformé. Il s'agira alors de rechercher le passage à zéro de cette phase. En effet on sait qu'elle est nulle pour la valeur de déplacement recherchée. La position de ce passage à zéro correspond également à la position du maximum de la corrélation réelle. C'est une approche qui a déjà été utilisée dans la littérature pour la direction axiale de l'image ultrasonore [17] et dont la précision, bien en dessous de la taille d'un pixel nous laisse envisager de bons résultats pour l'estimation latérale du déplacement.

La position du passage à zéro est estimée grâce à une méthode itérative de Newton dont le principe est rappelé Figure 3-1.

Afin « d'optimiser » l'estimation du déplacement on choisit une expression de l'intercorrélation complexe entre les signaux latéraux présentant une phase linéaire. On s'intéresse ensuite aux conséquences d'un tel choix sur les signaux RF latéraux, et sur le profil latéral de la réponse impulsionnelle. On montre ainsi que la réponse impulsionnelle adaptée présente des oscillations latérales dont la longueur d'onde est inversement proportionnelle à la pente de la phase de la corrélation complexe. L'expression du profil latéral de la réponse impulsionnelle est donnée dans l'équation (3-25). Elle est illustrée Figure 3-3 ainsi que la fonction d'ouverture qui permet de l'obtenir. Il s'agit d'une fonction d'ouverture présentant deux pics dont l'écartement est proportionnel à la fréquence spatiale des oscillations latérales et dont la largeur est inversement proportionnelle à la largeur de l'enveloppe de la réponse impulsionnelle comme l'exprime les équations (3-27) et (3-28).

Quelques résultats de simulations illustrent les différences majeures entre la nouvelle réponse impulsionnelle et une réponse impulsionnelle conventionnelle. En particulier on montre le module et la phase de l'autocorrélation complexe du profil latéral de la réponse impulsionnelle (3-10). On remarque en particulier que la pente de la phase dans le cas de la nouvelle réponse impulsionnelle est plus raide ce qui devrait conduire à une meilleure estimation de la position du passage à zéro. Ce

résultat est confirmé par une étude de la qualité de l'estimation en présence de bruit illustrée Figure 3-11 et Figure 3-12. Dans le cas de la réponse impulsionnelle adaptée l'écart type de l'estimé est diminué d'un facteur 9.

L'ensemble de la méthodologie mise en place pour intégrer l'estimation du déplacement latéral dans un schéma permettant de faire une estimation des deux composantes du vecteur déplacement est ensuite présenté. Il s'agit d'une approche deux fois 1D. Le déplacement axial est estimé à partir d'images conventionnelles. Le déplacement latéral est estimé à partir d'images adaptées obtenues grâce à notre formateur de voies et une démodulation hétérodyne [18] qui permet de supprimer les oscillations axiales qui étaient encore présentes dans l'image. Le principe de cette démodulation est rappelé et illustré Figure 3-17 et Figure 3-18. Un fenêtrage adaptatif est mis en place qui permet le suivit entre les images d'une même zone du milieu.

La démarche permettant de choisir l'ensemble des paramètres du formateur de voies et de la méthode d'estimation du déplacement est ensuite donnée.

Les paramètres d'imagerie sont limités par la taille de la sonde utilisée. Un compromis doit être réalisé entre la longueur d'onde des oscillations latérales et la largeur de l'enveloppe gaussienne de la réponse impulsionnelle. On montre que les deux paramètres ont une influence sur la qualité du résultat Figure 3-19, Figure 3-20 et Figure 3-21. Dans notre cas, la longueur d'onde des oscillations latérales est fixée à λ_x=2.6 mm et la largeur à mi hauteur de l'enveloppe gaussienne est à σ_x=2.8mm.

Les paramètres élastiques du milieu sont choisis pour être assez proches de ceux trouvés dans la littérature pour les tissus biologiques, un cœfficient de poisson de 0.49 et un module d'Young variant entre 50 et 500kPa. Le milieu considéré contient une inclusion rigide en son centre comme le montre la Figure 3-22.

La taille des fenêtres d'estimation est également choisie de manière à minimiser à la fois l'erreur quadratique de l'estimation et le nombre de points aberrants ce qui est illustré sur les Figure 3-23, Figure 3-25 et Figure 3-26.

Une comparaison des résultats obtenus en simulation sur des images conventionnelle et sur des images adaptées est réalisée. Les résultats sont donnés sous forme de vecteur Figure 3-28, Figure 3-29 et Figure 3-30 ou sous forme de cartes de déplacement Figure 3-31 et Figure 3-32. Les cartes d'erreur sont données Figure 3-33 et Figure 3-34 ainsi que les histogrammes des erreurs Figure 3-35 et Figure 3-36. L'amélioration de l'estimation grâce à l'utilisation d'images adaptées se traduit par une diminution d'un facteur 3 de l'écart type de l'histogramme des erreurs latérales.

Pour finir ce chapitre on montre quels seraient les résultats si les mêmes charactérstiques d'oscillations que dans la direction axiale pouvaient être obtenues dans la direction latérale de l'image. On montre qu'on a alors la même précision pour l'estimation axiale et latérale avec des histogrammes d'erreur présentant une même distribution Figure 3-45 . On donne enfin les caractéristiques que devraient avoir une sonde permettant d'obtenir ce genre de réponses impulsionnelles et en particulier la fonction d'ouverture qu'il faudrait utiliser Figure 3-46. Le nombre d'élément mis en jeu (plus de 500) dépasse largement le nombre d'éléments utilisé dans les sondes commerciales actuelles.

Chapitre 4 : Résultats expérimentaux

Dans ce chapitre la mise en pratique de la méthode proposée est étudiée.

Notre méthode nécessite l'accès à l'ensemble des données brutes de l'échographe. Peu de plateformes d'imagerie permettent l'accès à ce type de données. Nous avons réalisé les acquisitions dans le cadre d'une collaboration avec un laboratoire de l'Université Technique du Danemark.

L'échographe expérimental utilisé (RASMUS [19]) est tout d'abord présenté, ainsi que l'ensemble de la manipulation. La Figure 4-1 montre l'interconnexion des éléments de la manipulation.

Pour réaliser nos fantômes nous utilisons du cryogel qui est un matériau dont les caractéristiques élastiques sont contrôlées en fonction du nombre de cycles de congélation-décongélation [20]. Nous avons fabriqué un fantôme en cryogel de forme parallélépipédique contenant une inclusion rigide de forme cylindrique en son centre.

Deux séries d'acquisitions ont été réalisées. L'une consiste en une simple translation latérale de la sonde au dessus du fantôme immergé dans l'eau. Cela nous a permis de valider notre approche pour un mouvement purement latéral. Ceci permet d'éviter toute erreur qui serait liée à un mouvement axial du milieu.

La deuxième série d'acquisitions a consisté en une compression directe du fantôme avec la sonde échographique.

Les résultats expérimentaux sont tout à fait cohérents et une amélioration de l'estimation grâce aux images adaptées, par rapport aux images conventionnelles est mise en évidence. L'amélioration peut être quantifiée pour l'acquisition comportant uniquement un déplacement latéral de la sonde par rapport au fantôme. Dans ce cas l'écart type de l'erreur est plus de 7 fois inférieur dans le cas des images avec modulations latérales, Figure 4-9.

Pour les acquisitions avec compression du fantôme les appréciations ne peuvent être que qualitatives. Cependant la carte de déplacement latéral obtenue sur les images avec oscillations latérales ne présente pas de points incohérents, contrairement aux résultas obtenus avec les images conventionnelles Figure 4-12 pour lesquelles on observe quelques *accidents* d'estimation. Ces points sont incohérents dans le sens ou une pression verticale appliquée au milieu entraîne un mouvement du fantôme vers les côtés du fantôme. Or, les points incohérents semblent s'être déplacés vers l'intérieur du fantôme.

La faisabilité expérimentale de la méthode est validée et cette étude nous permet d'envisager de très bons résultats si le matériel peut d'avantage s'adapter à nos exigences.

Conclusion et perspectives

Dans cette thèse une nouvelle méthode d'estimation de plusieurs composantes du champ de déplacement entre deux images échographiques a été présentée.

Nous avons montré que l'estimation latérale du déplacement à partir de la phase de la corrélation complexe peut être grandement améliorée en agissant sur la formation des images échographiques. Une réponse impulsionnelle adaptée, présentant des oscillations latérales est utilisée. On l'obtient par formation de voies en réception. Les paramètres du formateur de voies sont déterminés grâce à une méthode simple mettant en jeu le principe de réciprocité et le concept de rétro-propagation.

L'estimation latérale du déplacement est intégrée dans une méthode deux fois 1D d'estimation du déplacement. Des résultats de simulation réaliste (avec les paramètres d'une sonde réelle) avec des

oscillations latérales sont confrontés aux résultas obtenus avec des images conventionnelles. Une amélioration d'un facteur 3 de la qualité de l'estimation est observée. On compare également ces résultats avec le cas où la réponse impulsionnelle serait optimisée d'avantage. On arrive alors à une précision identique pour les deux directions d'estimation. Malheureusement cela nous conduirait à l'utilisation d'une sonde très grande qui n'est pas disponible actuellement sur le marché.

Une étude expérimentale sur fantôme a été réalisée. Dans le cas d'un déplacement latéral pur l'estimation est à nouveau grandement améliorée grâce à l'utilisation des images adaptées. Les acquisitions mettant en jeu une compression directe du fantômes avec la sonde ne peuvent être appréciées que qualitativement. Mais l'absence de points incohérents nous conduit à la conclusion, encore une fois, que les oscillations latérales améliorent la qualité de l'estimation du déplacement.

Ce travail nous a permis de montrer que l'ensemble de la chaîne de traitement de l'information doit être pris en compte au moment de la conception ou de la mise au point de méthodes de traitement du signal.

Ce travail ouvre de larges perspectives. On envisage de développer un estimateur qui serait 2D et non plus deux fois 1D. Le travail sur des séquences d'images apporterait également une amélioration en termes de robustesse. On peut également envisager d'approfondir d'avantage notre connaissance des méthodes de formation de voies, en empruntant par exemple des méthodes issues du radar ou des télécommunications, afin d'optimiser encore la formation de voies, on peut citer la synthèse d'ouverture.

Introduction

This work deals with tissue elasticity imaging with ultrasound.

The aim of elastography is to provide an image of any mechanical parameter of the medium whose relation with a given pathology is clearly established. For example in breast cancer some hard inclusions can appear inside the breast. Elastography carries potential for detection and characterization of many diseases.

The basic principle of the method is to make two images of the medium under investigation. The two images are acquired at two different static compression states. Based on these images the displacement or strain field can be estimated inside the medium. From the strain or displacement field, general elasticity parameters such as *e.g.* Young's modulus or Poisson's ratio can be calculated.

In the first chapter of this thesis, the clinical motivation, the basic mechanics and the existing 2D displacement estimation methods are presented.

Chapter two recalls the principle of ultrasound imaging and beamforming.

In chapter three a method for estimating the lateral displacement between two ultrasound images is presented. The method is based on information present in the phase of the complex cross-correlation between the reference and displaced signals. The displacement is identified to the zero crossing of this phase. The use of this method leads to design a particular point spread function and the associated beamformer. This approach leads to images dedicated to lateral displacement estimation. A comparison between the use of this method on classical images and on our images is done. It shows clearly an improvement with our approach. This method is then introduced in a twice 1D scheme, which gives the 2D displacement vector. The image formation parameters, the mechanical properties of the medium and the estimation parameters are then given in order to optimize the estimation according to the physical limitations of the ultrasound probe. This is concluded with simulations using the parameters of our probe, as well as another simulation with same axial and lateral PSF that shows that the method could be even more optimized with other ultrasound probes.

In chapter four the method is tested experimentally with an experimental ultrasound scanner dedicated to research.

Finally summary conclusion and perspectives of this thesis work are given.

Chapter 1

State of the art

After presenting the clinical motivation for tissue elasticity imaging, part two of this chapter will present the basic mechanics laws in order to show the need for elasticity imaging methods to be multi dimensional. The other approaches to multi dimensional displacement estimation in ultrasound imaging will also be presented.

1.1 Clinical motivation

Many medical imaging modalities have been developed during the last century to enable the doctor to have access to information coming from inside the human body: X-ray, Ultrasound, Magnetic Resonance, PET... Originally developed to provide information about the anatomy and the functioning of the investigated body, it has been shown for many of those modalities that some other parameters of the medium can be imaged. This is known as parametric imaging.

Researchers have been focused on parameters of different nature, but one set of them seems to carry high potential for the diagnosis of many diseases. This parameter set is dealing with elasticity or more generally the mechanical properties of the medium.

Indeed, during the development of a large number of pathologies, the affected organ can show some changes in its elastic properties.

Palpation is an old diagnosis method that gives some information about tissue elasticity. However it can give relevant information only about abnormalities near the skin. Today it is still the most important way for women to detect tumors in their breast. As early detection is important, the American Cancer Society (ACS) recommends to practice, one's a month, a breast self examination based on palpation.

Different approaches for tissue elasticity imaging have been, and are still investigated. We have chosen the static approach which Ophir, in 91, has called elastography [1]. The approach uses the same principle as palpation and is very intuitive.

The medium under investigation is imaged at two different static compression states. Then the two images are processed in order to estimate any parameter characterizing the elastic properties of the medium. As the compression was supposed mono-dimensional, in the same direction as the propagation direction of ultrasound, the initial approaches estimated only the axial strain, or the axial

displacement. But, as we will show in the following part, this is not enough to completely characterize the medium.

1.2 Interest of 2D or 3D data, mechanical point of view

In this section the basics of linear elasticity are presented beginning from the notion of strain. The derivation of the strain tensor and its definition are given in Annex C.

1.2.1. Strain

The particular case of an Euclidian space coordinate system with three dimensions is considered. In this space we denote (x, y, z) the components associated to the space coordinate system $(\vec{x}, \vec{y}, \vec{z})$. The displacement vector is defined as $u = (u_x, u_y, u_z)$. Under the assumption of small deformation, the components of the strain tensor are approximated by

$$\varepsilon_{i,j} \approx \frac{1}{2}\left(\frac{\partial u_i}{\partial_j} + \frac{\partial u_j}{\partial_i}\right) \tag{1-1}$$

with $\varepsilon_{i,j}$ one term of the strain tensor $\mathbf{L}$, and i and j varying and equal successively to x, y and z. For example, $\frac{\partial u_x}{\partial y}$ is the derivative along direction y of the components of the displacement in direction x. Finally the tensor can be written

$$\mathbf{L} = \begin{bmatrix} \frac{\partial u_x}{\partial x} & \frac{1}{2}\left(\frac{\partial u_x}{\partial y} + \frac{\partial u_y}{\partial x}\right) & \frac{1}{2}\left(\frac{\partial u_x}{\partial z} + \frac{\partial u_z}{\partial x}\right) \\ \frac{1}{2}\left(\frac{\partial u_y}{\partial x} + \frac{\partial u_x}{\partial y}\right) & \frac{\partial u_y}{\partial y} & \frac{1}{2}\left(\frac{\partial u_y}{\partial z} + \frac{\partial u_z}{\partial y}\right) \\ \frac{1}{2}\left(\frac{\partial u_z}{\partial x} + \frac{\partial u_x}{\partial z}\right) & \frac{1}{2}\left(\frac{\partial u_z}{\partial y} + \frac{\partial u_y}{\partial z}\right) & \frac{\partial u_z}{\partial z} \end{bmatrix} \tag{1-2}$$

As the upper right triangle contains the same terms as the bottom left triangle this strain tensor is symmetrical.

1.2.2. Hook's law

Hook's law is a relation that makes it possible to describe the evolution of any particle inside a medium. This law gives a linear relation between stress and strain inside the medium. It is valid under its elastic limit. The elastic limit is defined as the limit under which the deformation is not permanent. The medium returns to its original state after the suppression of the stress. Hook's law is written in Einstein's convention[1] by

[1] Einsteins convention is used by the mecanics community in order lighten the expressions. Especially a summation for an indice which is present twice in the expression is not written but has to be considered.

$$\sigma_{ij} = C_{ijkl}\varepsilon_{kl} \tag{1-3}$$

where $\sigma_{i,j}$ is a term of the stress tensor $\boldsymbol{\Sigma}$ and C_{ijkl} a term of the elasticity tensor which depends only on the medium. As the strain tensor $\mathbf{L}$ is symmetrical, the stress tensor $\boldsymbol{\Sigma}$ is also symmetrical.

If the medium is considered isotropic, which means that all its mechanical characteristics are independent of its orientation, (1-3) can be written as

$$\begin{bmatrix} \sigma_{xx} \\ \sigma_{yy} \\ \sigma_{zz} \\ \sigma_{xy} \\ \sigma_{xz} \\ \sigma_{yx} \end{bmatrix} = \begin{bmatrix} \lambda+2\mu & \lambda & \lambda & 0 & 0 & 0 \\ \lambda & \lambda+2\mu & \lambda & 0 & 0 & 0 \\ \lambda & \lambda & \lambda+2\mu & 0 & 0 & 0 \\ 0 & 0 & 0 & \mu & 0 & 0 \\ 0 & 0 & 0 & 0 & \mu & 0 \\ 0 & 0 & 0 & 0 & 0 & \mu \end{bmatrix} \begin{bmatrix} \varepsilon_{xx} \\ \varepsilon_{yy} \\ \varepsilon_{zz} \\ 2\varepsilon_{xy} \\ 2\varepsilon_{xz} \\ 2\varepsilon_{yx} \end{bmatrix} \tag{1-4}$$

The constants λ and μ are the Lamé constants and represent the elasticity constants of compression and shear, respectively. More usually it is Young's Modulus E and Poisson's ratio ν that are used. A simple relation exists between those constants and the Lamé constants. This relation is

$$\lambda = \frac{\nu E}{(1+\nu)(1-2\nu)} \tag{1-5}$$

$$\mu = \frac{E}{2(1+\nu)} \tag{1-6}$$

Young's modulus represents the relation between stress and strain along the stress axis. Poisson's ratio characterizes the mass conservation between a lateral contraction and an axial elongation. ν stands between $0 \le \nu \le 0.5$. An uncompressible medium has a Poisson's ratio of 0.5.

Introducing (1-5) and (1-6) in (1-3) leads to

$$\frac{\nu E}{(1+\nu)(1-2\nu)}\varepsilon_{nn}\delta_{ij} + \frac{E}{(1+\nu)}\varepsilon_{ij} - \sigma_{ij} = 0 \tag{1-7}$$

with $\varepsilon_{nn} = \varepsilon_{xx} + \varepsilon_{yy} + \varepsilon_{zz}$ and δ_{ij} is the Kronecker symbol defined as

$$\delta_{ij} = \begin{cases} 1, \text{if } i = j \\ 0, \text{elsewhere} \end{cases} \tag{1-8}$$

If the deformations are static it is possible to use Newton's equilibrium

$$\frac{\partial \sigma_{ij}}{\partial x_i} + f_i = 0 \tag{1-9}$$

f_i is equal to the sum of the internal forces and it can be assimilated to gravity, and $x_1 = x$, $x_2 = y$ and $x_3 = z$. Finally the elasticity problem can be expressed as

$$\frac{\partial}{\partial_i}\left(\frac{\nu E}{(1+\nu)(1-2\nu)}\varepsilon_{nn}\delta_{ij} + \frac{E}{(1+\nu)}\varepsilon_{ij}\right) - f_i = 0 \tag{1-10}$$

This system describes the problem of elasticity and the way a medium is deformed with respect to the vectorial displacement field and two constants. The problem is completely determined by the boundary conditions.

The problem can be expressed directly with respect to the displacement field under the condition of small deformation by

$$\frac{\partial}{\partial_i}\left(\frac{\nu E}{(1+\nu)(1-2\nu)}\frac{\partial u_n}{\partial n}\delta_{ij} + \frac{E}{2(1+\nu)}\left(\frac{\partial u_i}{\partial_j} + \frac{\partial u_j}{\partial_i}\right)\right) - f_i = 0 \tag{1-11}$$

Beginning from Hook's law, some reconstruction methods can be built that enable to recover Young's modulus or Poisson's ratio. In [21], Nitta *et.al.* give such an example. The problem of reconstruction is clearly multi-dimensional. As a consequence considering the problem in more than just one direction, which has been the case for some years, will automatically lead to better results. An interesting article by Barbone and Bamber [22], gives some limitations associated with considering the problem of elasticity as one dimensional.

As a consequence it is necessary to estimate several components of the displacement field inside the medium under compression. Some approaches have already been tested in the literature and will be presented in the next section.

1.3 Approaches for 2D or 3D displacement estimation in ultrasound imaging

In this section we are going to present the different approaches for displacement estimation in ultrasound imaging.

Even though the theoretical framework for 3D displacement estimation using a 2D ultrasound array probe has been presented by Bonnefous in 1988 [23], in 1988 the technology was not able to provide the needed data. And it is still difficult to have access to 3D data today. Moreover problems seem to be encountered by the method presented by Bonnefous for flows that are not orthogonal to the ultrasound beam, as stated by Jensen in [24]. Hein presented in 1993 [25] an experimental setup based on a triple beam lens that was able to provide 3D displacement estimation. More recently Nitta [21] also presented a method that provides 3D displacement estimates.

Those approaches need specific ultrasound probes. Conceptually they are often similar to 2D methods, but they include one more direction. As a consequence in this section we will consider essentially 2D methods.

If the problem is considered two dimensional, x being the lateral dimension and y the axial dimension, a basic assumption in elastography, or more generally in some tissue displacement estimation, is that the image of the displaced medium $s(x,y)$ (s for strain image) is a displaced version, at least locally, of the original image, $r(x,y)$ (r for reference image) as

$$s(x,y) = r(x - \Delta x, y - \Delta y) \tag{1-12}$$

where $\Delta = [\Delta x, \Delta y]$ is the displacement vector.

This means that any pattern from the original image can be found, with of course a few differences, in the image of the displaced tissue. As a consequence, one of the most straightforward methods for estimating displacement in ultrasound is block matching.

1.3.1. Block matching techniques

The general word block matching used in image processing is often replaced by speckle tracking when it concerns ultrasound imaging. This is related to the texture, or background noise, of the ultrasound image which is called speckle. Speckle is the consequence of constructive and destructive interferences between the echoes backscattered from the investigated medium. The blocks (two-dimensional or one dimensional windows taken in an ultrasound image) contain a speckle pattern, which can also be found under the name acoustic signature.

The basic idea in block matching is to select a part of a reference image, a pattern or kernel P, and to find its position in a region of interest (ROI) from the strain image of the displaced medium. The initial block is compared to other, same sized blocks, from the ROI. The ROI is situated around the initial position of the kernel, and its size gives the limit of the maximum displacement that can be estimated.

In order to estimate the new position, the initial kernel and the one chosen in the ROI are compared with a resemblance or dissemblance criterion. This criterion indicates how much two blocks are identical or different. This basic principle is illustrated in
Figure 1-1, with a 2D kernel and a 2D ROI.

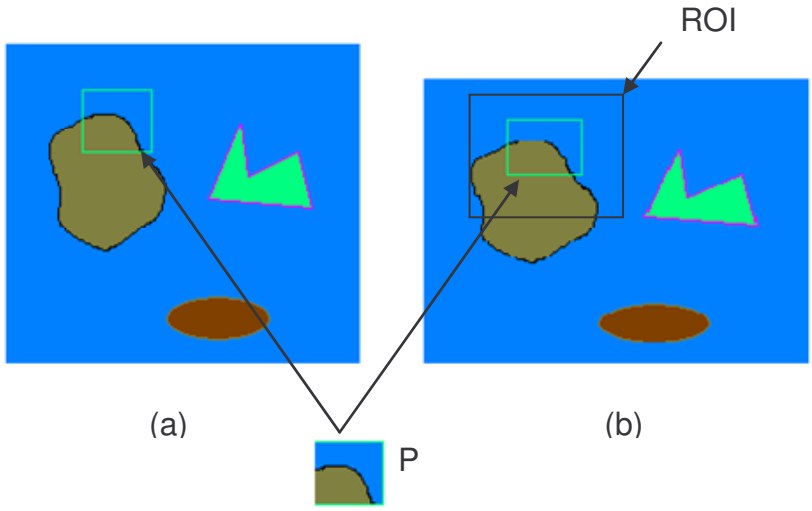

Figure 1-1: Block matching principle, P is the pattern selected in the first image (a). It can be found in the second compressed image (b) in the region of interest (ROI) around the initial position of the kernel

The basic idea of block matching has been applied with different approaches, trying to optimize the estimation result according to the different key parameters of the method. The first important parameter is the block's size.

Block's size

The ability to find the right position of a selected pattern in a certain region of interest is highly affected by its size with two different tendencies. A large block will increase the uniqueness of each block by including more information. But at the same time, the gain in accuracy will result in a lower spatial resolution [2].

Block matching techniques assume that the whole pattern inside the block has the same motion vector. This assumption is easily violated when using a large block if non-rigid movement or rotation is present.

In order to include advantages of both, small and large patterns, Yeung *et.al.*, in [26], have used a multilevel speckle tracking approach. In their work both the matching block and search window, are of variable size, based on a coarse to fine scheme. A large block size is first used to give a coarse estimate of the displacement of the point P_o, this first step is noticed L=1 in Figure 1-2 and the first displacement is noticed Δ_1. This step ensures that the region selected is the right one. Then smaller blocks and smaller search windows are used in order to increase the spatial resolution without loosing the information given by the prior level. This is done for L=2 and L=3 in our example. Finally the new position of the point is found and noticed P_f. The total displacement is equal to the sum of all displacements found at the previous steps.

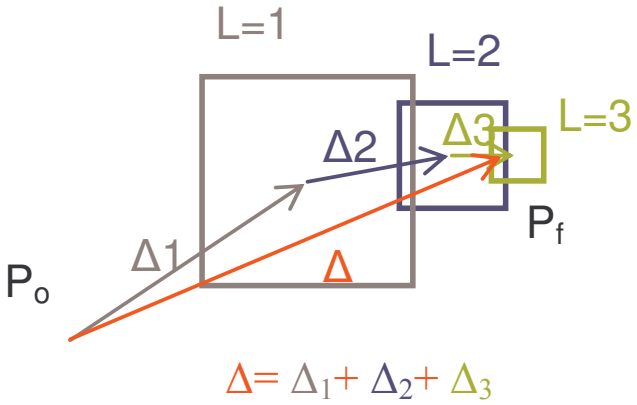

Figure 1-2: Coarse to fine approach used in [26]. P_o is the initial position and P_f the final one, the initial step is L=1, and the last one L=3, the total displacement is the sum of all small displacements

Matching criterion

In order to find the displacement, the initial block and those selected from the ROI are compared. This comparison is done by calculating a matching criterion that can indicate how much the blocks are identical or how much they are different. In the first case the criterion is maximized whereas in the second case it is minimized.

Langeland *et.al.,* in [3], have made a comparison in 2003 between the most used criterions. They first present the correlation. At a certain position (x_0, y_0) the estimated displacement vector is denoted $\hat{\Delta} = [\hat{\Delta}x, \hat{\Delta}y]$. The discrete expression of the correlation $R_{xc}(x_0, y_0, \hat{\Delta})$ is given in (1-13)

$$R_{xc}(x_0, y_0, \hat{\Delta}) = \sum_{n=-N}^{N} \sum_{m=-M}^{M} r(x_0 + n, y_0 + m) s(x_0 + n + \hat{\Delta}x, y_0 + m + \hat{\Delta}y) \quad (1\text{-}13)$$

where $2N+1$ and $2M+1$ are the size of the correlation blocks in the lateral and axial directions, respectively.

Then they present the normalized correlation $R_{Nxc}(x_0, y_0, \hat{\Delta})$

$$R_{Nxc}(x_0, y_0, \hat{\Delta}) = \frac{\sum_{n=-N}^{N} \sum_{m=-M}^{M} r(x_0 + n, y_0 + m) s(x_0 + n + \hat{\Delta}x, y_0 + m + \hat{\Delta}y)}{\sqrt{\sum_{n=-N}^{N} \sum_{m=-M}^{M} r^2(x_0 + n, y_0 + m) \sum_{n=-N}^{N} \sum_{m=-M}^{M} s^2(x_0 + n + \hat{\Delta}x, y_0 + m + \hat{\Delta}y)}} \quad (1\text{-}14$$

In those two cases the criterion is maximized over the ROI. The normalization reduces the risk of estimation errors due to a global change in brightness between the two acquisitions.

Two other criterions are also presented. The sum of absolute differences $R_{SAD}(x_0, y_0, \hat{\Delta})$ is expressed in (1-15)

$$R_{SAD}(x_0, y_0, \hat{\Delta}) = \sum_{n=-N}^{N} \sum_{m=-M}^{M} \left| r(x_0 + n, y_0 + m) - s(x_0 + n + \hat{\Delta}x, y_0 + m + \hat{\Delta}y) \right| \quad (1\text{-}15)$$

and the sum of squared differences $R_{SSD}(x_0, y_0, \hat{\Delta})$

$$R_{SSD}(x_0, y_0, \hat{\Delta}) = \sum_{n=-N}^{N} \sum_{m=-M}^{M} \left(r(x_0 + n, y_0 + m) - s(x_0 + n + \hat{\Delta}x, y_0 + m + \hat{\Delta}y) \right)^2 \quad (1\text{-}16)$$

(1-15) and (1-16) are minimized over the ROI.

Langeland *et.al*. have tested the estimators in different situations including different axial and lateral displacement values and different window sizes. Their conclusion is that normalized correlation performs better than correlation, whereas the differences between SAD, SSD and normalized correlation are in general not very large. However for small windows sizes the SSD outperforms the other estimators.

They also noticed the influence of the window size recalling us that a smaller window size is preferable for better resolution, but a larger one has a better accuracy.

Type of data processed: envelope or RF

Another important parameter affecting the performance of correlation based algorithms is the nature of the data used, the radio frequency signal (RF) or its envelope. RF data contains phase information which is lost when calculating the envelope. As a consequence keeping this information increases the uniqueness of the speckle pattern inside a given block. Ramamurthy and Trahey [4] and Bohs and Trahey [2] have shown that estimation using RF data is more accurate than using envelope data,

particularly for the axial direction. This is because the auto-correlation length of speckle in the axial direction is shorter for RF than for envelope.

However it is important to notice that no oscillations are naturally present in the lateral direction of the image. This means that using RF data for block matching will yield results with high non-uniformities in the two directions of estimation. This has led Bohs and Trahey [2] to the conclusion that despite the resulting coarser resolution, the use of B-scan[2] data might be more advantageous because it leads to more uniform results.

Drawbacks of the method: decorrelation, computing complexity, sub-pixel displacement estimation and some solutions.

One of the most significant drawbacks inherent in speckle tracking is the loss of motion information due to speckle de-correlation. Ultrasonic speckle patterns arise from the constructive and destructive interferences of coherent echo signals [27]. Speckle de-correlation can be introduced by out of plane motion, non uniform motion of sub resolution scatterers, non-uniformity of the ultrasound field and non rigid tissue deformation. Since speckle tracking algorithms depend on the stability of the speckle pattern they often yield inaccurate motion estimates where speckle de-correlation is high.

Instead of considering only rigid transformation of the blocks it is possible to include deformation, rotation or shearing in the optimization process of the criterions described previously. Stiller gives different motion models that can be used in [28]. The application of such an example for motion estimation in ultrasound is given by Maurice in [29]. But this increases the computation requirements which are already high.

Indeed cross-correlation between blocks needs a lot of calculation. Of course computer possibilities are always higher but from an economical point of view it is still an advantage to develop methods with lower calculation consummation.

For blood flow, an important drawback of block matching techniques is the necessity to have 2D images where the A-lines are acquired at difference time instances. Indeed between the acquisitions of two RF lines the blood has been moving. This leads to different estimation possibilities that depend for example on the direction of the flow. In order to limit this effect it is possible to acquire parallel beams. Based on the principle of explososcan presented by Shattuck *et.al.* in [30], Bohs *et.al.* have implemented a speckle tracking method using two parallel beams [31].

Sub-pixel displacement estimation is not possible naturally in block matching techniques. This is really an important drawback for tissue elasticity imaging where a small deformation is mostly applied in the axial direction, which leads to an even smaller deformation in the lateral direction in which the pixel size in much larger than in the axial direction. As a consequence, the original data of the correlation function have to be interpolated in order to reach sub-pixel estimates. Konofagou [32] for example calculated 64 linearly interpolated RF lines between the beamformed RF lines. Geiman *et.al.* [33] used a non linear interpolation method they called *grid slopes* to perform sub-pixel motion estimation using a SAD (as defined in (1-15)) block matching algorithm.

In 2000, Giachetti, in [34], has given a review about matching techniques for computing image motion. It is not only about ultrasound imaging but he gives some ways to improve the method by sub-

[2] B-Scan are defined later in equation (2-8)

sampling the block for example, using look-up tables or use coarse to fine approaches. Chen in his article of 2001 [35] gives also a short overview of methods to accelerate block matching methods.

Recent application of speckle tracking

The matching techniques presented above have been investigated a lot since the late 80's and in the field of tissue elasticity imaging. Recent works have shown the possibility of their use in vivo.

In 2002, Zhu and Hall presented a modified block matching method for real-time and freehand strain imaging [6]. They give experimental results on tissue mimicking phantoms with small spherical targets and in vivo images of breast and thyroid.

In 2003, Golemati *et.al*. presented in vivo results for vascular imaging [5].

In 2D block matching techniques, the patterns are translated over a two dimensional area, in order to find the new position. Another approach is to work on crossed beams. In this case the estimation is always in only one direction. The results are then projected on the conventional axial and lateral directions. These methods are presented in the following section.

1.3.2. Crossed beam techniques

The principle in crossed beam techniques is to use different angles of steering when focusing around a certain point of interest. The information collected from the different directions is then combined in order to estimate the 2D or 3D displacement vector or velocity vector. A first approach of crossed beam for Doppler velocimetry was published by Fox in 1978 [36].

Whereas in block matching methods, the selected blocks are searched inside two dimensional regions of interest and the position of the maximum resemblance gives the displacement, crossed beam techniques use directional 1D correlation. In this case only correlation along signals is considered. The original pattern is 1D as well as the ROI. The same kind of criterion as for 2D block matching techniques can then be used in order to find the good position along the specific direction. The result is then projected on the conventional axial and lateral axis. Several beams are used and the result is then averaged.

The principle of this approach is presented in Figure 1-3. A point of interest P is considered. At this particular position the displacement is equal to $\boldsymbol{\Delta} = [\Delta_x, \Delta_y]$, where $[\Delta_x, \Delta_y]$ are the projections of $\boldsymbol{\Delta}$ along the lateral and axial spatial directions respectively.

A beam can be steered from the aperture towards the point of interest in order to beamform a signal along the direction α_1. The displacement is then estimated along this direction, it is denoted $\Delta_{\alpha 1}$. The same kind of estimation as those presented in 1.3.1 can be used with a 1D speckle pattern searched in a 1D region of interest. This has to be done at least one more time. In Figure 1-3 it is done along direction α_2 leading to a displacement along this direction denoted $\Delta_{\alpha 2}$.

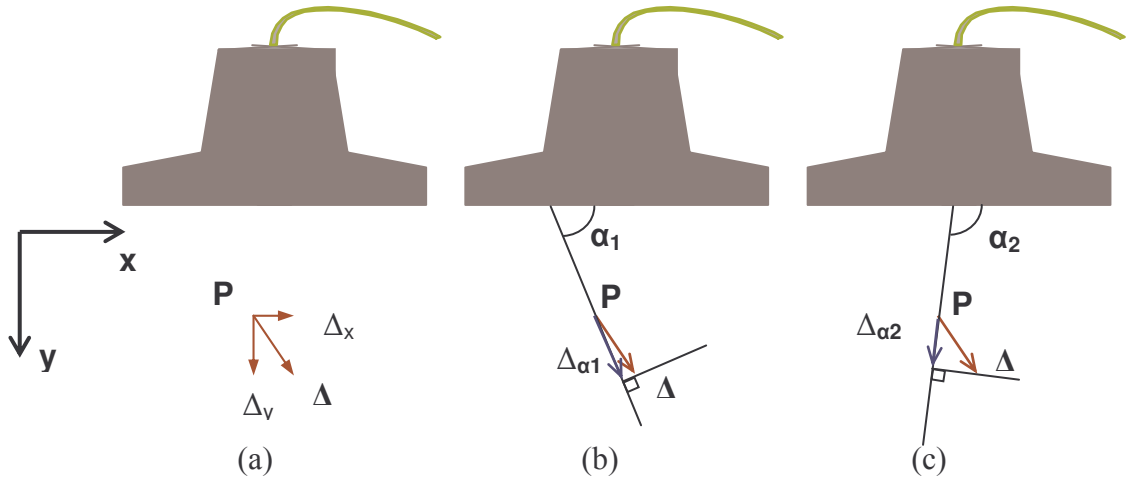

Figure 1-3: Principle for multiple crossed beam techniques, the displacement around the point of interest P is estimated along different directions, and then projected on the axial and lateral directions. (a) Gives the global configuration, (b) shows the estimation along direction $\alpha 1$ and (c) along direction $\alpha 2$.

Using $\Delta_{\alpha 1}$ and $\Delta_{\alpha 2}$ it is possible to recover Δ_x and Δ_y by simply calculating

$$\Delta_x = \Delta_{\alpha 1}\cos(\alpha_1) + \Delta_{\alpha 2}\cos(\alpha_2) \quad (1\text{-}17)$$

$$\Delta_y = \Delta_{\alpha 1}\sin(\alpha_1) + \Delta_{\alpha 2}\sin(\alpha_2) \quad (1\text{-}18)$$

This is the basic idea. But in order to obtain more robust estimates this operation can be done for a larger number of beams with an averaging of the values of the couple $[\Delta_x, \Delta_y]$.This is for example what is done by Tanter *et.al.* in [7]. The use of this kind of methods necessitates the possibility to acquire all raw data on the probe and to beamform in post-processing. Very few teams in the world have access to this kind of equipment.

Nitta and Shina [37] [21] also developed a method that can be classified as multiple crossed beams. Indeed they use a 2D array probe and they retrieve the full three dimensional displacement vector using their *weighted phase gradient method*. Their method is based on the fact that the phase shift detected at all individual elements of the 2D probe can be expressed as the equation of a plane with respect to the two spatial coordinates that include the 2D probe. They have developed the experimental setup and have tested it for blood flow and tissue elasticity imaging.

Another recent approach where we can speak about multiple beams was presented by Jensen. His method was developed for blood flow but it could be applied for other purposes. In 2003 [8] [9] he gives the method assuming that the direction of flow is known. A signal is beamformed along this direction and cross-correlation along this direction enables to give the value of the flow. The estimate is then projected on the axial and lateral axes using

$$\Delta_x = \Delta_\alpha \cos(\alpha) \quad (1\text{-}19)$$

$$\Delta_y = \Delta_\alpha \sin(\alpha) \quad (1\text{-}20)$$

He also gives a method for determining the direction of flow in [38]. In order to do this, different signals are beamformed in different directions around a specific point of interest. All maximum cross-

correlation coefficients are calculated for all directions of interest. The direction of flow α is the one with the highest maximum correlation coefficient.

Both block matching techniques and crossed beams techniques are more or less based on correlation calculation.

Another method that has been applied for displacement estimation in ultrasound imaging is the use of optical flow. Optical flow is presented in the following section.

1.3.3. Optical flow

An other way of determining the displacement that occurs between two images acquired at two time instances is to calculate the optical flow. Determining displacement of a medium scanned with ultrasound using optical flow is also based on the assumption that the image of the displaced medium is a displaced version of the initial image.

In order to compute the optical flow, an equation that relates the changes in image brightness at a given point to the motion of the brightness pattern, has to be derived. The basic assumption that is used to derive this relation is that the brightness of a particular point in the pattern remains constant in time [10]. This is expressed by

$$\frac{dB}{dt} = 0 \tag{1-21}$$

where $B = B(x, y, t)$ is the image brightness at the point (x, y) in the image plane, at time t. This can be developed as

$$\frac{\partial B}{\partial x}\frac{dx}{dt} + \frac{\partial B}{\partial y}\frac{dy}{dt} + \frac{\partial B}{\partial t} = 0 \tag{1-22}$$

letting

$$u = \frac{dx}{dt} \tag{1-23}$$

$$v = \frac{dy}{dt} \tag{1-24}$$

be the two spatial velocities along the lateral and axial direction, respectively. This leads to a single equation with two unknowns.

Equations (1-21) and (1-22) mean that when a given pattern moves between the two images, one particular point of the patter conserves the same brightness. If the brightness level of a given pixel has changed between the two images, according to (1-22) $\frac{\partial B}{\partial t} \neq 0$, at least one of the terms $\frac{dx}{dt}$ or $\frac{dy}{dt}$ has to be non zero, which means that there is a displacement between the images.

Additional constraint has to be introduced. Horn and Shunk [10] introduced the *smoothness constraint* which assumes that the velocity changes slowly in the neighborhood of a given point of interest. This constraint, which has also been used by Mailloux *et.al.* in [39], is written by minimizing the gradient of the optical flow velocity expressed by

$$ec^2 = \left(\frac{\partial u}{\partial x}\right)^2 + \left(\frac{\partial u}{\partial y}\right)^2 + \left(\frac{\partial v}{\partial x}\right)^2 + \left(\frac{\partial v}{\partial y}\right)^2 \tag{1-25}$$

Finally the estimation of the optical flow is a minimization problem that combines the minimization of the optical flow error eb expressed by

$$eb = \frac{\partial B}{\partial x}\frac{dx}{dt} + \frac{\partial B}{\partial y}\frac{dy}{dt} + \frac{\partial B}{\partial t} \tag{1-26}$$

and the smoothness constraint given in (1-25) , with a certain weighting coefficient λ which is necessary because both quantities cannot be expected to be identically zero due to quantization error and noise [10]. The total quantity to be minimized is then

$$e^2 = \int\int (\lambda ec^2 + eb^2)dxdy \tag{1-27}$$

This is the basic idea in optical flow methods. Different minimization strategies can be used, and other studies have included additional constraints, with for example hypothesis of linearity of the optical flow [39]. For heart motion estimation, the linearity constraint enabled to separate translational from rotational, divergence and shear fields. This is interesting because a global translation could appear because of breathing for example, or moving of the ultrasound probe, which in not related to the heart's activity.

Optical flow also requires a considerable amount of computation time.

1.3.4. Spatial quadrature and synthetic lateral phase

More recently the idea of introducing oscillations, and to use phase information, in the lateral direction of the pressure field was proposed. Similar approaches have been proposed by Jensen and Munk [11] and Anderson [40] for transverse blood flow estimation. The idea is to produce a pressure field with oscillations not only in the axial direction but also in the perpendicular direction of the image plane. The presence of these oscillations introduces a modulation in the signal backscattered from a blood scatterer having a transverse movement across the pressure field.

Like in the pure axial case, where a quadrature signal is needed for velocity estimation, here the concept is extended for the lateral direction and it is possible to speak about spatial quadrature.

One of the main differences between the two approaches relies on the way the two 90° laterally phase shifted pressure fields are generated. Both approaches use two beamformers. Anderson achieves this task by using one beamformer based on an even apodization, the other one on an odd apodization function. Jensen and Munk use two different focus directions having a 90° phase shift in the lateral direction, at the point of interest.

Furthermore the estimation is not the same.

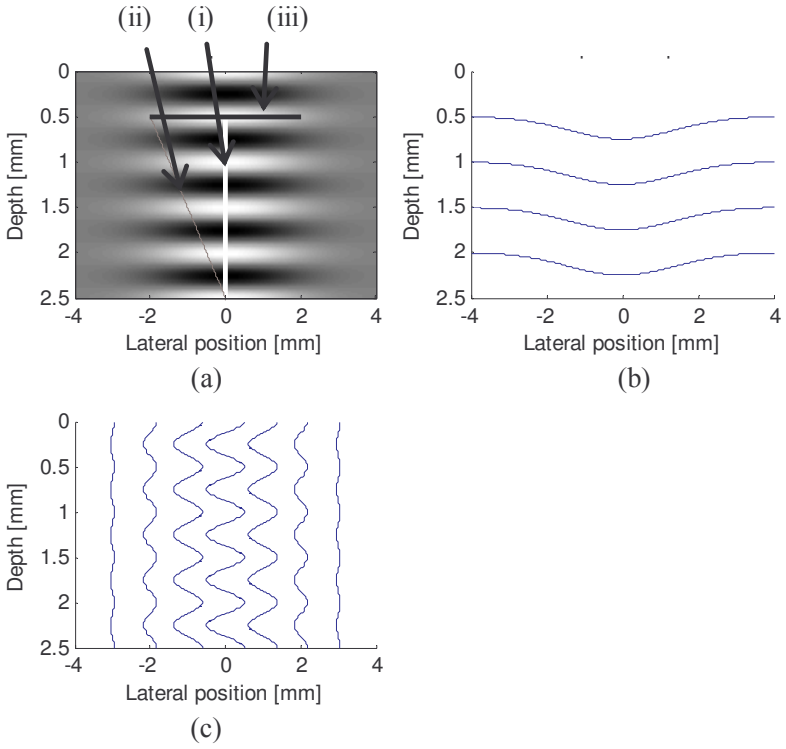

Figure 1-4: Classical pressure field (a), with lateral (b) and axial (c) profiles. The three lines in white, grey and black correspond to the path of the scatterers whose pressure received is represented in Figure 1-6

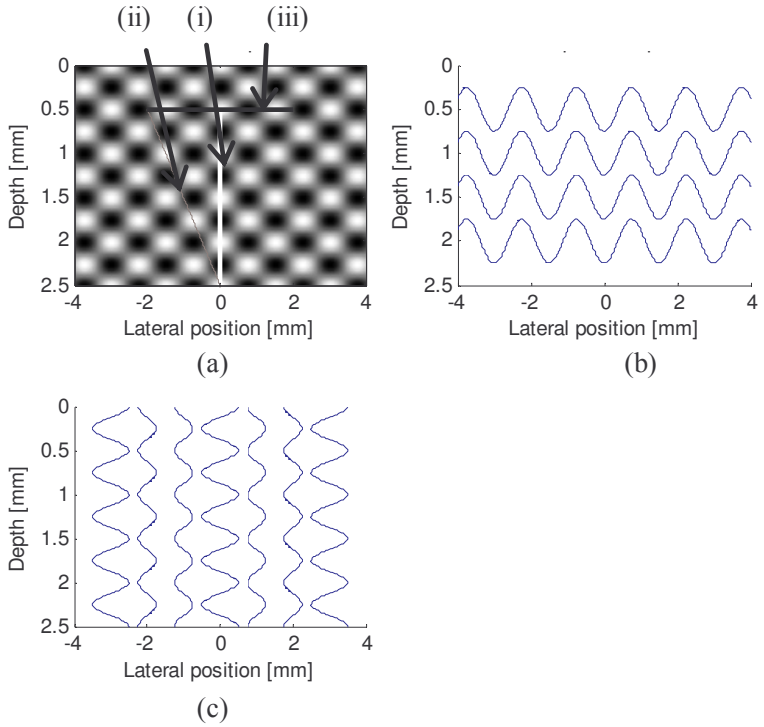

Figure 1-5: Lateral oscillations pressure field (a), with lateral (b) and axial (c) profiles. The three lines in white, grey and black correspond to the path of the scatterers whose pressure received is represented in Figure 1-7

Figure 1-4 and Figure 1-5 show a classical pressure field having only oscillations in the axial direction and a pressure field having oscillations in both directions, respectively.

Figure 1-4 and Figure 1-5 also give the axial and lateral profiles of those pressure fields.

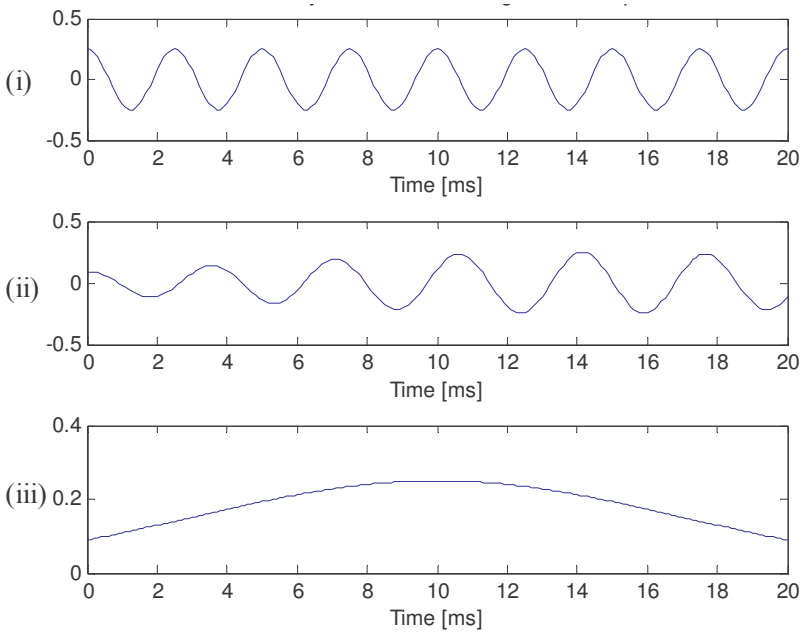

Figure 1-6: Pressure received by a scatterer crossing the normal pressure field, with an angle of 0°, 45°, and 90° (i), (ii), and (iii) respectively. The corresponding paths are represented in Figure 1-4 in white, grey and black, respectively.

Let's imagine that a scatterer is crossing both pressure fields with a given angle. An angle of 0 degree indicates a purely axial velocity of the scatterer. An angle of 90 degrees indicates a displacement perpendicular to the beam axis. Figure 1-6 shows the pressure that would be received by a scatterer crossing the pressure field of Figure 1-5 with angles of 0, 45 and 90 degrees. And Figure 1-7 the one received by a scatterer crossing the lateral oscillations pressure field of Figure 1-5 with the same angles.

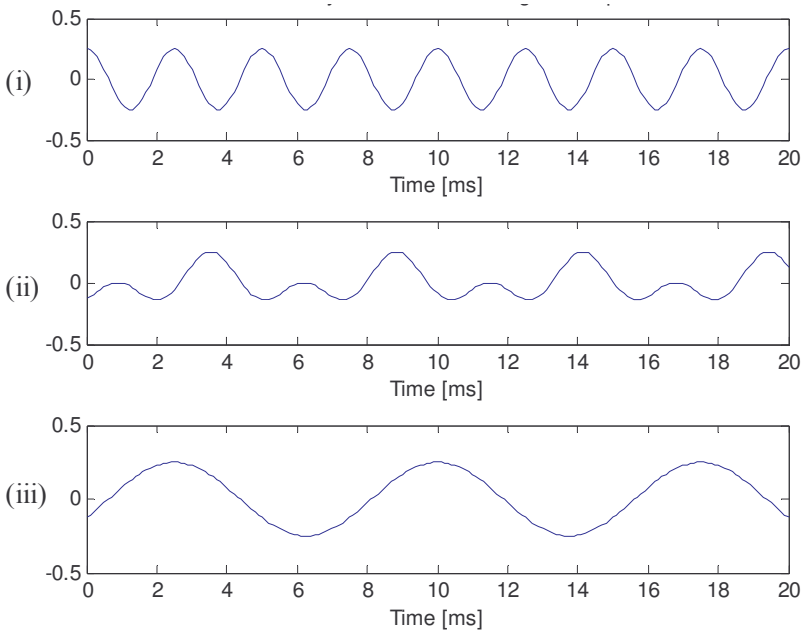

Figure 1-7: Pressure received by a scatterer crossing the lateral oscillations pressure field, with an angle of 0°, 45, and 90°, (i), (ii), and (iii) respectively. The corresponding paths are represented in Figure 1-5 in white, grey and black, respectively.

Figure 1-6 and Figure 1-7 show clearly the differences between the pressure received by a scatterer crossing a classical pressure field and the one receive by a scatterer crossing a double oscillating pressure field. The pressure received by a scatterer crossing the double oscillating pressure field carries clearly a signature of the lateral oscillations. For a purely axial velocity this cannot be seen. But for a purely lateral displacement it is extremely important. Indeed, when a scatterer crosses a normal pressure field with an angle of 90 degrees, there are no oscillations whereas with the lateral oscillation the frequency of the pressure seen by the scatterer is directly proportional to its velocity.

Anderson hasn't published a lot about this work since 1998. But Jensen's group continues to investigate this approach. A paper not only about lateral oscillations has been published by Jensen in 2000 [24] and one presenting a new estimator in 2001 [41]. Recently in vivo results have been given by Udesen and Jensen in [42] and [43].

The approach with lateral oscillations enables to introduce the concept of lateral phase.

In elastography an approach that can be classified in this section has been recently published by Chen *et.al.* [12]. This work is sited here because it also uses the concept of lateral phase. The difference between this work and the other two approaches is that no particular beamforming is introduced in [12]. A synthetic lateral phase is created.

The two articles of 1998 by Jensen and Munk and Anderson have been the starting point for this PhD work in 2002. The initial idea was to investigate the possibility of using some kind of phase information in the lateral direction of the ultrasound image and apply this to tissue elasticity imaging with ultrasound. The aim is to understand how the phase signal can be controlled and to to change it in order to increase the quality of the lateral displacement estimation.

Before detailing our displacement estimation method, it is important to understand how an ultrasound image is constructed. This will be presented in the second chapter of this thesis.

Chapter 2

Ultrasound imaging and beamforming

In this chapter the different aspects of ultrasound imaging that are important for a good understanding of the material of this thesis are presented. First, ultrasound imaging is described in a really general way, explaining the physical phenomenon that is involved. Then, a simple mathematical description of the image formation is given. The last part of this chapter is devoted to beamforming and formation of the point spread functions. The parameters of the beamformer that influence the shape of the PSF are given. The way they can be changed in order to control the shape of the PSF is also given. Finally the validation of our system approach to ultrasound image formation is presented.

2.1 Ultrasound imaging

In this section the physical principle of ultrasound imaging is described. Then, a linear relation that explains the ultrasound image formation is given and explained.

2.1.1. Principle of echography

Ultrasound has begun to be used in medical application in the early 50's. In 1952, British J.J. Wild and American J.M. Reid have presented some of the first images of a 2D section of breast obtained by mean of ultrasound [44].

Basically, ultrasound imaging consists first of the production of an acoustic wave. This wave is produced by electrically exciting a piezoelectric transducer. The emitted wave propagates through the investigated medium. Some echoes due to acoustical heterogeneities arise in the medium. These echoes propagate back towards the transducer which is able to produce an electrical signal proportional to them. As the echoes are attenuated while propagating in the medium, time gain compensation (TGC) is applied to the signal. The TGC is an amplification that increases with respect to time of arrival. The signal is then envelope detected and log amplified. Such a signal is called an A-line (A for amplitude). It can be plotted. The height of the signal indicates reflection strength whereas

the other axis indicates time. If the hypothesis is made, that the sound speed is constant inside the human body, the axis can also be interpreted as depth. This is currently done, and the sound speed is taken equal to 1540 m/s. As the ultrasound wave has to go from the transducer to the echogeneïty and back again, the relation between depth d and time of arrival t is given as a function of the velocity c by

$$d = \frac{ct}{2} \tag{2-1}$$

The principle of pulse emission, interaction with the medium and production of the signal is shown in Figure 2-1.

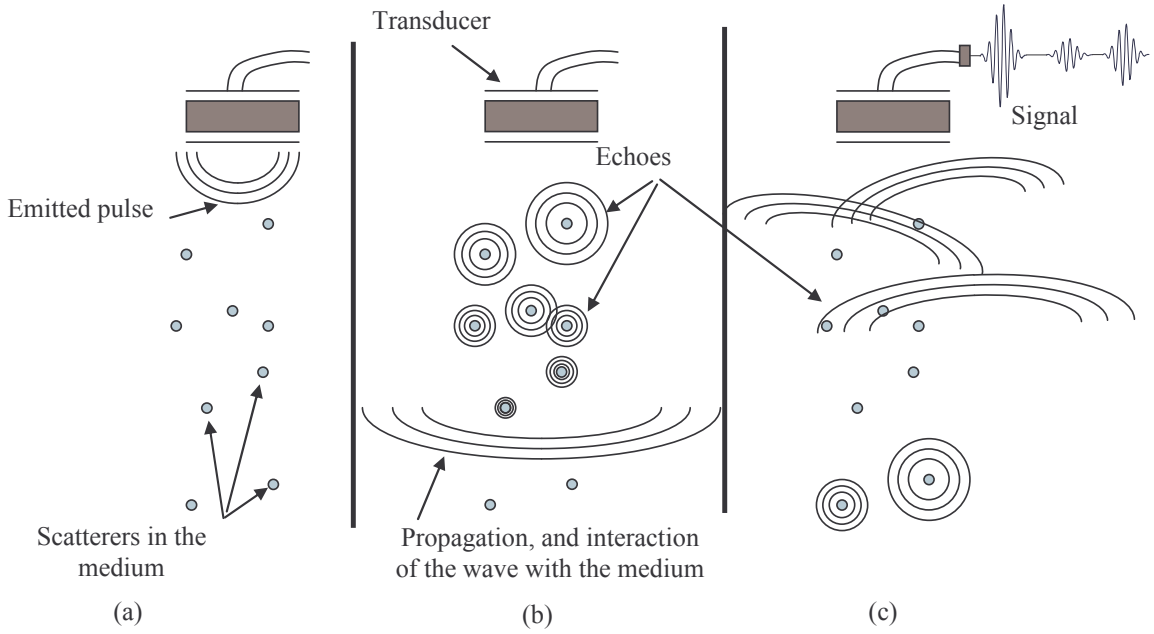

Figure 2-1: Basic principle of ultrasound imaging, (a) a pulse is emitted by the transducer, (b) the wave propagates through the medium, some echoes are backscattered from heterogeneities and (c) the echoes received at the transducer are traduced in an electrical signal. After some additional processing this signal becomes an A-line

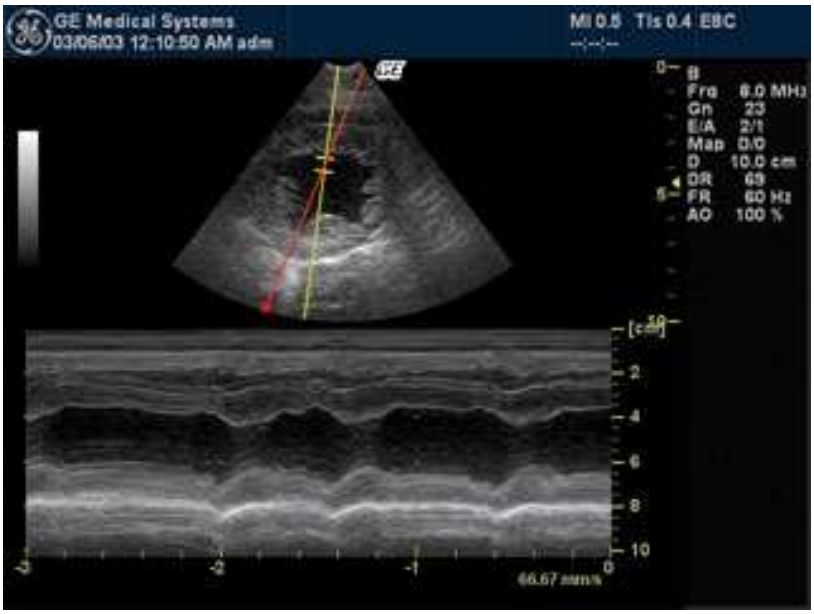

Figure 2-2: Image of the left ventricle on top and associated M-mode image at the bottom, from General-Electric web site (http://www.soundvet.com/Pages/US/Products.html). The depth of the anatomic structures changes with the time.

It is possible to highlight moving objects by acquiring successive A-lines with a transducer standing still on top of a moving tissue. The different A-lines are displayed as an image. Two successive A-lines are represented as two successive columns of the image. The height of the signal is coded in brightness levels, light gray and white corresponding to large echoes. This is called M-mode (M for moving). An M-mode image from a heart wall can be seen in Figure 2-2.

It is also possible to construct a conventional ultrasound image, of a still medium, by moving the transducer. The transducer is moved in order to sweep a certain region of interest. The A-lines are displayed as an image where brightness levels correspond to echo strength, as for M-mode. Such an image is called B-mode image (B for brightness). A B-mode image of a fetus can be seen in Figure 2-3.

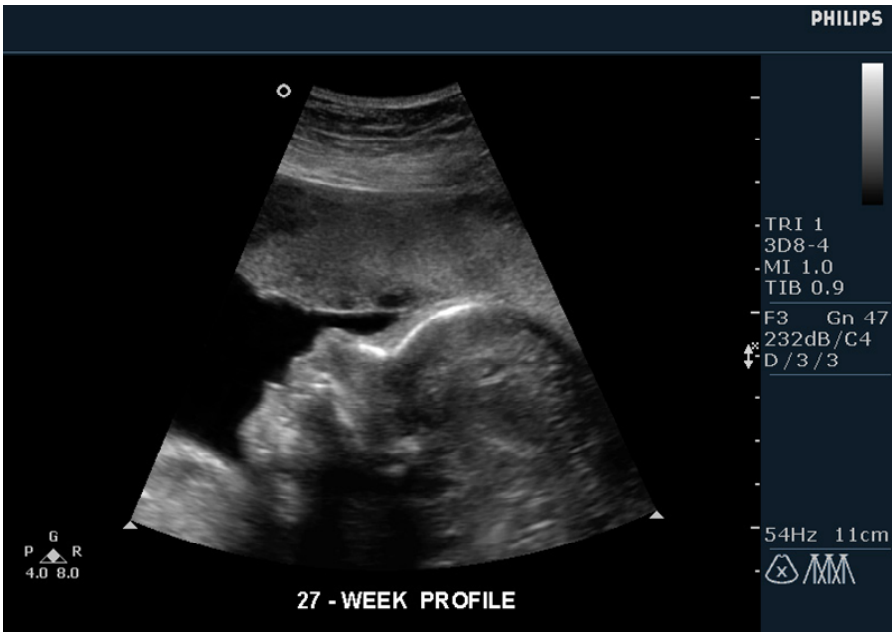

Figure 2-3: B-mode image of a 27 weeks old fetus from Philips web page. The head with the nose and mouth can clearly be seen on this image. From http://www.medical.philips.com/main/products/ultrasound/image_library/

The first ultrasound probes were based on mechanical translation or rotation of a single piezoelectric transducer. As the technology has been evolving, the tendency is now to have an increasing number of elements. Mechanical translation or rotation is replaced by electronic sweeping or steering. The probes can be separated into three main categories: linear arrays, convex arrays and phased arrays. Linear arrays provide rectangular images whereas convex arrays and phased arrays provide sector scans. Figure 2-3 is a sector scan. A linear array and a convex array probe are given in Figure 2-4. More information about the way these probes function is given in section 2.2.

(a) (b)

Figure 2-4: (a) convex array and (b) linear array ultrasound probes from B-K Medical (8807 and 8804 models, respectively)

Other applications have been developed based on ultrasound like intravascular ultrasound (IVUS) or 3D ultrasound. Those applications use other kind of probes but they all use the same basic principle given previously. Echography has also been used to make parametric imaging, and particularly blood flow. As the aim here is not to give a review of ultrasound imaging these aspects will not be developed, but an overview of blood flow techniques has been made by Jensen [45].

Now a simple mathematical model, that can be used to describe the image formation, will be presented.

2.1.2. System approach

The physical phenomenon involved in ultrasound imaging can be described by a simple linear relation if some assumptions are made. Both the imaging system and the medium have to be modeled. Here RF data are considered.

Model of the medium

As said in part 2.1.1, the physical phenomenon which is the basis of ultrasound imaging is the production of echoes in the medium investigated due to the propagation and interaction with the medium of the emitted acoustic wave. The echoes are due to acoustical impedance changes in the medium. Two models have been principally used to describe the medium: the heterogeneous continuum described for example by Sehgal and Greenleaf in [46] and the discrete model that has been widely used in the literature and has been initially proposed by Bamber and Dickinson [47].

As the heterogeneous model can be expressed in an equivalent way to the discrete model, the discrete model will be considered in our study.

It consists of a discrete 3D distribution of N scatterers, $d(x,y,z)$ spatially uncorrelated and expressed as

$$d(x,y,z) = \sum_{i=1}^{N} A_i \delta(x - x_i, y - y_i, z - z_i) \tag{2-2}$$

where $[x_i, y_i, z_i]$ is the position of the ith scatterer. The three coordinates of the scatterers are random uniform distributions [48]. The strength of A_i can be random Gaussian distributed.

Model of the ultrasound system

The second term that is involved in the formation of the ultrasound image corresponds to the imaging system. It can be described by its point spread function (PSF). The PSF is the image that would be generated by a medium composed of only one scatterer of unitary amplitude. The PSF is a three dimensional function denoted $h(x,y,z)$. It can be considered separable in the three spatial dimensions [47] as

$$h(x,y,z) = h_x(x)h_y(y)h_z(z) \tag{2-3}$$

The axial profile $h_y(y)$ is related to the excitation pulse and to the electro-mechanical impulse response of the elements [27]. The lateral profile $h_x(x)$, and the azimuthal profile, $h_z(z)$ are governed by diffraction and interference effect. $h_x(x)$ and $h_z(z)$ are also separable, one term corresponding to the emit process, and one to the receive process, [49] or [50].

$$h_x(x) = h_{xe}(x)h_{xr}(x) \tag{2-4}$$
$$h_z(z) = h_{ze}(z)h_{zr}(z) \tag{2-5}$$

$h_{xe}(x)$ and $h_{xr}(x)$ are the lateral profiles in emit and in receive, respectively. $h_{ze}(x)$ and $h_{zr}(x)$ are the azimuthal profiles in emit and in receive, respectively. The emit profiles correspond to the place where the energy is sent, whereas the profiles in receive correspond to a sensibility function showing where the energy is collected.

The image

In a limited region of the medium $[x,y,z] \in \Omega$ where the PSF is considered to be constant, the relation that describes the formation of the ultrasound image $r(x,y,z)$ is a convolution over the three spatial variables x, y and, z denoted $\underset{x,y,z}{\otimes}$, between the PSF $h(x,y,z)$ and the scatterer distribution $d(x,y,z)$ as follows

$$r(x,y,z) = h(x,y,z) \underset{x,y,z}{\otimes} d(x,y,z) \tag{2-6}$$

A conventional B-mode image is a 2D slice for a given azimuthal position z_0 given by

$$r(x,y) = r(x,y,z_0) \tag{2-7}$$

The B-mode image obtained from the RF image given in (2-7) is the envelope of the complex image expressed as

$$\left|\tilde{r}(x,y)\right| = \left|r(x,y) + H_y\{r(x,y)\}\right| \tag{2-8}$$

$H_y\{r(x,y)\}$ is the Hilbert transform of the image along the axial direction.

The PSF is rarely constant naturally for the whole volume containing the scanned medium. But we will see in the following part called beamforming how the different profiles of the PSF can be controlled.

One interesting point with this way of describing the image formation is that the influence of a displacement of the medium on the ultrasound image can easily be shown.

Formation of an image of a displaced medium

If a limited region of the medium $[x,y,z] \in \Omega$ is considered where the PSF is constant and the medium has been moved uniformly by a given displacement vector $\Delta = [\Delta x, \Delta y, \Delta z]$. The new distribution of scatterers $d'(x,y,z)$ is simply given by

$$d'(x,y,z) = d(x - \Delta x, y - \Delta y, z - \Delta z) \tag{2-9}$$

The new image, also called strain image, $s(x,y,z)$ is the convolution between this distribution and the PSF as

$$s(x,y,z) = h(x,y,z) \underset{x,y,z}{\otimes} d'(x,y,z) \tag{2-10}$$

It can be expressed as a function of the initial distribution $d(x,y,z)$ as

$$s(x,y,z) = h(x,y,z) \underset{x,y,z}{\otimes} d(x - \Delta x, y - \Delta y, z - \Delta z) \tag{2-11}$$

Finally it can be given as a function of the initial image $r(x,y,z)$, as

$$s(x,y,z) = r(x - \Delta x, y - \Delta y, z - \Delta z) \tag{2-12}$$

Relation (2-12) shows simply that the image of a displaced medium is a displaced version of the initial image.

This expression is of course very simple and it doesn't reveal the entire phenomenon that appears in the whole medium, like strain for example. But this hypothesis can be made locally, and this is what will be done in this work.

But first the way the imaging system point spread function can be controlled by beamforming is presented.

Remark: the description of the imaging system by a separable PSF has been used in the literature and is interesting for simple modeling purposes. However it does not describe the formation of an ultrasound image as good as an acoustic model as the one used in Field II for example [51], [16], [52].

2.2 Beamforming

The first ultrasound probes were equipped with only one piezoelectric transducer that was translated or rotated in order to sweep a region of interest. The first part of this section is going to explain how ultrasound imaging can be done with multi-elements probes and electronic sweeping.

2.2.1. Imaging with arrays

As said in section 2.1 there are mainly three kinds of ultrasound probes: the linear arrays, the convex arrays and the phased arrays. All three are going to be presented now.

Linear arrays

When imaging with a linear array, each A-line is constructed with a different sub-aperture composed of a certain number of elements. The sub-aperture is translated over a region of interest. This enables to construct a rectangular image. In order to cover a large region of interest, it is necessary to employ large arrays. Convex arrays can limit this problem.

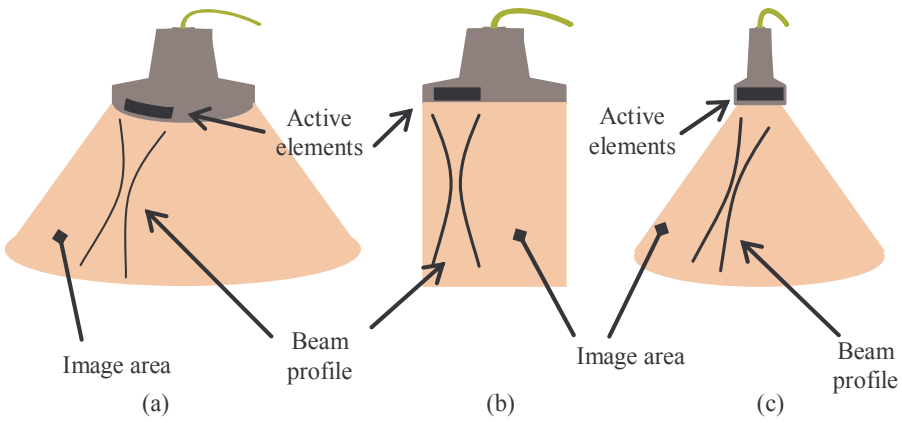

Figure 2-5: Principle of electronic sweeping with a convex array (a), a linear array (b), and a phased array (c)

Convex arrays

A larger area can be scanned with a smaller array if the elements are placed on a convex surface. A sector scan is then obtained. This is useful for imaging the abdomen for example. The principle of translating the active sub-aperture all over the probe is the same as for the linear array. But in some cases this can still be insufficient. For imaging the heart for example, smaller arrays are used in order to steer between the ribs; those arrays are the phased arrays.

Phased arrays

Phased arrays enable to have a large field of view using a small array. All elements of the array are used in transmit and receive. The direction of the beam is controlled by electronically delaying the signals emitted and/or received by the elements. The image can be acquired through a small window and the beam rapidly swept over the region of interest. The rapid steering of the beam compared to mechanical transducers is especially important in flow imaging.

Recently more advanced transducers have been developed. The number of elements is always increasing, and two dimensional arrays begin to be less uncommon.

In all different kinds of arrays, beamforming can be used in emit and receive in order to improve the contrast, depth of field or more generally to control the characteristics of the ultrasound image.

2.2.2. Delay and sum beamformers

Principle

In order to construct one A-line, more than just one piezoelectric element are used both in transmit and in receive. Ultrasound imaging is still using the most basic beamformers which are known under the name delay and sum beamformers.

If the emission is considered (the same principle can be made in receive), the idea is to excite the different elements at different instants in time. All elements produce a wave which will propagate in the medium and the obtained field is the sum of all contributions coming from the different elements.

It is possible to apply a weighting function, also called aperture function or apodization function, to the elements. In this case the field is a weighted sum of the wave emitted by each element.

The pressure field $P(x, y, z, t)$ can be expressed as

$$P(x, y, z, t) = \sum_{i=1}^{N} w_i p_o(x - x_i, y - y_i, z - z_i, t - \Delta t_i) \tag{2-13}$$

where x, y, z, t are the three space variables and time, N is the total number of elements, w_i is the weight applied to the ith element, x_i, y_i, z_i is the position of its center, Δt_i is the time delay applied to the signal exciting the ith element and $p_o(x, y, z, t)$ is the pressure field produced by one element centered at the origin of the coordinate system, as a function of space and time. In Figure 2-6

$p_o(x, y, z, t)$ would be the pressure as a function of space and time due to the black element. As all elements are supposed to be identical, the pressure of any other element can be expressed as a function of this element's pressure.

A representation of this principle is given in Figure 2-7 and the spatial configuration with the different variables is given in Figure 2-6.

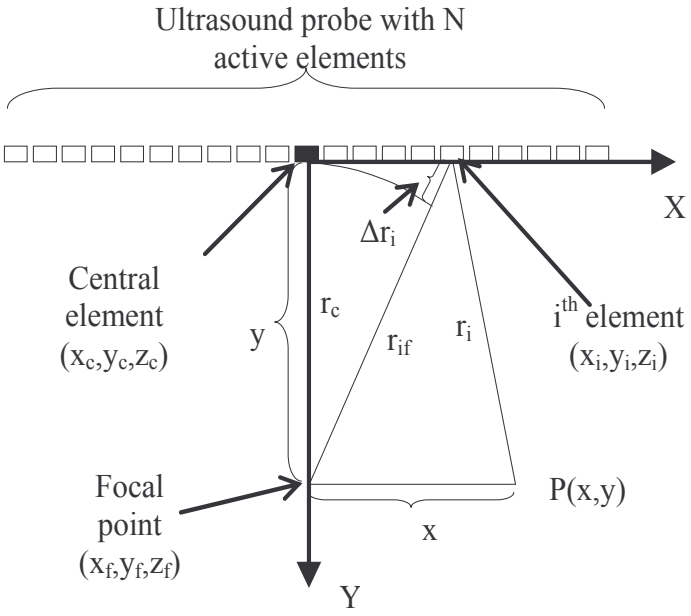

Figure 2-6: Spatial configuration in 2D. The focal point is at depth y. The central element is in black. The distance from this element to the point of interest is r_c. The distance from the ith element to the focal point is r_{if}. The delay applied to the signal of the emitted element is used to compensate the difference in path Δr. And the distance from the ith element to any point P of coordinates (x,y) is r_i. The pressure denoted $p_0(x,y,z,t)$ in (2-13) is the one due to the central element, the black one, as a function and space and time.

A delay and sum beamformer can also be used in receive. In this case, it is the signal received by all the elements which is delayed and apodized. All the signals are summed to form just one final signal.

Beamforming is much more flexible during receive. Indeed, in emit, once the elements have been excited nothing can be changed anymore. In receive it is possible to store all raw data and then to beamform with different weighting functions and delays according to the depth.

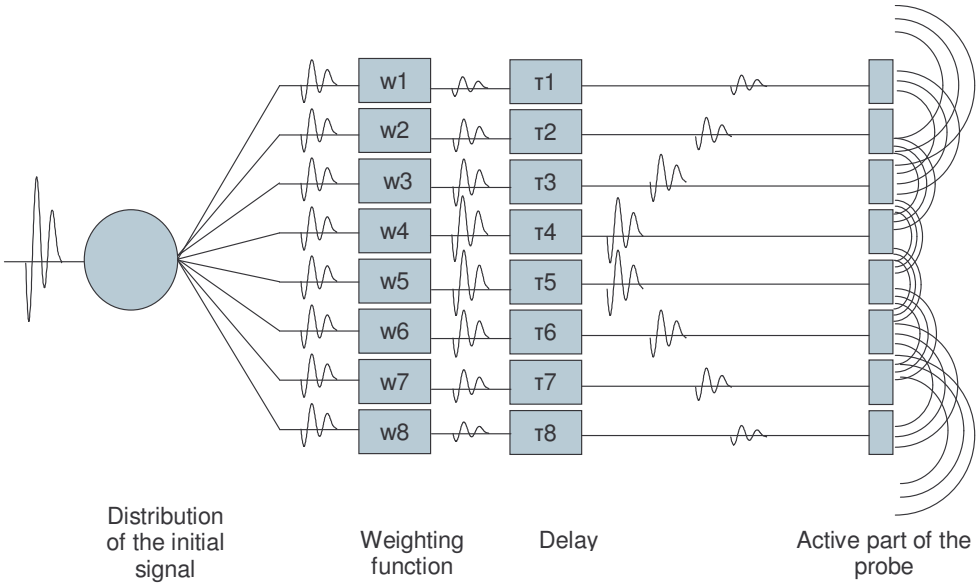

Figure 2-7: Principle of delay and sum beamformer for emit

Focusing

One important task that can be achieved by beamforming is focusing. In emit, focusing consists of applying the delays that enable all contributions coming from all elements to hit a given point called focal point at the same time. In receive, it consists of delaying all signals in order to sum contributions coming from the same given point of the medium called again the focal point.

The delays are easily calculated using ray acoustics [53].

The distance r_i, from the ith aperture element to the field point is

$$r_i = \sqrt{(x_i - x_f)^2 + (y_i - y_f)^2 + (z_i - z_f)^2} \tag{2-14}$$

where (x_i, y_i, z_i) is the center of the ith aperture element and (x_f, y_f, z_f) the position of the focal point.

The center of the aperture is situated at position (x_c, y_c, z_c). The distance from the center of the aperture to the field point is

$$r_c = \sqrt{(x_c - x_f)^2 + (y_c - y_f)^2 + (z_c - z_f)^2} \tag{2-15}$$

The delays that have to be used on each element of the array are used to compensate the difference in path and are equal to

$$\Delta t_i = \frac{1}{c}\Delta r_i = \frac{1}{c}(r_c - r_i) \tag{2-16}$$

With c the sounds speed. Using such delays enables to select any point as focal point.

2.2.3. Beamformer design for ultrasound imaging

The beamformer is a key part of the ultrasound image formation. It has already been seen in the previous section how focusing is achieved by changing the delays. In order to give some particular characteristics to the ultrasound images delay and apodization parameters have to be selected properly.

Some advanced methods have been presented in the literature in order to design beamformers. An interesting formulation of the beamformer design is given by Ranganathan and Walker in [49] and [54]. In their approach the problem is solved by minimization of the sum squared error (MSSE) between the obtained PSF and the desired PSF using a linear formulation. They give results for continuous wave and for the broadband case, and use their approach for different applications like depth of field improvement.

Even if their formulation is interesting, it is possible to have a simpler approach which gives also good results.

In this section the way the apodization function is chosen is described.

Approximation of the field and choice of the apodization function

As a first approximation, the aperture is considered as a linear aperture consisting of discrete point sources situated at depth $y_0 = 0$. These sources are considered to produce a spherical monochromatic continuous wave. We are interested in the field profile at the focus. A weighting function $w(x_i)$ is applied to the elements of the aperture. In this case the pressure at depth y and lateral position x is equal to

$$p(x,y) = \sum_{i=-\infty}^{+\infty} w(x_i) g(x_i, x, y) \tag{2-17}$$

where $g(x_i, x, y)$ is the Green function that corresponds to the propagation from the ith element at position x_i to the point of interest. Of course the number of elements of an ultrasound probe is not infinite, and only a finite number of N elements, corresponding to the number of active elements, have a non-zero weighting coefficient $w(x_i)$. By introducing in (2-17) the expression of the Green function in infinite space it is possible to write

$$p(x,y) = \sum_{i=1}^{N} w(x_i) \frac{e^{\frac{j2\pi r_i}{\lambda}}}{r_i} \tag{2-18}$$

λ is the wavelength of the emitted beam, N the number of active elements and $r_i = \sqrt{y^2 + (x_i - x)^2}$ is the length of the path from the ith aperture element to the point of interest.

It is possible to design the beamformer by using reciprocity theorem. This theorem indicates that the position of a point source and an observer can be reversed without altering the observed pressure [14], [13].

In this case the apodization function is taken equal to the pressure that would be provided at the location of the aperture elements by a probe located at the depth of interest and apodized with the expected pressure profile. This can be called back-propagation of the pressure field towards the aperture. Munk and Jensen have presented a method using back-propagation and pulsed plane wave decomposition [55]. The pulsed plane wave decomposition is less restrictive than our back-propagation because pulsed waves are considered whereas we still back-propagate continuous waves.

This can be expressed equivalently to (2-18), but with an integral as the pressure profile is continuous

$$w(x_i, y0) = \int_{-\infty}^{+\infty} p(x, y_0) \frac{e^{\frac{j2\pi r_{i0}}{\lambda}}}{r_{i0}} dx \qquad (2\text{-}19)$$

Equation (2-19) is given for a fixed depth equal to y_0. In this case the length of the path r_{i0} is equal to $r_{i0} = \sqrt{{y_0}^2 + (x_i - x)^2}$. Of course if the lateral pressure profile is constant as a function of depth, as it does not depend on y_0 it can be denoted $p(x)$, then the apodization function changes with the depth y. In the follwing, as we want a constant pressure profile as a function of depths, y_0 will not be written anymore. What has been called the pressure profile is identified to the lateral profile, in emit or in receive of the point spread function.

Finally designing a beamformer (if the azimuthal direction is not considered) consists in the following steps. First the lateral profile of the total point spread function $h_x(x)$ is chosen. Then, the emit and receive lateral profiles, $h_{xe}(x)$ and $h_{xr}(x)$, respectively, are chosen in order to satisfy (2-4). Finally the apodization functions in emit and receive, $w_e(x_i)$ and $w_r(x_i)$, are chosen by back-propagating the expected pressure profiles towards the aperture as given in (2-19).

Point spread functions

One interesting thing would be to have a constant point spread function in the whole medium. This can be interesting for ultrasound imaging in general, but even more for displacement estimation because it is one of the basic hypothesis. In order to reach this, a different beamformer has to be used for all depths of investigation. Indeed y is present in (2-19) and the apodization is a function of the depth.

Dynamic beamforming is unfortunately not possible in emit when using conventional ultrasound systems. This could be possible using synthetic aperture.

In synthetic aperture, all signals emitted by any element and received by any element of the probe are recorded. This can be done by exciting successively all element as presented by Ylitalo and Ermert in [56]. But, in this case, poor temporal resolution is achieved because exciting the elements one after another takes a certain time. More recently Gran and Jensen have investigated the possibility of exciting all elements at the same time and separating the information afterwards. In [57] they propose

a frequency division approach. The synthetic aperture approaches are also used in other domains like radar for example by Soumekh [58], [59].

If synthetic aperture is used, it is then possible to calculate, for each receive element, and any point in the medium, the right time delay that enables to be focused at that point. If this is done, it is possible to consider that both emit and receive are focused. But our work is not to investigate synthetic aperture, and another, simpler approach has been chosen.

If a broad beam is emitted, $h_{xe}(x)$ can be considered to have no influence on the final point spread function, because

$$h_{xe}(x) = 1 \tag{2-20}$$

This can be reached by emitting a plane wave, as explained by Jensen and Munk in [11].

In this case the point spread function is equal to the term in receive as

$$h_x(x) = h_{re}(x) \tag{2-21}$$

As a consequence beamforming is done only during receive. Dynamic quadratic focusing is applied for all depths of investigation and the apodization function is adapted with depth as explained earlier, according to (2-19).

A number of approximations have been used here. The emission is not considered whereas it probably has a small effect. The sources are not point sources but piezoelectric elements of a certain size and they don't emit a monochromatic wave.

In order to show the potential of our approach some field simulations have been done.

Validation of the beamformer by field simulations

The validation consists of a comparison between the lateral profile of the point spread functions obtained in a field simulation using our receive apodization functions and the expected profile. The simulation program Field II developed by Jensen *et.al* has been used [51], [16], [52].

Field II is a program for the simulation of ultrasound systems. It is based on the Tupholme-Stepanishen method [60] [61], and is fast because of the use of a far field approximation. Any kind of transducer geometry and excitation can be simulated, and both pulse-echo and continuous wave fields can be calculated for both transmit and pulse-echo. Dynamic apodization and focusing are handled through time lines, and different focusing schemes can be simulated. The versatility of the program is ensured by interfacing it to Matlab[3]. All routines are called directly from Matlab, and all Matlab features can be used. This makes it possible to simulate all types of ultrasound imaging systems.

It has been decided to simulate a classical Gaussian point spread function profile. The scatterer was situated at a depth of 20 mm. The expression of the expected profile is given by

[3] Matlab 7.0. Copyright © 1994-2004 The Mathworks, Inc.

$$h_x(x) = e^{-\pi\left(\frac{x}{\sigma_x}\right)^2} \tag{2-22}$$

σ_x is the standard deviation of our Gaussian pulse, it is nearly equal to the width at half maximum of the Gaussian. The simulation has been done with the parameters of the elements of the B-K Medical 8804 linear array probe.

All raw data have been saved and they were beamformed in post processing. Dynamic quadratic focusing has been used in receive. The parameters of the emission are given in Table 1.

Parameter	Value
Center Frequency	7 MHz
Total number of elements	640
Number of active elements in emit	512
Elements height	4.5 mm
Elements width	0.173 mm
Distance between 2 elements	0.035 mm
Focus in emit	Plane wave
Apodization in emit	Hann

Table 1: Simulation parameters: physical parameters of the BK Medical 8804 linear array probe, and parameters used in emit.

Figure 2-8 shows the dynamic apodization function that has been used in the simulation in order to get a point spread function having the same expression as (2-22) with $\sigma_x = 0.75\,\text{mm}$. It can be seen that around 70 elements have a significant weight. In this case, less elements are used in receive than in emit. As can be seen on the different profiles, the width of the apodization function has to increases with the depth in order to maintain the profile of the PSF constant through the entire medium.

The 2D point spread functions, and its lateral profile, are given in Figure 2-9 and Figure 2-10 respectively. And the expected profile is also plotted.

The profile of the point spread function obtained with Field II and the theoretical one are a bit different. The difference comes probably from the fact that the emit is not taken into account when designing the beamformer.

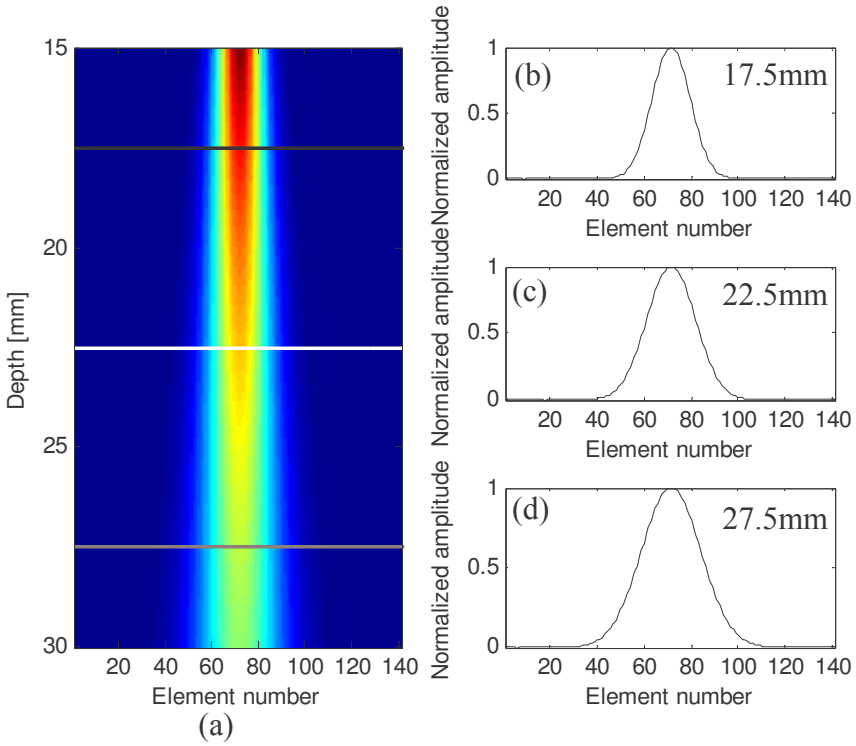

Figure 2-8: Dynamic apodization function used in order to obtain a Gaussian lateral profile of the PSF having a standard deviation of 0.75 mm with respect to depth, between 15 and 30 mm (a), and profiles corresponding to the black, white and grey lines, (b), (c) and (d), respectively.

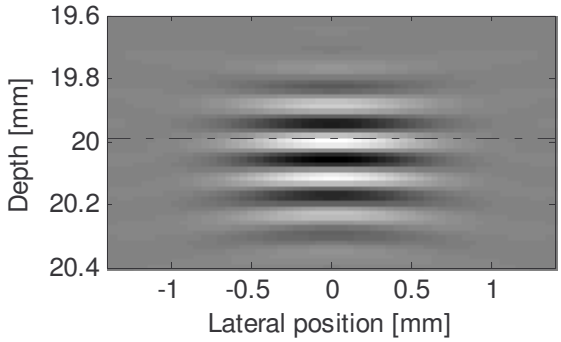

Figure 2-9: 2D PSF of a scatterer situated at a depth of 20 mm obtained with the apodization of Figure 2-8. The interrupted line gives the depth of the profile of Figure 2-10.

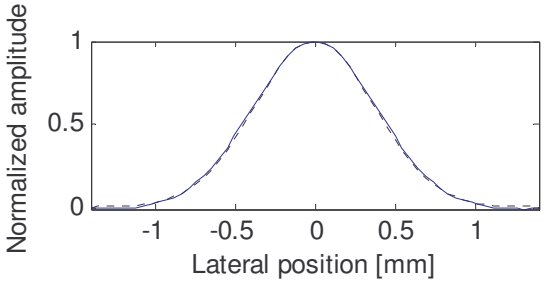

Figure 2-10: Lateral profile of the PSF of a scatterer situated at a depth of 20 mm in solid line, compared to the expected lateral profile in doted line

The normalized correlation between the expected lateral profile and the obtained lateral profile is equal to 99.8%.

The method presented to design our beamformer has shown results in good agreement with the simulated PSF. It can be qualified as really accurate according to the correlation coefficient between the expected and obtained PSF. It will be used in the rest of this thesis for calculating all apodization functions.

In the next section a different approach is also presented. This approach helps to understand and predict the shape of the apodization function that leads to a given pressure profile.

2.3 Fourier relation

An interesting approach to beamformer design is to use Fourier relation given by Fraunhoffer approximation. In Annex A it is shown how it is possible to approximate the pressure profile around the focal point by the Fourier transform of the apodization function as

$$p(x,y) = \frac{1}{C}\sum_{i=1}^{N} w(x_i) e^{-2j\pi \frac{x_i x}{y\lambda}} \tag{2-23}$$

where $p(x,y)$ is the complex pressure at depth y and lateral position x, N is the total number of active elements, $w(x_i)$ is the apodization function with respect to the lateral position x_i. Outside the sum, the terms have been regrouped under the variable $\frac{1}{C}$. As explained in Annex A, those terms are some phase terms whose influence can be neglected is some cases, especially when the distance away from the beam axis is small. Indeed, in (2-23), if the term $\frac{x}{y\lambda}$ is considered as a frequency variable, the sum corresponds to the Fourier transform of the discrete function $w(x_i)$. There is a scaling of the frequency variable by $y\lambda$ which means that this relation is a function of both the wavelength of the emitted beam, and the depth. As a consequence, in order to maintain the pressure profile constant with the depth, the apodization function has to be changed dynamically.

This approach is a bit less precise than back-propagation given in (2-19) because of the approximations used to write (2-23), but it helps to give a good feeling of what kind of apodization functions lead to some particular field shapes. Indeed in order to get a given pressure profile it is simply necessary to take as apodization function, the inverse Fourier transform of the desired profile as

$$w(x_i, y) = F^{-1}\left\{ p\left(\frac{x}{\lambda y}\right) \right\} \tag{2-24}$$

In order to illustrate this relation, the same example as in the previous section is taken and the apodization functions obtained with both approaches are compared.

The expression of the lateral profile of the PSF is given in (2-22). Here the standard deviation is equal to $\sigma_x = 0.75\,\text{mm}$. As it is a Gaussian function, according to Fourier relation the apodization function should also be Gaussian shaped. One apodization function is calculated with the Fourier relation, and the other one with the back-propagation and the results are shown in the following figures.

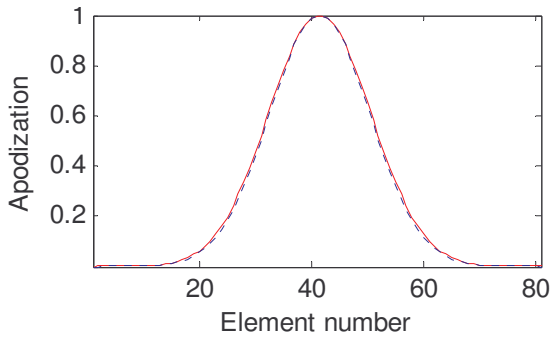

Figure 2-11: Apodization functions given by back-propagation (2-19) in doted line and by inverse Fourier transform (2-24) in solid line. The difference can hardly be seen between the two profiles.

Figure 2-11 shows that the apodization is a Gaussian, as expected. The difference between both apodization functions is extremely small. It is hardly possible to distinguish a difference between the two profiles.

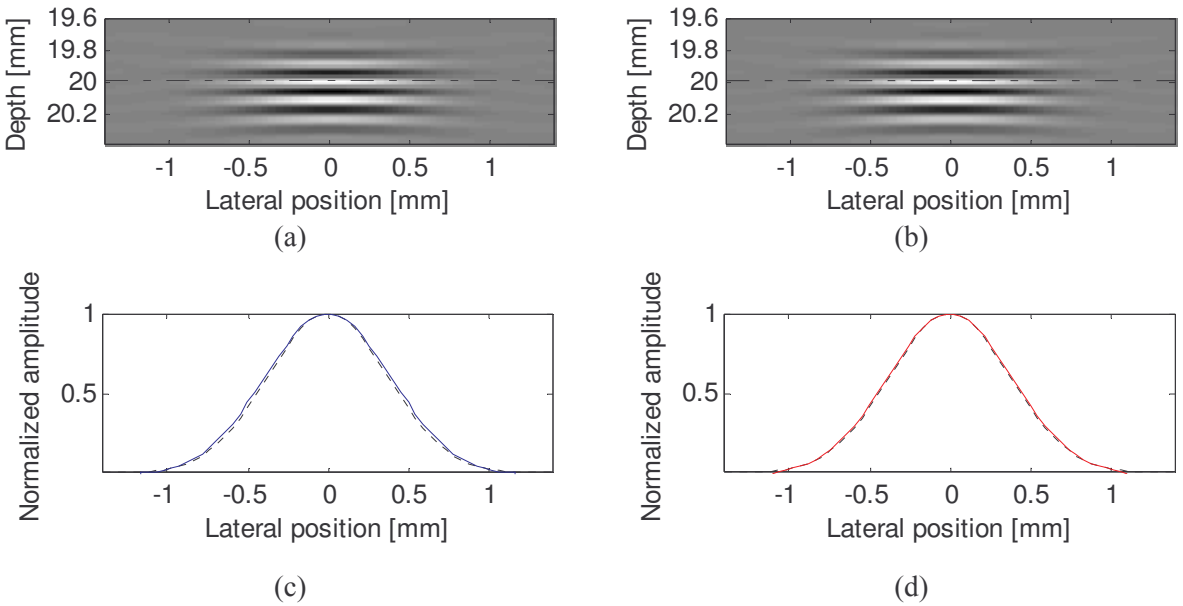

Figure 2-12: 2D PSFs obtained with the two apodization functions Figure 2-11, and the corresponding lateral profiles, (a) and (c) with Fourier relation and (b) and (d) with back-propagation. The interrupted lines give the depth of the profiles.

In Figure 2-12, which gives the 2D point spread functions and the corresponding lateral profiles, it is hard to evaluate visually the improvement due to our approach. The normalized correlation between the obtained profile and the expected one, in our case, is equal to 99.98% and for the Fourier relation it is equal to 99.94%, which is a small but existing improvement of 0.04%.

However in some situations a difference can be seen, especially when the approximations leading to the Fourier relation are less respected. This is for example the case if more active elements are used for the same scatterer. This is illustrated now.

Here the expected lateral profile has the same shape as the previous one except that the standard deviation of the Gaussian has been divided by three and is now equal to $\sigma_x = 0.25$ mm.

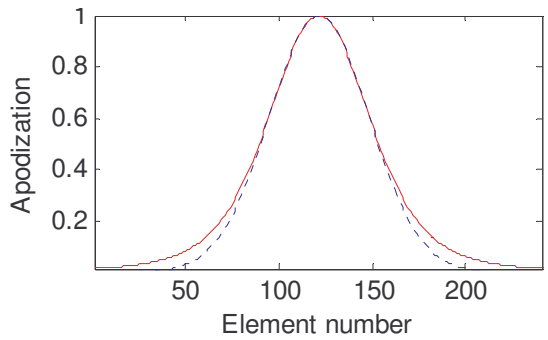

Figure 2-13: Apodization functions given by back-propagation (2-19) in doted line and by inverse Fourier transform (2-24) in solid line. Here a difference between the two profiles can be seen.

Figure 2-13 gives again the apodization functions given by the two approaches. It is now clearer that the result is not identical. The dotted line decreases faster than the solid line.

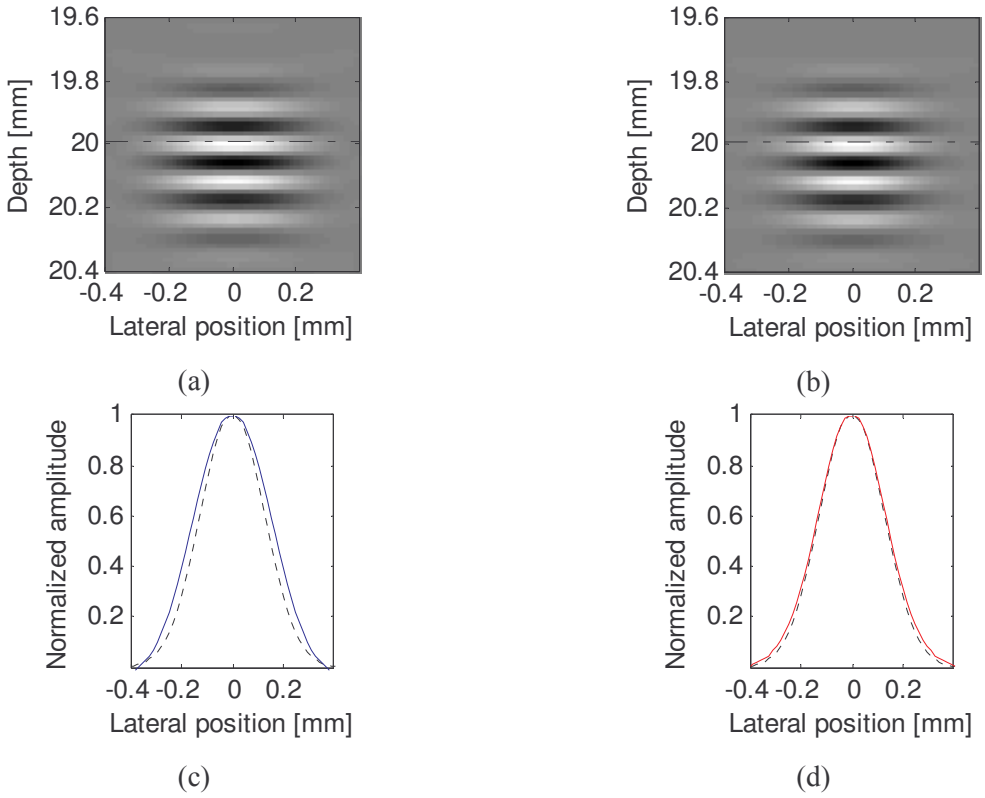

Figure 2-14: 2D PSFs obtained with the two apodization functions of Figure 2-13 and the corresponding lateral profiles, (a) and (c) with Fourier relation and (b) and (d) with back-propagation. The interrupted lines give the depth of the profiles.

Finally in Figure 2-14 it is possible to compare the 2D PSFs and the lateral profiles obtained with both approaches in the case of the thin PSF. In this case our approach is better than the Fourier relation. Indeed this can be seen on the lateral profiles where our profile seems closer to the expected profile than with the Fourier relation. In our case the normalized correlation is equal to 99.96% and for Fourier relation 99.2%. Now the difference between the two approaches reaches nearly one percent. Of course this is not dramatically degrading the result for this particular case. But still, in the rest of the thesis, all apodization functions will be calculated with the back-propagation approach. Fourier relation will help us to give an interpretation of the shape of our apodization functions.

2.4 System approach validation

In order to validate completely our system approach the PSF and images obtained with the system approach and with the Field II program are compared more in detail. Both RF and envelope images of a small medium are shown.

2.4.1. Comparison of the point spread functions

Here a PSF having a particular shape has been used. In chapter 3 the reason why such a PSF has been used will be given. For the moment we try to focus on one particular question: How good is our system approach for simulating ultrasound images.

The PSF considered here has the following analytical expression

$$h(x,y) = \cos(2\pi u_x x)\cos(2\pi u_y y) e^{-\pi\left(\frac{x}{\sigma_x}\right)^2} e^{-\pi\left(\frac{y}{\sigma_y}\right)^2} \tag{2-25}$$

This PSF is separable in the axial and lateral directions. In each direction, the profile is a sinusoid multiplied by a Gaussian envelope. u_x and u_y are the lateral and axial oscillations spatial frequencies and σ_x and σ_y are the standard deviations of the Gaussian envelopes. Those variables have the following values, $\lambda_y = \frac{1}{u_y} = 0.11\,\text{mm}$, $\lambda_x = \frac{1}{u_x} = 2.6\,\text{mm}$ and $\sigma_x = 0.32\,\text{mm}$, $\sigma_y = 2.7\,\text{mm}$

Figure 2-15 gives the exact shape of this PSF.

In order to obtain the PSF given by the Field II program, first all raw data have been calculated. The probe that has been used is the same as for the previous simulations. The dynamic apodization function has been calculated using back-propagation and dynamic quadratic focusing has been used. The obtained PSF is shown in Figure 2-15.

Figure 2-17 gives a comparison between axial and lateral profiles taken at different depths and lateral positions of the system and Field II point spread functions.

The first important thing to notice is the change in axial wavelength between the two approaches. This is seen qualitatively in the axial profiles (e), (f) and (g). The solid profiles are in advance at the top of the PSF and at the bottom the dotted profiles are in advance. This has also an impact on the lateral profiles. As there is always a small delay between the axial profiles, the lateral profiles don't correspond exactly to each other.

Moreover it is important to notice the curvature present in the front of the PSF obtained with Field II, Figure 2-16. This curvature cannot be modeled with a separable PSF. This is one sign that our model is simplified compared to a real acoustic model. However the normalized correlation between the two PSF is 82% and qualitatively the two PSF look really like each other.

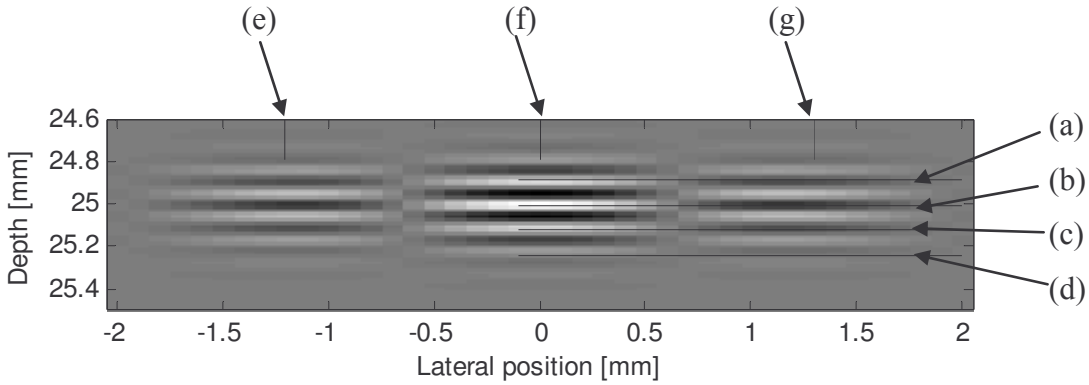

Figure 2-15: PSF of a scatterer at depth 25 mm obtained with the system approach. Figure 2-17 gives a comparison between the lateral profiles of the depths indicated (a), (b), (c) and (d) and the axial profiles of the lateral positions indicated (e), (f) and (g) with those of Figure 2-16.

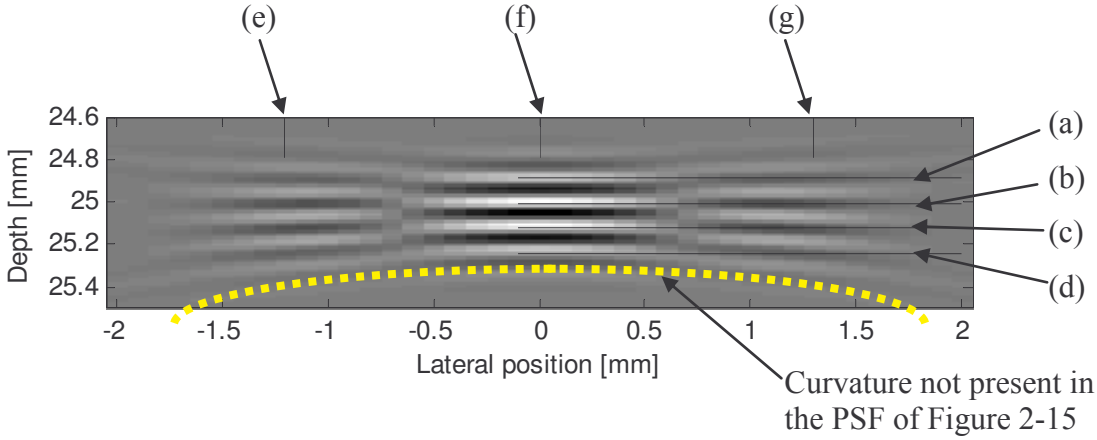

Figure 2-16: PSF of a scatterer at depth 25 mm obtained with Field II. Figure 2-17 gives a comparison between the lateral profiles of the depths indicated (a), (b), (c) and (d) and the axial profiles of the lateral positions indicated (e), (f) and (g) with those of Figure 2-15. Note that a curvature of the PSF is present here and not in the PSF of Figure 2-15

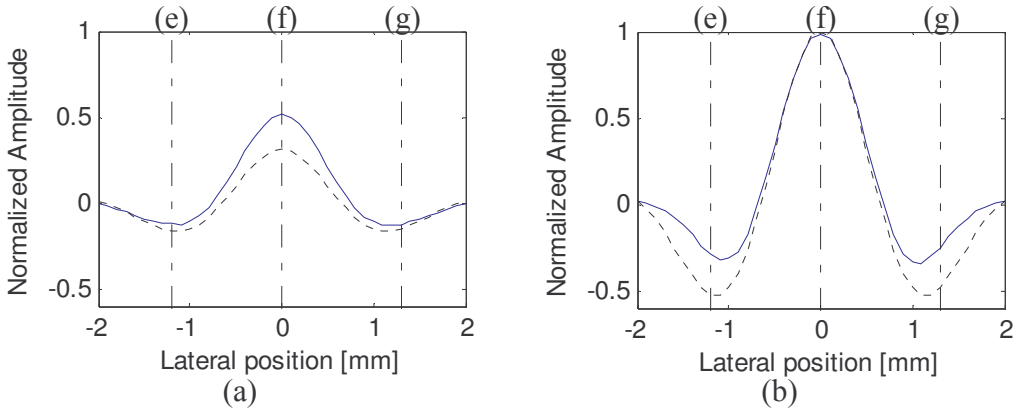

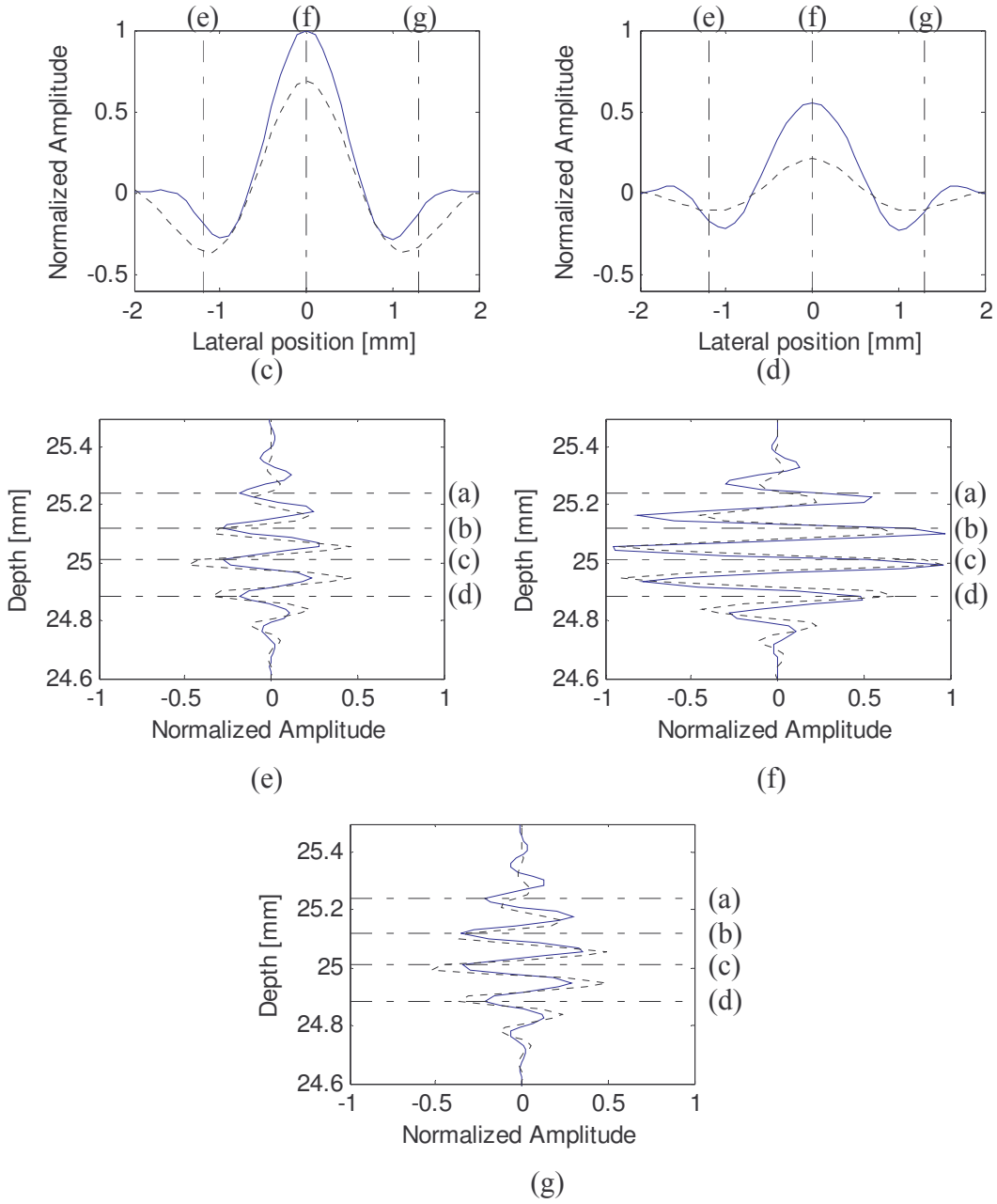

Figure 2-17: Comparison between the lateral profiles indicated (a), (b), (c) and (d) and the axial profiles indicated (e) (f) and (g) in Figure 2-16 and Figure 2-15. The solid line corresponds to the profiles coming from the Field II image, the dotted line from our approach. The interrupted lines give the positions of all different profiles represented.

2.4.2. Comparison between RF and envelope images obtained with the two approaches

A comparison between two images obtained one with Field II and the other one with our system approach is given.

A 2D medium of 4x5 mm composed of 500 scatterers having a random position and a Gaussian scattering coefficient distribution has been used. In our system approach the image is obtained directly by convolution between the PSF and the medium. For the Field images the raw data are first calculated, and then they are beamformed.

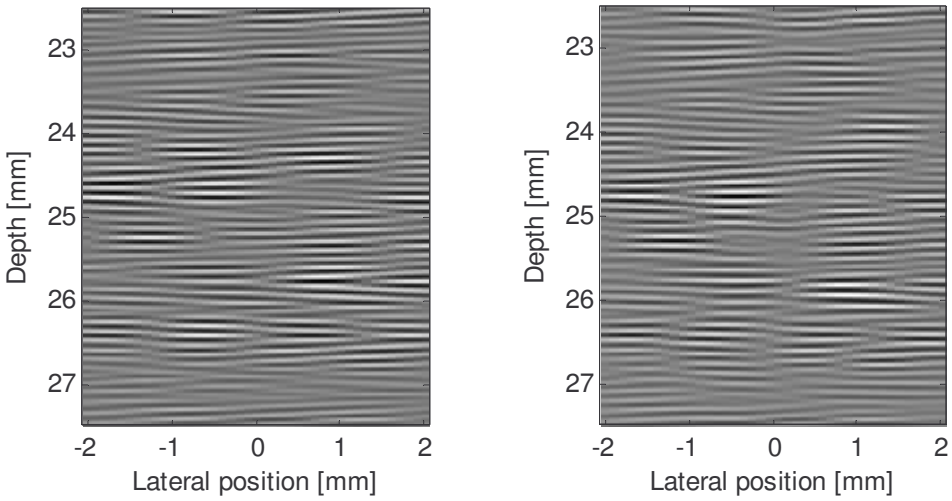

Figure 2-18: RF images obtained with the system approach and with the Field II program with the same scatterer distribution. (a) system approach, (b) Field II.

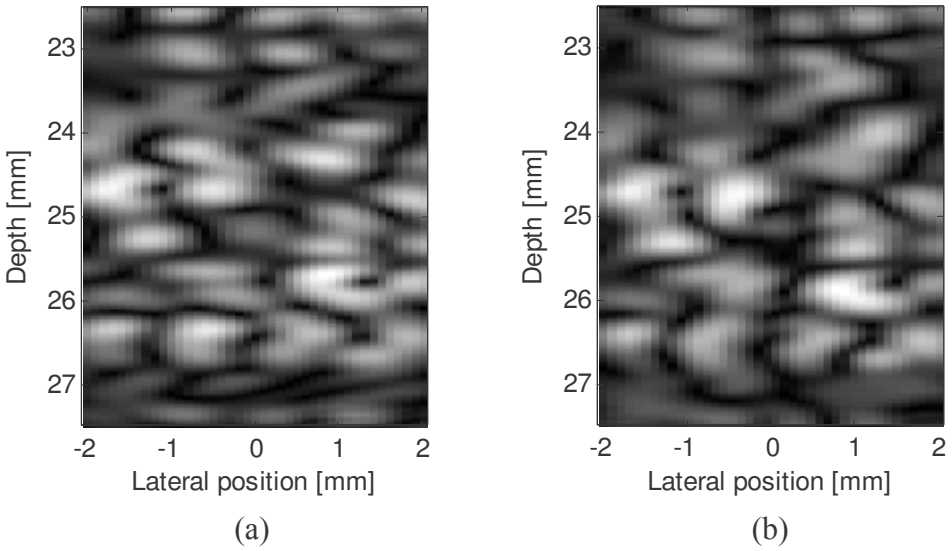

Figure 2-19: Envelope images obtained with the system approach and with the Field II program with the same scatterer distribution, (a) system approach, (b) Field II.

Figure 2-18 and Figure 2-19 show the obtained RF images and the obtained envelope images. As expected with the comparison of the PSF, there are small differences. This could be predicted because the PSFs were not exactly identical. But the main patterns can clearly be recognized both in the envelope and in the RF image.

This comparison has shown a few interesting things. The first one is that the beamformer design enables to obtain point spread functions that are extremely close to the expected ones. And what is even more interesting is that the images obtained by simple convolution between the PSF and the scatterer distribution is really similar to the one obtained with Field. And the results would probably be even more close to each other if the exact analytical expression of the PSF could be known.

As a consequence our approach is used to simulate the ultrasound images in the rest of the thesis, because it is a good tool as long as the PSF is completely controlled.

In the next chapter a particular beamformer will be presented that makes it possible to adapt the image characteristics to the requirements of a particular displacement estimation method.

Chapter 3

Lateral displacement estimation using the twice 1D approach

3.1 Introduction

In chapter 1, different approaches to multi-dimensional displacement estimation for ultrasound imaging have been presented. In this chapter a new approach will be presented, based on the study of the phase of the complex correlation between a reference and a delayed or displaced signal. This approach has been used for axial displacement estimation in ultrasound imaging by Pesavento *et.al.* [17]. More recently, Xunchang Chen *et.al.* in [12] have used a method similar to this approach but for the lateral direction. Their method works with classical ultrasound images, which is an important advantage. The aim of our approach is to improve the quality of the lateral estimation obtained with this method. This is done by considering the image formation and changing it in order to adapt it to the estimation method. It will be seen in this chapter how changing the image formation improves the accuracy of the estimation.

In this chapter first the iterative estimation of the lateral displacement using the Newton method will be presented. It will be shown how this approach leads to the use of lateral signals with particular spectral characteristics. It will also be shown how a particular beamformer can affect those characteristics. The improvement due to the new beamformer is illustrated with simulation results.

Then, the lateral displacement estimation is included to form a "twice 1D" scheme which is able of estimating the axial and the lateral components of the displacement. The principle of the method is presented as well as the specific ultrasound images used for both directions.

The beamformer and estimation parameters are then optimized according to the physical limitation of our probe. Simulation results are given for the parameters of our probe for both conventional images

and adapted images. A result is given for an even more optimized case where the same characteristics are used for both directions of the PSF. Unfortunately this case cannot be reached experimentally because of the limited size of the probe.

3.2 Lateral RF signals

As this work has been focused on the lateral displacement estimation the study of the shape of the lateral profiles of the ultrasound images will first be done. Those profiles will be called lateral RF signals. One lateral RF signal is composed of all samples coming from the same depth in the ultrasound RF image.

It is possible to make a very simple model for the formation of the lateral RF signals by making the same kind of approach as the one given in chapter 2 for the formation of the whole image.

Both azimuthal dimension (*i.e.* perpendicular to the image plane) and depth are considered to be fixed, *i.e.* $z = z_0$ and $y = y_0$, and in order to lighten the equation they won't be written anymore.

Let's first consider the medium. It will be assumed to consist of a discrete 1D distribution of N scatterers, $d(x)$ spatially uncorrelated and expressed as

$$d(x) = \sum_{i=1}^{N} A_i \delta(x - x_i) \tag{3-1}$$

where x_i is the position of the ith scatterer. It is a random variable having a uniform distribution [48]. The amplitude A_i can be random Gaussian distributed.

A 1D PSF reduced to its lateral profile $h(x)$ is defined. The reference lateral signal $r(x)$ is equal to the convolution between the scatterer distribution and the point spread function

$$r(x) = h(x) \underset{x}{\otimes} d(x) \tag{3-2}$$

A region of the medium $[x, y, z] \in \Omega$ is considered where the PSF is constant and the medium has been moved uniformly by a given lateral displacement vector $\boldsymbol{\Delta} = [\Delta x, 0, 0]$. The new distribution of scatterers $d'(x)$ is simply given by

$$d'(x) = d(x - \Delta x) \tag{3-3}$$

The new lateral signal $s(x)$ (strain signal) is the convolution between this distribution and the PSF as

$$s(x) = h(x) \underset{x}{\otimes} d'(x) \tag{3-4}$$

It can be expressed as a function of the initial distribution $d(x)$ as

$$s(x) = h(x) \underset{x}{\otimes} d(x - \Delta x) \tag{3-5}$$

Finally, it can be given as a function of the reference signal $r(x)$, as

$$s(x) = r(x - \Delta x) \tag{3-6}$$

Equation (3-6) shows simply that the signal from the displaced medium is a displaced version of the original signal. This expression is equivalent to (2-12) which was given for a three-dimensional window of the image, whereas here it concerns just a signal.

Once again it is important to notice that this expression is true locally, in a region where both the PSF and the displacement vectors are constant.

3.3 Lateral displacement estimation using the Newton method

In order to estimate the lateral displacement using complex correlation it is necessary first to understand how the displacement influences the expression of the complex cross-correlation.

3.3.1. Complex cross-correlation and displacement

The complex cross-correlation between the reference signal and the strain signals, $\widetilde{R}_{rs}(X)$, is defined as

$$\widetilde{R}_{rs}(X) = R_{rs}(X) + jH_x\{R_{rs}(X)\} \tag{3-7}$$

with $R_{rs}(X)$ the classical cross-correlation between the two real signals $s(x)$ and $r(x)$ and $H_x\{R_{rs}(X)\}$ its Hilbert transform. The envelope of the complex cross-correlation between the two signals is maximal for the displacement value Δx. For this particular value, the phase is equal to zero as follows

$$\arg\max_X \left|\widetilde{R}_{rs}(X)\right| = \Delta x \tag{3-8}$$

$$\Phi\left(\widetilde{R}_{rs}(\Delta x)\right) = 0 \tag{3-9}$$

This means simply that in order to find the right displacement there are two possibilities. It is possible to seek for the maximum of the envelope of the complex correlation. If this approach is chosen, it is not useful to calculate the complex correlation simply because the correlation between real signals has exactly the same property to be maximal for the right displacement.

The real interest of working with complex signals is to focus on the phase information. Indeed the phase of the complex correlation function crosses zero at the same position as the envelope or the real part is maximal. It is then possible to estimate the displacement by seeking for the zero crossing of the phase. This can be done faster and with a better accuracy than seeking for the absolute maximum of the cross-correlation [17]. In order to achieve this task, one possibility is to use the Newton method.

3.3.2. Newton method

The Newton method is an iterative method that is able to converge very quickly to the zero crossing of a given function. In our case the position of the zero crossing of the phase of the complex correlation is expected.

The expression of the estimate of the position of the zero crossing of the function at a particular iteration number $\hat{\Delta}^{i+1}x$ is given as a function of the previous estimate $\hat{\Delta}^{i}x$, the value of the function at the previous iteration $\Phi\left(\widetilde{R}_{rs}(\hat{\Delta}^{i}x)\right)$ and its derivative $\Phi'\left(\widetilde{R}_{rs}(\hat{\Delta}^{i}x)\right)$ as

$$\hat{\Delta}^{i+1}x = \hat{\Delta}^{i}x - \frac{\Phi\left(\widetilde{R}_{rs}(\hat{\Delta}^{i}x)\right)}{\Phi'\left(\widetilde{R}_{rs}(\hat{\Delta}^{i}x)\right)} \tag{3-10}$$

The estimation can be seen as follows. First the function is evaluated at one point. Then the tangent of the function at this particular point is calculated. This is the reason for the derivative to appear in (3-10) because the derivative of a function is equal to the slope of the tangent. Then the zero crossing of the tangent is calculated. This zero crossing is then used as starting point for another loop like this one (evaluation of the function, of its tangent and zero crossing of the tangent). This enables to reach the zero crossing of the function very quickly as seen in Figure 3-1.

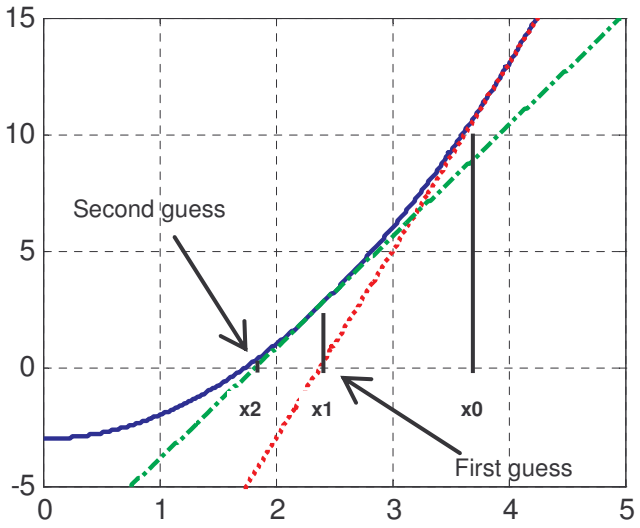

Figure 3-1: Principle of Newton method. The zero-crossing of a function (solid line) is expected. Two iterations are presented. The initial point is at the abscise x0 and the two first estimates are x1 and x2. The first tangent is in dotted line and the second one in dashed-dotted line.

The Newton method can be very efficient, but its result also depends on the shape of the function. The Newton method works with first order approximations of the function (the tangents). As a consequence one iteration would be enough to find the solution if the function was a simple line.

Newton method has been implemented for axial displacement estimation between ultrasound images by Fromageau and Delachartre [62]. They have been working with the zero-crossing of the imaginary part of the complex correlation. Indeed it is well known that the imaginary part of the complex correlation between real signals is an odd function which crosses zero at the same position as the

phase. But it seems more interesting to work with the phase because it can be controlled very easily as will be seen next.

The phase of the complex correlation will be forced to be linear and the consequences on the lateral RF signals of such a choice will be studied.

3.4 Linear phase of the complex cross-correlation and consequences for the lateral RF signals.

The phase of the complex correlation crosses zero at $X = \Delta x$. If the phase is assumed to be linear, it can be expressed as

$$\Phi\left(\widetilde{R}_{rs}(X)\right) = -2\pi u_x (X - \Delta x) \tag{3-11}$$

Equation (3-11) is simply that of a line that crosses zero at $X = \Delta x$ with a slope equal to $-2\pi u_x$. As will be seen later, u_x can be interpreted as a carrier frequency for the lateral signals. As only the phase has an important shape, any function could be used for the envelope of the correlation.

As this kind of function can be easily produced and as it is convenient to manipulate analytically, the envelope for the complex correlation is chosen to be Gaussian. This envelope is expressed as:

$$\left|\widetilde{R}_{rs}(X)\right| = \frac{\sigma_u}{\sqrt{2}} e^{-\pi\left(\frac{\sigma_u}{\sqrt{2}}(X-\Delta x)\right)^2} \tag{3-12}$$

Using (3-11) and (3-12), the whole expression of the complex correlation can be given by

$$\widetilde{R}_{rs}(X) = \frac{\sigma_u}{\sqrt{2}} e^{-\pi\left(\frac{\sigma_u}{\sqrt{2}}(X-\Delta x)\right)^2} e^{-j2\pi u_x (X-\Delta x)} \tag{3-13}$$

As the two signals considered are simply displaced versions from each other, as can be seen in equation (3-6), the complex cross-correlation is a displaced version of the complex auto-correlation as

$$\widetilde{R}_{rs}(X) = \widetilde{R}_{rr}(X) \underset{X}{\otimes} \delta(X - \Delta x) \tag{3-14}$$

with $\widetilde{R}_{rr}(X)$ the complex auto-correlation of the reference signal. From equations (3-13) and (3-14) the expression of the auto-correlation can be deduced as

$$\widetilde{R}_{rr}(X) = \frac{\sigma}{\sqrt{2}} e^{-\pi\left(\frac{\sigma_u}{\sqrt{2}}X\right)^2} e^{-j2\pi u_x X} \tag{3-15}$$

The spectral density of a signal is defined as the Fourier transform of its auto-correlation function. $P_{\tilde{r}}(u)$, the spectral density of the complex reference signal $\tilde{r}(x)$, is equal to the Fourier transform of (3-15) and is given by

$$P_{\tilde{r}}(u) = e^{-2\pi\left(\frac{u}{\sigma_u}\right)^2} \underset{u}{\otimes} \delta(u - u_x) \tag{3-16}$$

where u denotes the spatial frequency variable in the lateral direction.

The envelope of the spectrum of the analytical signal $\left|\widetilde{R}(u)\right|$ is equal to the square root of the spectral density. The square root of (3-16) is equal to

$$\left|\widetilde{R}(u)\right| = e^{-\pi\left(\frac{u}{\sigma_u}\right)^2} \underset{u}{\otimes} \delta(u - u_x) \tag{3-17}$$

Finally the modulus of the bilateral spectrum of the real signal $\left|R(u)\right|$ can be deduced as

$$\left|R(u)\right| = \tfrac{1}{2} e^{-\pi\left(\frac{u}{\sigma_u}\right)^2} \underset{u}{\otimes} \left(\delta(u - u_x) + \delta(u + u_x)\right) \tag{3-18}$$

As the scatterer distribution $d(x)$ is assumed spatially uncorrelated, its auto-correlation $R_{dd}(X)$ is a delta function, and its spectral density $P_d(u)$ is equal to 1, as well as the modulus of its spectrum $\left|D(u)\right|$ as

$$R_{dd}(X) = \delta(X) \tag{3-19}$$

$$P_d(u) = 1 \tag{3-20}$$

$$\left|D(u)\right| = 1 \tag{3-21}$$

According to (3-2) it can be written that

$$\left|R(u)\right| = \left|H(u)\right|\left|D(u)\right| \tag{3-22}$$

and finally using (3-21) gives

$$\left|R(u)\right| = \left|H(u)\right| \tag{3-23}$$

Equation (3-23) indicates that the modulus of the spectrum of the lateral signals is equal to the spectrum of the lateral profile of the PSF. There is no term corresponding to the medium in this expression.

In order to satisfy the choice of the complex correlation (3-13) it is necessary to design the beamformer in order to have

$$\left|H(u)\right| = \tfrac{1}{2} e^{-\pi\left(\frac{u}{\sigma_u}\right)^2} \underset{u}{\otimes} \left(\delta(u - u_x) + \delta(u + u_x)\right) \tag{3-24}$$

A number of functions satisfy (3-24) because no assumption is made for the phase of the spectrum. The following function is chosen

$$h(x) = e^{-\pi\left(\frac{x}{\sigma_x}\right)^2} \cos(2\pi u_x x) \tag{3-25}$$

with $\sigma_x = 1/\sigma_u$. In (3-25), σ_x will be called the standard deviation. It is equal to the width at half maximum of the Gaussian pulse. Here the notion of lateral wavelength is introduced. The lateral wavelength is the wavelength of the lateral oscillations. The lateral wavelength is denoted λ_x and is equal to $\lambda_x = 1/u_x$.

Equation (3-25) is composed of two terms. The exponential can be seen as an envelope, and the cosine represents a carrier with spatial frequency u_x. As a consequence it is possible to speak about lateral oscillations, because the lateral profile of the PSF has some oscillations. Jensen and Munk also used the concept of lateral oscillation as presented in chapter 1 [11].

This kind of lateral PSF profiles is not really common, and a particular beamformer has to be used in order to reach this shape. As a first approach, the shape of the apodization functions that leads to this kind of lateral PSF profiles is given using the Fourier relation.

The inverse Fourier transform of a Gaussian envelope multiplied by a cosine, is the convolution between a Gaussian and two delta functions. Using the Fourier relation given in (2-23) the apodization would be given by:

$$w(x_i) = \tfrac{1}{2} e^{-\pi\left(\frac{x_i}{\sigma_0}\right)^2} \underset{u}{\otimes} \left(\delta(x_i - x_0) + \delta(x_i + x_0)\right) \tag{3-26}$$

where x_i is the lateral position on the aperture, σ_0 is the standard deviation of each peak and $\pm x_0$ their position. The standard deviation and the position of the peak can be related to the PSF parameters of (3-25) at any depth y as

$$x_0 = \lambda y u_x = \frac{\lambda y}{\lambda_x} \tag{3-27}$$

$$\sigma_0 = \frac{\lambda y \sqrt{2}}{\sigma_x} \tag{3-28}$$

with λ being the wavelength of the emitted ultrasound wave. Figure 3-2 shows a sketch of the PSF profile and the apodization profile. It also identifies the four parameters in equations (3-27) and (3-28).

The apodization function of (3-26) is close to the one used by Jensen and Munk in [11]. In their case the apodization function was the convolution between two delta functions and a sinc function whereas for us the two delta functions are convolved with a Gaussian function.

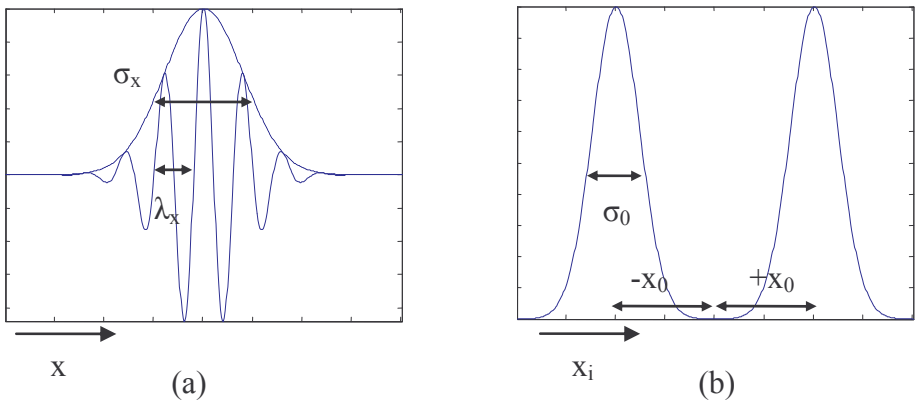

Figure 3-2: Representation of the different variables of the lateral profile of the PSF (a) and the apodization function (b). The relation between x_0 and $u_x = 1/\lambda_x$ is given in (3-27). The relation between σ_0 and σ_x is given in (3-28). The apodization function is a function of x_i the lateral position on the probe. The lateral profile of the PSF is a function of the lateral position x. The standard deviations are equal to the width at half maximum of the Gaussian envelopes.

Even if the Fourier relation helps to understand the shape of the apodization, the parameters of the beamformer are calculated using the method presented in chapter 2, the back-propagation of the expected profile.

As an illustration, two examples of point spread functions having the expected shape of (3-25) are given. Each example has a different pair of parameters u_x and σ_x.

As for the point spread functions of Chapter 2, the simulation results to be presented here have been obtained with Field II [16], [52]. Probe (BK Medical 8804 linear array probe) and parameters were identical to the ones given in Table 1.

In the first example, the expected PSF is supposed to have a lateral wavelength of $\lambda_x = 1.5$ mm and its envelope is a Gaussian, (3-25), of standard deviation $\sigma_x = 1.875$ mm. The two-dimensional PSF is shown in Figure 3-3. In Figure 3-4 the obtained lateral profile can be seen as a solid line as well as the expected lateral profile in dotted line. A difference can be seen between the expected profile and the obtained one, but this is still related to some assumptions that are made in order to calculate the apodization function (monochromatic waves etc…). The aperture function that enables to obtain this PSF is given in Figure 3-5. This profile has been calculated with the back-propagation method.

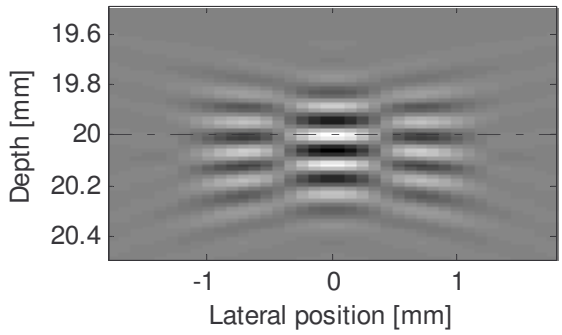

Figure 3-3: 2D RF point spread function obtained with the apodization function of Figure 3-5. The dashed-dotted line gives the depth of the profile in Figure 3-4. (Data obtained with Field II)

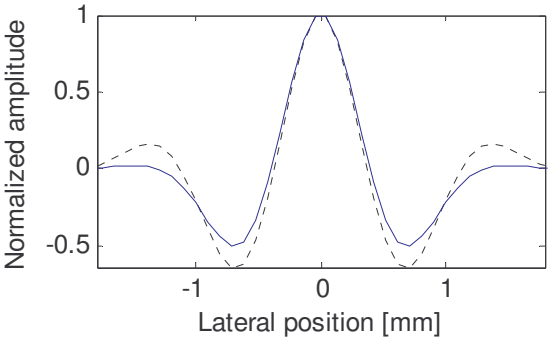

Figure 3-4: Lateral PSF profiles obtained with the apodization function of Figure 3-5. The profile obtained with the apodization function given by the backpropagating method (2-19) is shown as a solid line and the expected one given in (3-25) is shown as a dotted line.

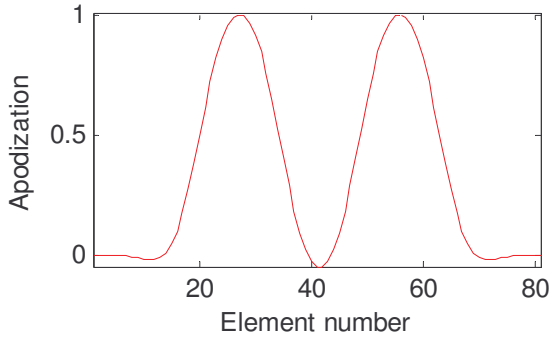

Figure 3-5: Apodization function used to obtain the PSF profile (3-25), having a lateral wavelength of $\lambda_x = 1.5$ mm and a standard deviation of its Gaussian envelope of $\sigma_x = 1.875$ mm

Two peaks are clearly identified in Figure 3-5 which is coherent with what is expected from Fraunhoffer approximation even if the envelope of the peaks does not appear strictly as a Gaussian. The number of elements having a significant weight is around 70.

It is interesting to have a short look on the consequence for the apodization function of an increase of u_x and a decrease of σ_x. Those changes are interesting because they should both correspond to an increase in the quality of the estimation (as will be seen later on). A higher frequency increases the slope of the phase which should lead to a better estimate. And a smaller standard deviation should lead to a better spatial resolution.

Specifically, in the second example the carrier frequency has been multiplied by a factor of three compared to the previous example and the width at half maximum of the envelope σ_x has been divided by three. Here the expected PSF is supposed to have a lateral wavelength of $\lambda_x = 0.5$ mm and its Gaussian envelope has a width at half maximum of $\sigma_x = 0.625$ mm.

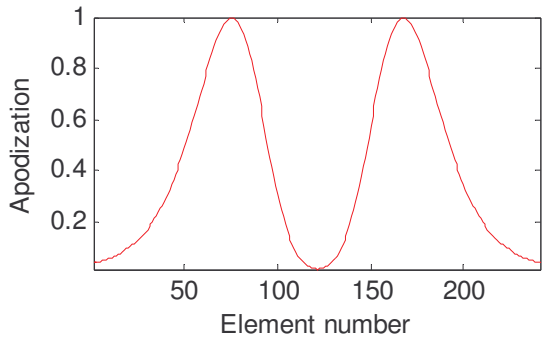

Figure 3-6: Apodization function used to obtain the PSF profile (3-25), having a lateral wavelength of $\lambda_x = 0.5$ mm and a standard deviation of its Gaussian envelope of $\sigma_x = 0.625$ mm

The apodization function that leads to the expected PSF is given in Figure 3-6. The 2D PSF is given in Figure 3-7. The expected profile and the obtained profile are given in Figure 3-8. As for the previous example both profiles are very close to each other, which indicates one more time that our choice of beamformer design leads to proper results.

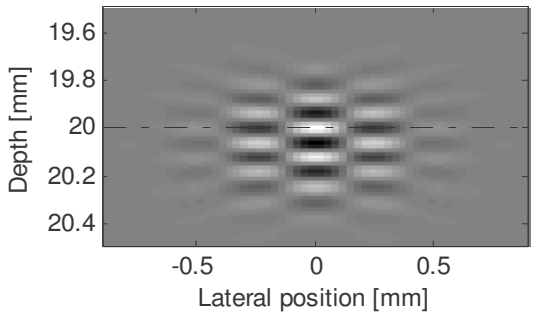

Figure 3-7: 2D RF point spread function obtained with the apodization function of Figure 3-6. The dashed-dotted line gives the depth of the profile of Figure 3-8.

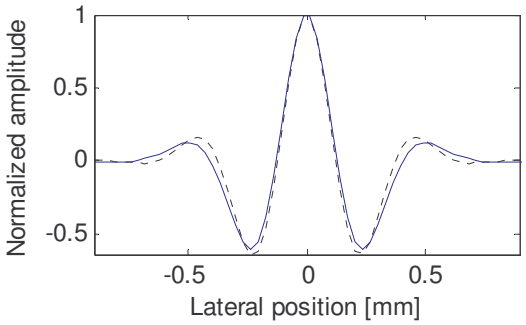

Figure 3-8: Lateral PSF profiles obtained with the apodization function of Figure 3-6. The profile obtained with the backpropagating method is shown as a solid line and the expected one given in (3-25) is shown as a dotted line.

It is clear in Figure 3-6 that the number of elements that have to be used this time is much more important than for the previous example. More that 210 elements have to be used. This is already an interesting aspect. Indeed the physical size of our probe will be a limitation, and not any PSF can be obtained.

As in the previous example two peaks are still present in the apodization function, but from a visual inspection, it is clear now that their shape is not Gaussian anymore: a Gaussian is symmetric but the peaks of Figure 3-6 are not symmetric. This shows that in this case Fraunhoffer approximation does

not apply well. As a consequence, (3-26), which gives the apodization function obtained with the Fourier relation, is not valid anymore.

In the next section the interest of using images with lateral oscillations obtained with our beamformer compared to conventional images for estimating lateral displacement, will be seen.

3.5 Potential of this beamformer for lateral displacement estimation, compared to classical beamformer

Recently, Xunchang Chen *et.al.* have published a paper [12], that shows how it is possible to estimate lateral displacements by working with *synthetic lateral phase*. Their method is based on the observation that complex correlation between conventional images can show some kind of phase information in the lateral direction. This is of course extremely interesting because it doesn't necessitate any particular beamformer.

However, it will be shown that having a beamformer that leads to a linear phase of the complex correlation in the lateral direction improves the accuracy of the lateral displacement estimation.

In order to do this a comparison between the results from two cases obtained in simulation are presented. First a classical PSF having a Gaussian lateral profile, leading to what will be called *conventional images* will be simulated. Then our PSF having lateral oscillations (LO) is used. First the shape of both the envelope and the phase of the complex auto-correlation functions of the two PSFs are shown.

3.5.1. Envelope and phase of complex auto-correlation of the two PSFs

For the conventional images, the classical PSF, $h_1(x)$ is given by (2-22) with $\sigma_x = 1.4$ mm. For the lateral oscillations (LO), the PSF $h_2(x)$ is given by (3-25) with $\sigma_x = 2.8\,\text{mm}$ and $\lambda_x = 2.6\,\text{mm}$. The depth is chosen equal to 30 mm. The parameters of the elements of the probe are those of Table 1. The two apodization functions are called $w_1(x)$ and $w_2(x)$. All those functions are given in Figure 3-9.

In the whole section, the solid line corresponds to the conventional PSF and the dotted line to the lateral oscillations.

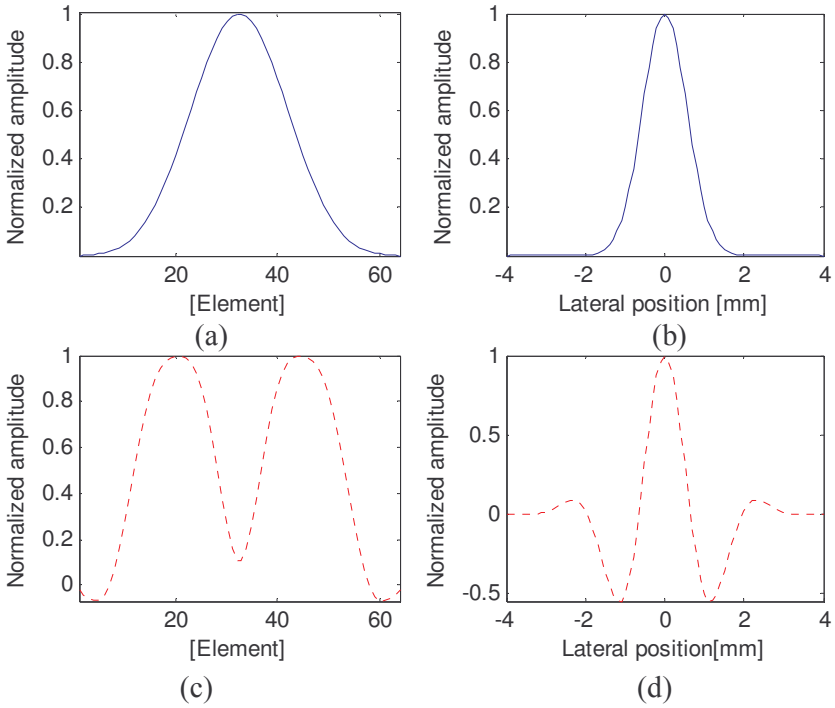

Figure 3-9: (a) shows w1, the apodization functions for the conventional PSF, (c) shows w2, the apodization functions for the lateral oscillations PSF, (b) shows h_1 the lateral profile of the conventional PSF and (d) h2 shows the lateral profile of the lateral oscillations PSF.

The complex auto-correlation functions of the PSF profiles are calculated in both cases. The envelope and phase of those functions can be seen in Figure 3-10.

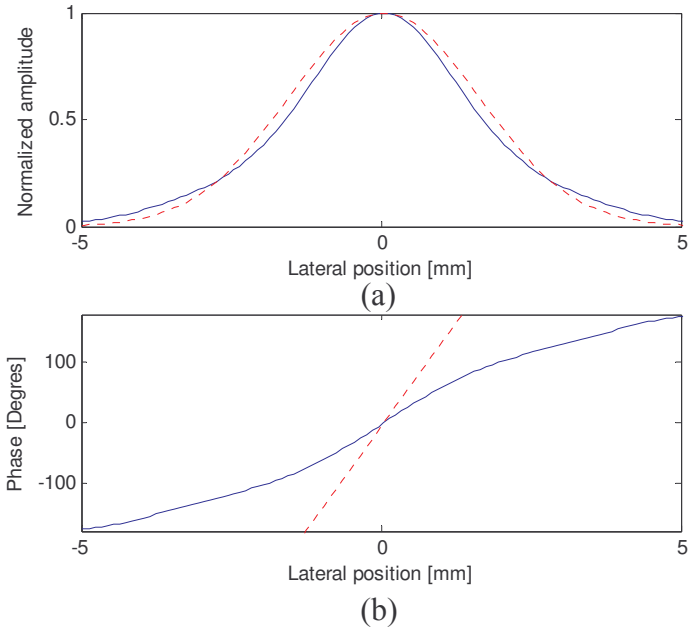

Figure 3-10: (a) shows the envelope of the complex auto-correlation functions, (b) shows the phase of the complex auto-correlation functions. The solid line is used for conventional PSF and the dotted line for lateral oscillations. PSF

In both cases the envelope is maximal and the phase is equal to zero at zero lag. This is in agreement with (3-8) and (3-9). However, for the conventional PSF, the phase is not linear, whereas it is the case

for the lateral oscillations PSF. More over, around zero, the slope of the phase of the lateral oscillations PSF is steeper than for the conventional PSF. Indeed for the classical PSF it is around 57°/mm and for the lateral oscillations it is around 131°/mm. This should lead to a better estimation of the zero crossing of the phase in the case of the lateral oscillations.

This will be illustrated next.

3.5.2. Improvement due to lateral oscillations in presence of noise

In order to show that estimation of the displacement using zero crossing of the phase is improved by using a particular PSF, a simulation has been done that enables to compare the performance of the estimation in presence of noise.

The same two point spread functions as in the previous section have been used. A random distribution of scatterers spatially uncorrelated and satisfying conditions presented in chapter 2 has been used. The lateral RF signals have been obtained by convolution between the scatterers and the point spread functions using (3-2).

First the Newton estimator has been tried in a case where the reference signal was compared to a noisy version of itself. The strain signal is expressed as

$$s(x) = r(x) + n(x) \tag{3-29}$$

where $n(x)$ represents zero mean white Gaussian noise. In this simulation the signal-to-noise ratio was controlled and varied from 2 to 50 dB. 500 realizations for each signal-to-noise ratio have been used. The mean estimate and standard deviation of the estimate for both cases are represented in Figure 3-11 as a function of the signal-to-noise ratio.

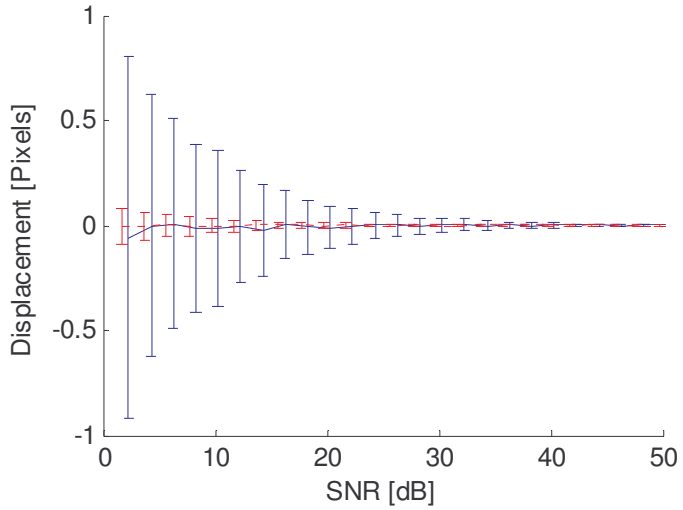

Figure 3-11: Mean estimate and standard deviation of the estimation as a function of SNR. The strain signal is simply the reference signal plus noise. The standard deviation for the lateral oscillations (dotted line) is between 8 and 9 times smaller than for the conventional PSF (solid line).

Figure 3-11 shows that for both cases the mean estimate is close to zero, which is the true displacement. However, the lateral oscillations lead to a smaller standard deviation. The standard deviation of the estimation for the lateral oscillations is between 8 and 9 times smaller than for conventional images, and this, for all SNRs. The lateral oscillation is a better solution.

A second simulation has been done with, this time, estimation between the reference signal and the second signal being a displaced noisy version of the reference signal as

$$s(x) = r(x - \Delta x) + n(x) \tag{3-30}$$

The displacement Δx has been chosen equal to 1 pixel which corresponds to 0.1mm in our simulation. This distance can also be compared to the size of the point spread function. For the conventional PSF it represents roughly 10% of σ_x and for the lateral oscillations, it represents roughly 20% of σ_x. With the expression of the Gaussian function that is used, σ_x is nearly the full width at half maximum of the Gaussian function. As for the previous simulation the SNR was between 2 and 50 dB and 500 realizations have been used. The results are plotted in Figure 3-12.

As for the case with only noise, the standard deviation in the case of the lateral oscillations is around 9 times smaller than for the classical PSF.

Those two simulations really show the potential of controlling the shape of the PSF by using lateral oscillations instead of using conventional images.

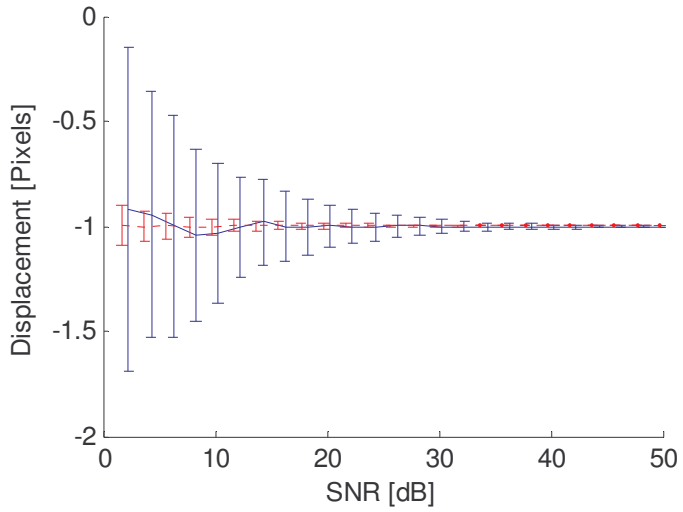

Figure 3-12: Mean estimate and standard deviation of the estimation as a function of SNR. The strain signal is calculated using (3-30). The standard deviation for the lateral oscillations (dotted line) is roughly 9 times smaller than for the classical PSF (solid line).

The next step is to introduce the lateral estimation in a whole 2D displacement algorithm. This is presented in the next section.

3.6 2D displacement estimation using a “twice 1D” approach

The lateral displacement estimation presented previously is now introduced in the frame of a 2D displacement estimation. First the principle of the algorithm is presented.

3.6.1. Principle of the algorithm

In this section all aspects of the 2D estimation algorithm are presented.

Adapted windowing

In order to have a local estimation of the displacement, it is necessary to work with parts of the images having a limited size. Those limited regions are called windows. In this twice 1D scheme, the windows are 1 dimensional windows composed of a certain number of pixels taken either in the axial or in the lateral direction of the image. The central position of the axial and lateral windows is the same point and is called the position of the windows. The principle of the windows is shown in Figure 3-13.

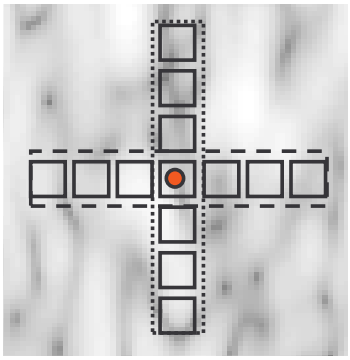

Figure 3-13 : Axial 1D window (dotted line) and lateral 1D window (dashed line). In this example the size of the windows in the axial and lateral directions is the same; there are 7 samples in each direction. The position of the windows is marked by a dot.

The position of the windows in the reference and strain images is extremely important. The displacement has to be estimated between parts of the image corresponding to the same parts of the medium.

The positions of the windows in the reference image are situated on a regular grid. This grid is represented in Figure 3-14. The estimation begins with the point of interest on the top of the image in the central column. This point is denoted A. For this first estimation, the position of the windows in the strain image is centered on A', which has the same position as A in the first image. The first displacement vector is estimated.

Then the next points of interest are chosen in order to form a line around the initial point of interest. Once the displacement is estimated for all points of this line, a next one is selected, and so on until all points of interest in the initial image have been selected. The lines are chosen as described in Figure 3-14.

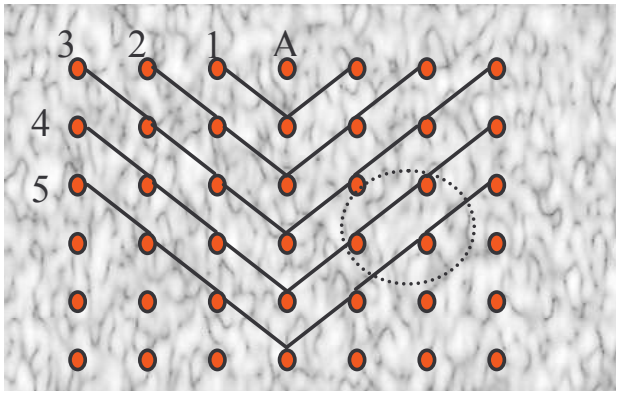

Figure 3-14: Regular grid in the reference image. First the displacement of point A is estimated. Then the displacement for the points of the line number 1 are estimated, then for those of line number 2, 3, 4 etc...The dotted region is considered in Figure 3-15.

In order to estimate the displacement correctly, the position of the point of interest in the strain image takes into account the displacement of the neighbor points estimated previously. This is done in order to always estimate displacement between windows corresponding to the same part of the medium.

For the lateral direction, the displacement estimated previously for the point on the left or on the right of the point of interest is used (depending if the point of interest is on the left part or on the right part of the image). For the axial direction it is the displacement of the point above which is used. This is easier to understand with an example. Let's consider the three points K, L and M of Figure 3-15.

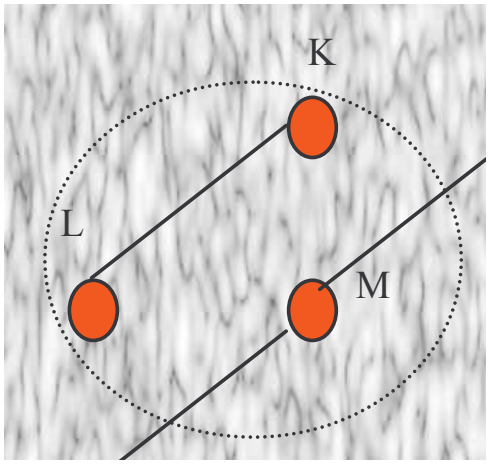

Figure 3-15: Points used for the example. The displacement vectors of the points K and L have already been estimated. They will be used for the estimation of the displacement of point M.

Assume that the displacement of point K and the displacement of point L have been estimated previously. Those two displacement vectors are denoted $\mathbf{\Delta_K}$ and $\mathbf{\Delta_L}$ and are defined as

$$\mathbf{\Delta_K} = (\Delta x_K, \Delta y_K) \tag{3-31}$$

$$\mathbf{\Delta_L} = (\Delta x_L, \Delta y_L) \tag{3-32}$$

The point of interest M', of coordinate vector $\mathbf{M'} = (x_{M'}, y_{M'})$, in the strain image has to be selected by taking into account the displacement estimated previously for his neighbor points. As explained, the coordinates will be selected according to

$$x_{M'} = x_M + \Delta x_L \quad (3\text{-}33)$$

$$y_{M'} = y_M + \Delta y_K \quad (3\text{-}34)$$

This means also that, if the displacement is equal to zero for a given point, the position of the windows in the second image is equal to the position of the windows in the reference image. And if the displacement is equal to zero for the whole image, the points of interest in the strain image will be on the identical regular grid as the one used for selecting the points of interest in the reference image.

Local estimation

Two sets of images are considered. The next section explains how they are obtained. Let's consider for the moment that there are two reference images and two strain images. One set of images is used for the axial displacement estimation along direction y, the other one for the lateral displacement estimation along direction x. They will be called $s_y(x,y)$, $r_y(x,y)$, $s_x(x,y)$ and $r_x(x,y)$. The indices indicate the direction for which they are used.

The estimation is done for a point of interest P of coordinates (x_P, y_P) situated in the first image. As explained previously, the displacement already estimated for the neighbors of P are used in order to select $(x_{P'}, y_{P'})$, the coordinates of P', the point of interest in the strain image. The windows and their positions in the reference and strain images are illustrated in an example in Figure 3-16.

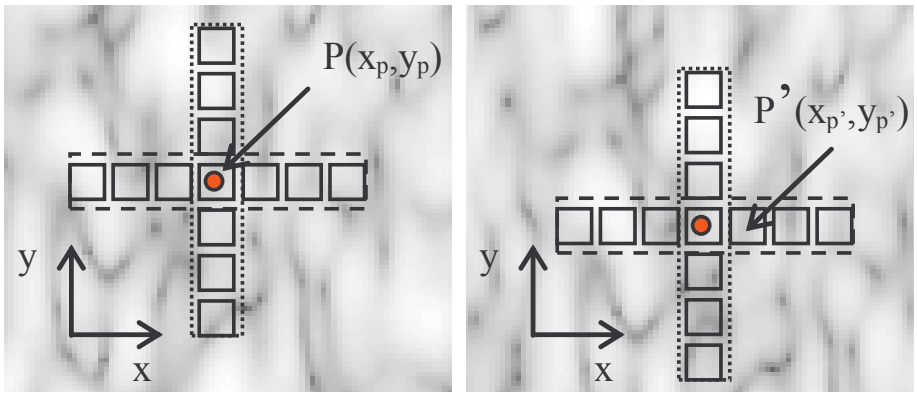

(a) (b)

Figure 3-16 : (a) is in the reference image, (b) is in the strain image. The position of the windows in the reference image is P, and in the strain image it is P'.

The axial displacement at position P is estimated by estimating the position of the zero crossing of the complex cross-correlation between axial RF signals taken in $s_y(x,y)$ and $r_y(x,y)$. The expression of the discrete complex correlation between those signals is given by

$$\widetilde{R}_{rs}(x_P, Y) = \sum_{i=-N}^{i=N} \widetilde{r}_y(x_P, y_P + i)\widetilde{s}_y(x_{P'}, y_{P'} + i + Y) \quad (3\text{-}35)$$

where 2N+1 is the length of the signals. In the example of Figure 3-16, 2N+1 is equal to 7. $\widetilde{r}_y(x_P, y)$ and $\widetilde{s}_y(x_{P'}, y)$ are complex signals given by

$$\tilde{r}_y(x_P, y) = r_y(x_P, y) + jH_y\{r_y(x_P, y)\} \quad (3\text{-}36)$$

$$\tilde{s}_y(x_{P'}, y) = s_y(x_{P'}, y) + jH_y\{s_y(x_{P'}, y)\} \quad (3\text{-}37)$$

$r_y(x_p, y)$ is an axial signal and $H_y\{r_y(x_p, y)\}$ its Hilbert transform in the axial direction.

The lateral displacement is estimated in an equivalent way using complex correlation between lateral RF signals. This time the position of the zero crossing along the lateral direction of the complex correlation is estimated. The complex correlation is expressed by

$$\tilde{R}_{rs}(X, y_P) = \sum_{k=-M}^{k=M} \tilde{r}_x(x_P + k, y_P)\tilde{s}_x(x_{P'} + k + X, y_{P'}) \quad (3\text{-}38)$$

Here the length of the signals is 2M+1. In the example of Figure 3-16, 2M+1 equals 7. $\tilde{r}_x(x, y_P)$ and $\tilde{s}_y(x, y_{P'})$ are complex signals given by

$$\tilde{r}_x(x, y_P) = r_x(x, y_P) + jH_x\{r_x(x, y_P)\} \quad (3\text{-}39)$$

$$\tilde{s}_x(x, y_{P'}) = s_x(x, y_{P'}) + jH_x\{s_x(x, y_{P'})\} \quad (3\text{-}40)$$

$r_x(x, y_P)$ is a lateral signal and $H_x\{r_x(x, y_P)\}$ its Hilbert transform in the lateral direction.

The progression of the algorithm has been described for the whole image, and the way the displacement is estimated at one particular point has also been described. Next the reason why two sets of images are needed is given. The method to obtain the two sets of images is also presented.

Specific images

At the beginning of this chapter it has been seen that using lateral oscillations PSFs enables to estimate more accurately lateral displacement using complex correlation than using conventional PSFs. On the other hand it has been shown in the literature that the phase of the complex correlation can be used for axial displacement estimation. However, different images have to be used for the two directions of estimation.

Indeed in a normal situation there is always displacement in both spatial directions. When estimating in one direction, the displacement that is present in the perpendicular direction should not affect the estimation. In other words, when estimating in one direction, the changes in shape of the signals should be slow in the other direction.

In order to reach this situation it is necessary to have images showing oscillations in the direction of estimation and slow variations in the other direction. This is naturally the case for classical RF images where Gaussian apodization is used for both emit and receive. The lateral profile of the PSF is then also Gaussian, and this makes classical images adapted for axial displacement estimation.

For the lateral direction it is more complicated. It is possible by beamforming to obtain images with lateral oscillations, but those images still contain axial oscillations. This is a real drawback for our method. As a consequence a heterodyning demodulation of the images will be used, in order to

suppress the axial oscillations. This is possible using a method introduced by Anderson in 2000 in [18]. The demodulation method is now recalled.

The relation is given for the point spread function. Let $h(x,y)$ be the PSF that will be demodulated. If $H_y\{\ \}$ and $H_x\{\ \}$ denote the Hilbert operators in the axial and lateral directions, respectively, the heterodyning demodulated PSF $h_d(x,y)$ as described in [18], is calculated using the following equations

$$h_{even}(x,y) = h(x,y) + jH_y\{h(x,y)\} \tag{3-41}$$

$$h_{odd}(x,y) = H_x\{h(x,y)\} + jH_y\{H_x\{h(x,y)\}\} \tag{3-42}$$

$$h_d(x,y) = \left(h_{even}(x,y) + jh_{odd}(x,y)\right)\left(\overline{h_{even}(x,y) - jh_{odd}(x,y)}\right) \tag{3-43}$$

The PSF given in (3-43) is complex and the final demodulated PSF is its real part.

The initial PSF is defined as

$$h(x,y) = \cos(2\pi u_x x)\cos(2\pi u_y y)e^{-\pi\left(\frac{x}{\sigma_x}\right)^2} e^{-\pi\left(\frac{y}{\sigma_y}\right)^2} \tag{3-44}$$

which is the kind of 2D PSF that can be produced with our beamformer. This is the expression of the lateral oscillations PSF. Then, (3-41), (3-42) and (3-43) can be approximated by

$$h_{even}(x,y) = \cos(2\pi u_x x)e^{-\pi\left(\frac{x}{\sigma_x}\right)^2} e^{-\pi\left(\frac{y}{\sigma_y}\right)^2} e^{j2\pi u_y y} \tag{3-45}$$

$$h_{odd}(x,y) = \sin(2\pi u_x x)e^{-\pi\left(\frac{x}{\sigma_x}\right)^2} e^{-\pi\left(\frac{y}{\sigma_y}\right)^2} e^{j2\pi u_y y} \tag{3-46}$$

$$h_d(x,y) = e^{-2\pi\left(\frac{x}{\sigma_x}\right)^2} e^{-2\pi\left(\frac{y}{\sigma_y}\right)^2} e^{j4\pi u_x x} \tag{3-47}$$

And the real part of (3-47)

$$R\{h_d(x,y)\} = e^{-\pi\left(\frac{x}{\sigma'_x}\right)^2} e^{-\pi\left(\frac{y}{\sigma'_y}\right)^2} \cos(2\pi u'_x x) \tag{3-48}$$

with $u'_x = 2u_x$, $\sigma'_x = \sigma_x/\sqrt{2}$ and $\sigma'_y = \sigma_y/\sqrt{2}$.

Remark: Relation (3-48) shows three important things. First the axial oscillations are not present anymore, which was the purpose of the processing. Second, the frequency of the lateral oscillations has been multiplied by a factor of two. Finally the standard deviations of the Gaussian envelopes of the PSF have been divided by $\sqrt{2}$ which makes the new PSF thinner in both directions.

Moreover the shape of the lateral profile of the PSF has not changed. It still has the form of (3-36) which is the shape that should lead to an accurate estimation. The fact that the central frequency is higher is also an advantage, because it will result in a steeper slope of the phase of the complex correlation.

Figure 3-17 and Figure 3-18 show an example of a PSF before and after heterodyning demodulation, respectively. The equation of the initial PSF is given in (3-44) with $u_x = 1.25\,\text{mm}^{-1}$, $u_y = 1.25\ \text{mm}^{-1}$, $\sigma_x = 1.5\,\text{mm}$ and $\sigma_y = 1.5\,\text{mm}$.

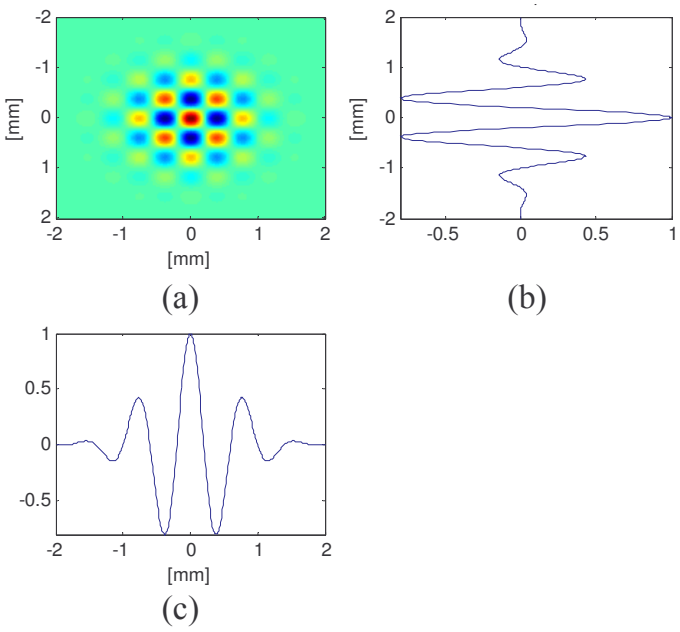

Figure 3-17: (a) Initial 2D PSF with axial (b) and lateral (c) profiles. This PSF shows axial and lateral oscillations.

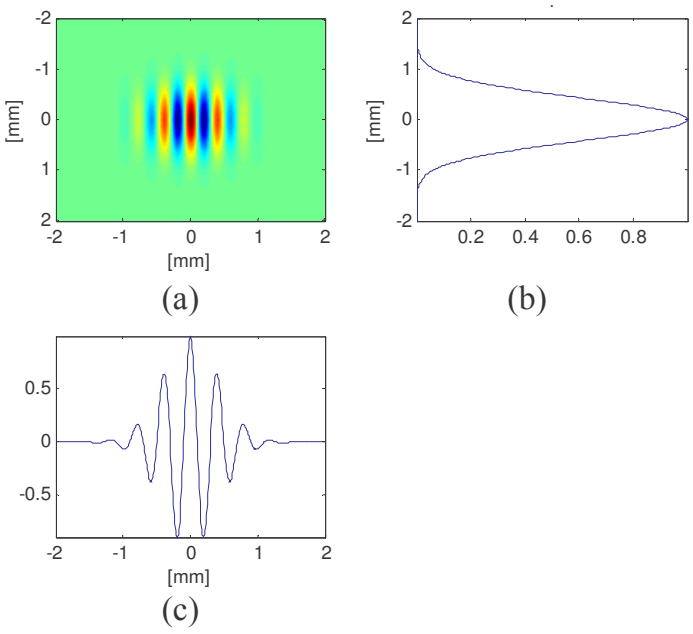

Figure 3-18: (a) Demodulated PSF with axial (b) and lateral (c) profiles. Compared to Figure 3-17, the axial oscillations are not present anymore, the lateral oscillations are twice faster and the lateral envelope is thinner by a factor $\sqrt{2}$

All bases for the 2D displacement estimation have been presented, and all key parameters are known. It is important now to fix all those parameters that will be used for the experiments of the next chapter.

3.6.2. Choice of the parameters

Three sets of parameters have to be chosen: the beamforming parameters related to the image formation; the medium parameters; the estimation algorithm parameters.

Imaging parameters

The shape of the lateral profile of the PSF has already been chosen. But both central frequency and standard deviation have to be chosen. Particularly, the physical size of the probe gives the limitation for those two parameters.

The Fourier relation provides easily access to the quantitative limitation of the probe. Let's first present this aspect qualitatively.

The frequency of the lateral oscillations is directly related to the position of the peaks in the aperture function. If the frequency has to be high, then the distance between the peaks increases. Of course, this distance can not be larger than the size of the aperture. For the standard deviation of the envelope of the two Gaussian pulses in the aperture function, the same qualitative approach can be made. If the envelope of the PSF is expected to be thin, then the peaks have to be wide.

It is not possible to give the width of the Gaussian pulses because they are infinite, but the criterion that 99% of the area under curve has to be inside the limits of the size of the probe will be used. With the expression of the Gaussian pulses, 99% of the surface under curve is between minus and plus 1.2 times the standard deviation.

The Fourier relation gives an aperture function equal to

$$w(x_i) = \tfrac{1}{2} e^{-\pi\left(\frac{x_i}{\sigma_0}\right)^2} \underset{x_i}{\otimes} \left(\delta(x_i - x_0) + \delta(x_i + x_0)\right) \tag{3-49}$$

with σ_0 the standard deviation of the Gaussian peaks and x_0 their position, x_i is the lateral position. The signification of the different parameters is given in Figure 3-2.

If W denotes the width of the aperture, combining the limit for the lateral frequency, and the one for the standard deviation leads to the following limitation:

$$1.2\sigma_0 + x_0 \leq \frac{W}{2} \tag{3-50}$$

The relation between the PSF parameters and the apodization function parameters is known and given in (3-27) and (3-28). The limitation for the aperture given in (3-50) can be expressed as a function of the parameters of the point spread function as

$$1.2\frac{\lambda y\sqrt{2}}{\sigma_x} + \frac{\lambda y}{\lambda_x} \leq \frac{W}{2} \tag{3-51}$$

with λ the wavelength of the emitted wave. All parameters are represented in Figure 3-2.

In order to choose the optimal parameters according to the size of our probe a simulation has been done using the system model to obtain the signals.

A reference signal and a strain signal are calculated using (3-2) and (3-4). This time, instead of applying a pure translation to the scatterer distribution, it has been stetched. The following equation gives the relation between the reference distribution of scatterers and the second distribution of scatterers

$$d'(x) = d\left((1 + \frac{\varepsilon}{100})x \right) \tag{3-52}$$

with ε the deformation in percents. In this case, the displacement is not the same for the whole window of interest. It is considered that the displacement that should be given by the estimator is the displacement from the sample in the middle of the window.

For example if a window has a size of 3 mm, with a strain of 1%, the displacement considered for the window is 15 μm.

In the simulation, values of σ_x between 1 and 8 mm and values of $\lambda_x = 1/u_x$ between 1 and 5.6 mm have been tested. For each pair of standard deviation and wavelength of the lateral PSF, 3000 realizations have been tested. This means that 3000 different random scatterer distributions and lateral RF signals have been generated and calculated. The displacement has also been estimated 3000 times. In order to choose the best couple of parameters, the mean quadratic error over the 3000 realizations is calculated for each couple. This error is normalized by the mean quadratic true displacement, which is the reason for the following figures to be in percents. The quadratic error is given by

$$E = (\Delta - \hat{\Delta})^2 \tag{3-53}$$

Of course, parameters that can be reached with our probe have to be chosen. The limitation is given in (3-51). As there are 64 active elements in our probe with a distance of 0.208 mm between two elements, the width of the aperture is equal to W=13.1 mm.

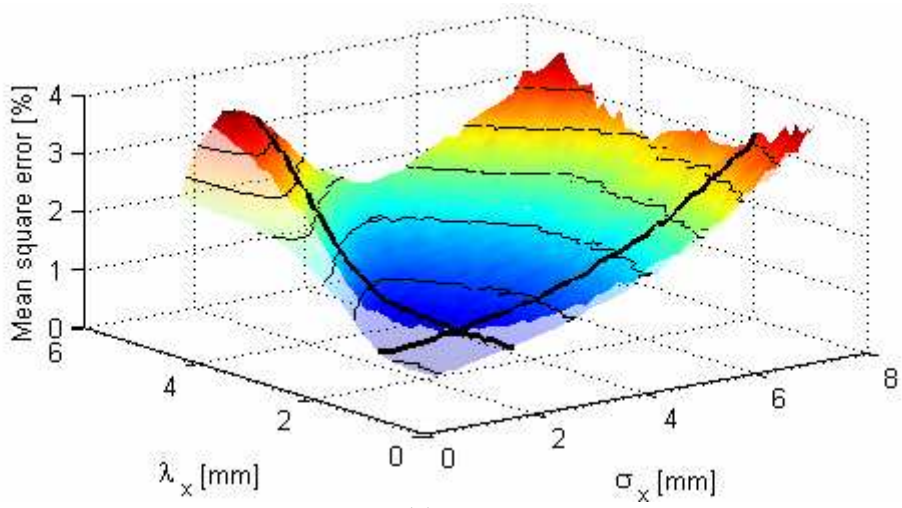

(a)

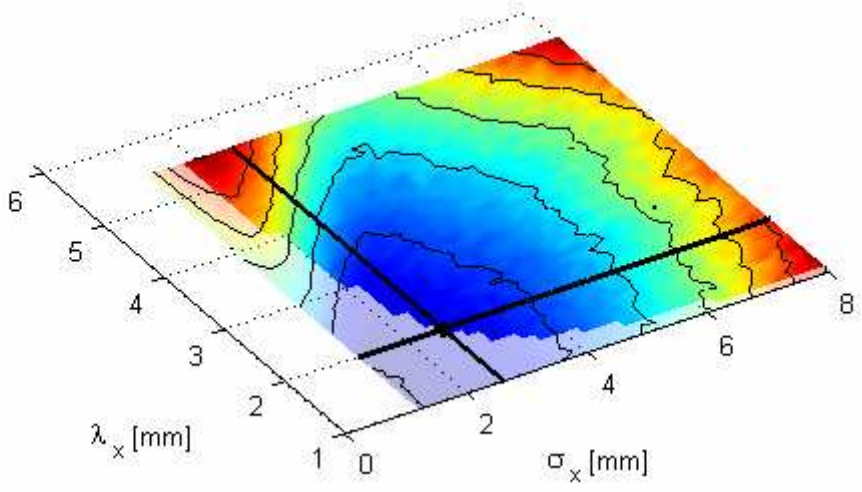

(b)

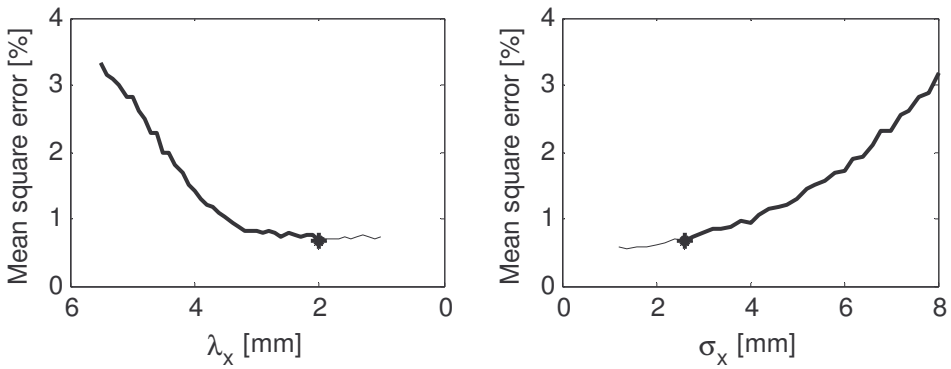

(c) (d)

Figure 3-19: Mean quadratic error calculated for 3000 estimations of the displacement in the case of a strain of 1%. The light part of the surface (a) corresponds to the whole simulation, and the dark one to the limitation given by the physical dimension of our probe, for a depth of 25 mm. The black dot indicates the position of the optimum possible with our probe. (b) is a view from the top of (a). The black lines cross each other at the position of the optimum. The profiles corresponding to the two lines are represented in (c) and (d). For the plots, the bold line corresponds to the possible parameters with our probe. The optimum is for σ_x =2.6mm and λ_x =2mm.

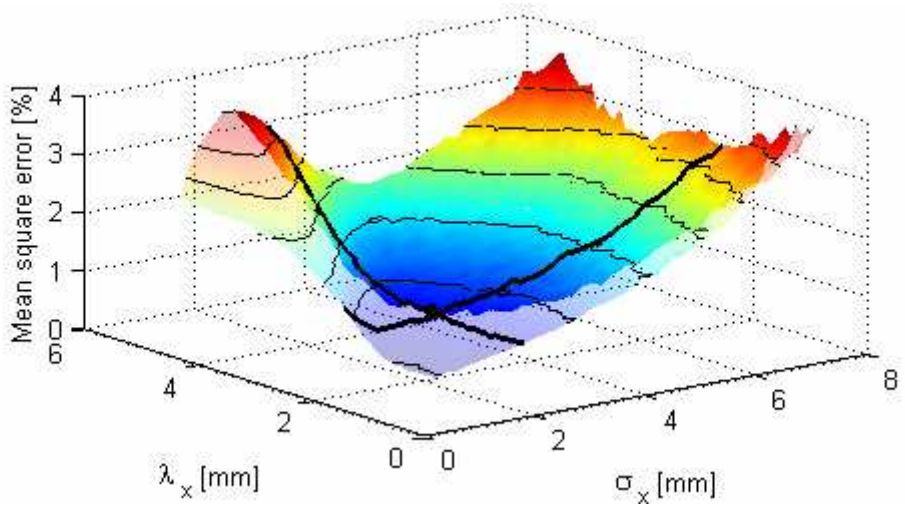

(a)

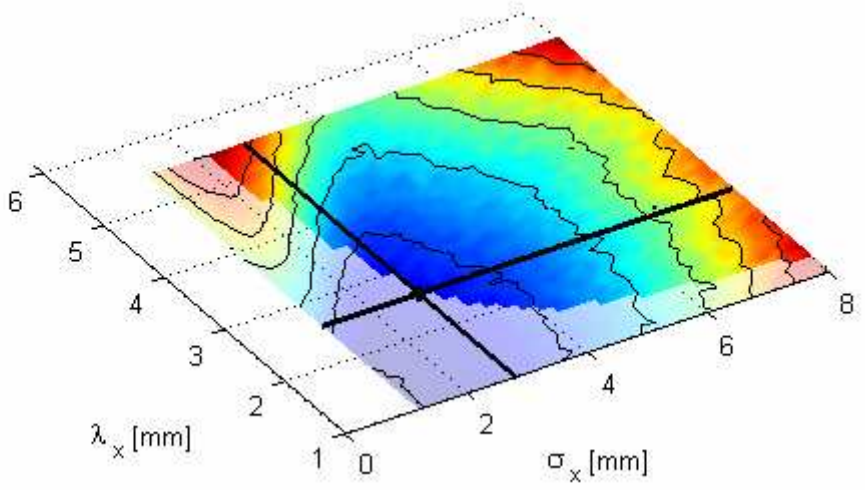

(b)

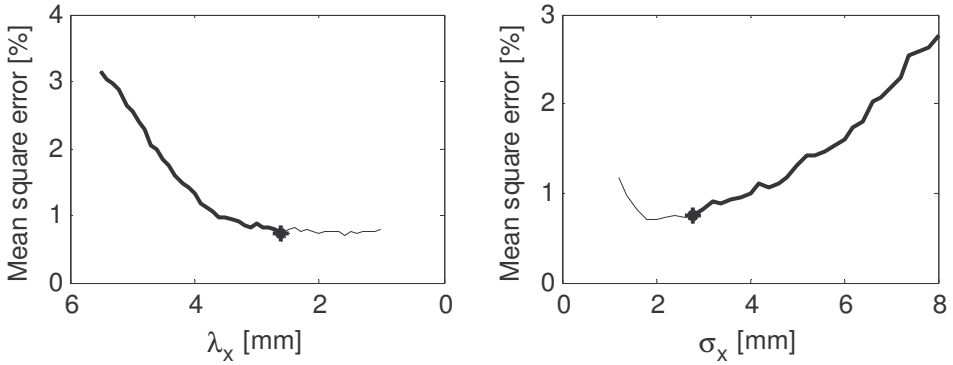

(c) (d)

Figure 3-20: Mean quadratic error calculated for 3000 estimations of the displacement in the case of a strain of 1%. The light part of the surface (a) corresponds to the whole simulation, and the dark one to the limitation given by the physical dimension of our probe, for a depth of 30 mm. The black dot indicates the position of the optimum possible with our probe. (b) is a view from the top of (a). As the depth is not the same as for Figure 3-19, the position of the dot is not the same. The black lines cross each other at the position of the optimum. The profiles corresponding to the two lines are represented in (c) and (d). For the plots, the bold line corresponds to the possible parameters with our probe. The optimum is for σ_x =2.8mm and λ_x =2.6mm.

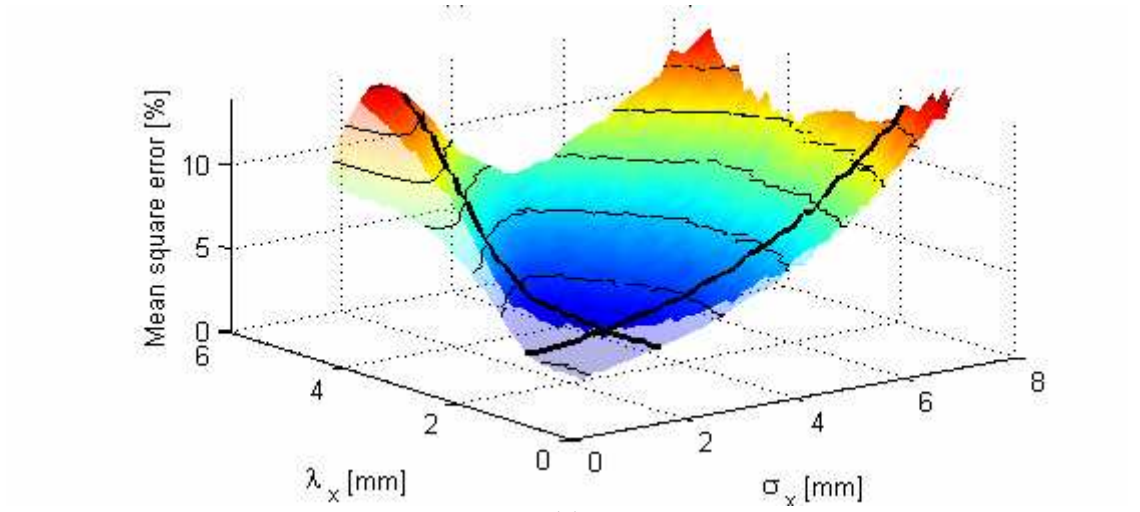

(a)

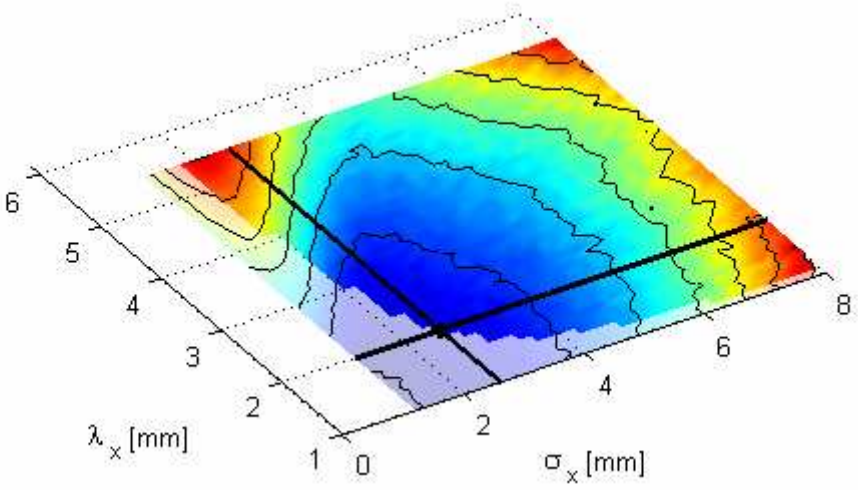

(b)

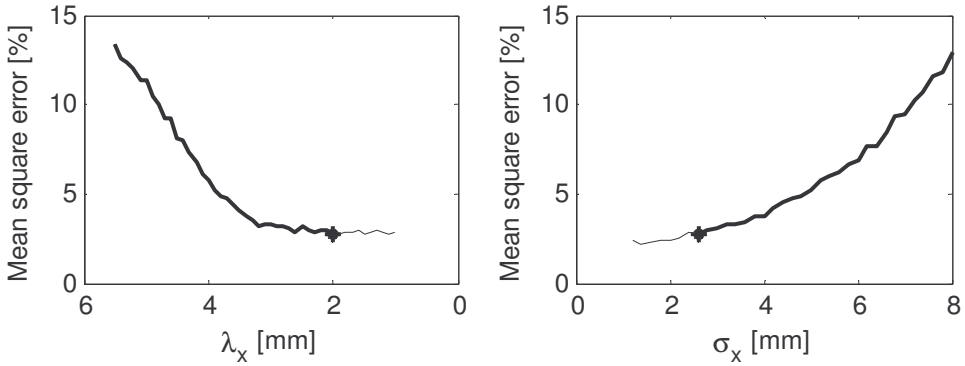

(c) (d)

Figure 3-21: Mean quadratic error calculated for 3000 estimations of the displacement in the case of a strain of 2%. The light part of the surface (a) corresponds to the whole simulation, and the dark one to the limitation given by the physical dimension of our probe, for a depth of 25 mm. The black dot indicates the position of the optimum possible with our probe. (b) is a view from the top of (a). As the depth is the same as for Figure 3-19, only the applied strain changes and the position of the dot is the same. The black lines cross each other at the position of the optimum. The profiles corresponding to the two lines are represented in (c) and (d). For the plots, the bold line corresponds to the possible parameters with our probe. The optimum is for σ_x =2.6mm and λ_x =2mm.

The results of those simulations are given in Figure 3-19, Figure 3-20 and Figure 3-21, for two strain values and considering two different depths. More parameters than those that can be reached with our probe have been simulated. This enables to see what could be reached if the parameters could be even more optimized. In the figures, the light part of the surface corresponds to what can not be reached with our probe, whereas the dark part corresponds to the parameters that can be chosen. On the plots, (c) and (d), the bold line corresponds to the values that can be used, and the thin line to the forbidden values.

As can be seen in those figures, there is a real compromise between the width at half maximum of the envelope, σ_x, and the wavelength of the oscillations, λ_x, of the lateral profile of the PSF.

The tendency is a reduced mean quadratic error for small standard deviations and small lateral wavelengths.

One probable reason for that is that the standard deviation is related to the resolution. As the PSF has a certain width one specific sample of a signal is not the sum of contributions coming only from its position. The other scatterers situated near its position also participate to its value. Having a small standard deviation increases the locality of the information, whereas wide PSFs will increase the mixing of information coming from different positions, increasing as a consequence the averaging and loss of information. If there was a constant (space unvarying) displacement the results would be different. Indeed, all scatterers would have the same displacement and no problem of locality would be important. However in our case the notion of resolution is important and this is the reason why having a thin PSF (small σ_x) is important.

More over it is interesting to choose a solution that needs a thin PSF, because this needs a large apodization function, and it involves more elements of the probe. The more raw signals are combined, the more the signal-to-noise ratio is increased. If a boxcar window is used, a multiplication by a factor of N of the number of elements will increase the signal-to-noise ratio of the final signal by a factor of $\sqrt{N}$ as explained in [63].

Having a small λ_x is important because it corresponds to a steep phase of the complex correlation.

The simulation has been done for two strain values, 1% and 2% and two maximal depths of investigation 25 mm and 30 mm. The optimal standard deviation and lateral wavelength values are all recalled in Table 2.

Concerning the strain values, the optimal parameters are the same for both cases. Indeed the coordinates of the optimal point is the same in Figure 3-19 and Figure 3-21.

Also it is interesting to notice the difference between Figure 3-19 and Figure 3-20. The difference between the two figures is the maximal depth of investigation. In Figure 3-19 it is 25 mm and in Figure 3-20 it is 30 mm. If the maximum depth of investigation is higher the same parameters can not be reached. The distance between the peaks has to be larger and the width of the peaks as well. As the physical size of the probe can not be changed, this is not possible.

The optimized parameters for 30 mm lead to a worse accuracy than for 25 mm. Consequently, the parameters will always be chosen according to the highest depth, because it is this depth that gives the most limitation regarding the probe's size. If the parameters are optimized for a smaller depth, the same PSF can not be obtained for the deepest depth of investigation. As one of the basic assumptions

is that the PSF remains constant for the whole depth, this solution can not be chosen. As a result the deepest depth is considered when optimizing the imaging parameters.

It is also important to keep in mind the fact that the design of the beamformer consists of certain assumptions especially that the emission has no consequences on the PSF. This is not the case in the really near field. The point spread functions with parameters optimized for a maximal depth of investigation of 30 mm have been calculated by field simulation. According to Figure 3-20 the parameters of the PSF are: a lateral wavelength $\lambda_x = 2.6$ mm and a standard deviation of the Gaussian envelope $\sigma_x = 2.8$ mm. The point spread functions calculated with the Field II program are given in Annex B.

It is obvious that for small distances close to the probe, the PSF is not exactly equal to the expected one. However for higher depths this assumption can be made, the correlation coefficient between the expected profile and the obtained one is higher than 95%.

In simulation a slice of the medium situated between 20 and 30 mm will be considered.

The parameters for the beamformer are simply calculated using back-propagation of the given PSF.

Now that the parameters of imaging have been chosen the parameters of the medium investigated in simulation are going to be given.

Depth	Strain	σ_x	λ_x
25 mm	1%	2.6 mm	2 mm
25 mm	2%	2.6 mm	2 mm
30 mm	1%	2.8 mm	2.6 mm

Table 2: Optimized PSF parameters for different depths and strain values. For a given depth, the optimal parameters are not dependant on the strain value. For a higher depth, the limitation of the probe leads to worse lateral frequency and standard deviation.

Parameters of the medium

In order to make an elastrographic study, the first step consists of the acquisition of the reference and strain images. When the study is done in simulation, before calculating the images, it is necessary to make a mechanical simulation of the medium under investigation.

This is done with Femlab[4], a finite element simulation tool, which has the advantage of being completely compatible with Matlab[5], which is the tool that is used for all calculations.

With Femlab a 2D simulation of a slice of the medium is done. The plane strain case is considered, assuming that the azimuthal dimension is large enough to be ignored. The medium has to show a difference in stiffness. A medium containing an inclusion having a Gaussian Young's modulus distribution is simulated. The Young's modulus of the whole medium in kPa is given in (3-54), and can be seen in Figure 3-22:

$$E = 50 + 450e^{-\pi\left(\frac{x}{4}\right)^2} e^{-\pi\left(\frac{(y-25)}{4}\right)^2} \tag{3-54}$$

[4] Femlab 3.1. Copyright © 1994-2004 COMSOL AB
[5] Matlab 7.0. Copyright © 1994-2004 The Mathworks, Inc.

In equation (3-54) the first term corresponds to the modulus of the background medium of the phantom, here it is equal to 50 kPa. The second term corresponds to a Gaussian inclusion. As a consequence, the maximum of the Young's modulus distribution is equal to 500 kPa, which means that there is a factor of 10 between the maximum and minimum value of Young's modulus.

The Poisson's ratio, which is also an important parameter of the medium is chosen equal to 0.49, which is a characteristic value for biological tissues, which are mainly composed of water and are nearly incompressible.

The boundary conditions for the simulation are a still position of the top of the phantom, and the compression applied on the bottom. The compression consists of a displacement of 0.1 mm of the deepest edge of the phantom. This would correspond, for a homogeneous medium, to a homogeneous axial strain of 3.3%.

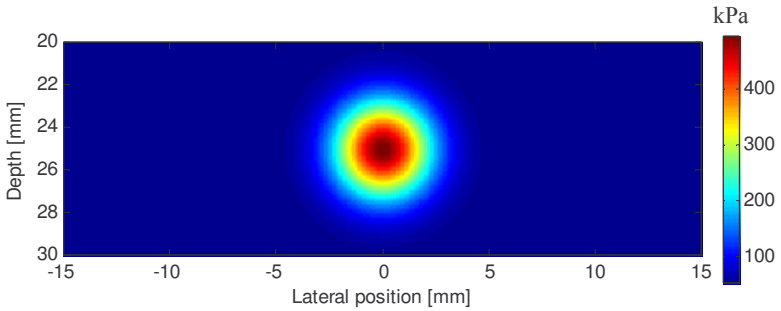

Figure 3-22: Distribution of the Young's modulus in the medium. The modulus inside the hard inclusion is Gaussian with a maximum of 500 kPa, and the background's modulus is 50 kPa, as given in (3-54).

The Femlab program generates a mesh and calculates the displacement for each node of the mesh according to the physical characteristics and the boundary conditions previously specified. The coordinates of the nodes before and after applying the stress are used for calculating the images. Each node is used as a scatterer.

If there are too few scatterers some additional ones are added randomly between the nodes of the mesh. The displacement of those additional scatterers is taken as a linear combination of the neighboring scatterers. Enough scatterers are added to have an average of one scatterer per square of side equal to the wavelength of the emitted wave. For the medium of 30 mm by 10 mm this yielded 10.000 scatterers.

Then the images are calculated using all the reference and displaced distributions of scatterers according to the 2D versions of (2-6) and (2-10) which are expressed as

$$r(x,y) = h(x,y) \underset{x,y}{\otimes} d(x,y) \tag{3-55}$$

$$s(x,y) = h(x,y) \underset{x,y}{\otimes} d'(x,y) \tag{3-56}$$

The amplitude of the scattering coefficients of $d(x,y)$ is chosen in order to be a random normal distribution.

Two sets of images are calculated using the analytical expressions of the PSF given by the following equations.

$$h(x,y) = e^{-\pi\left(\frac{x}{\sigma_x}\right)^2} e^{-\pi\left(\frac{y}{\sigma_y}\right)^2} \cos(2\pi u_x x)\cos(2\pi u_y y) \tag{3-57}$$

with, $\lambda_x = 2.6$ mm, $\sigma_x = 2.8$ mm, $\lambda_y = 1/u_y = 0.2$ mm, $\sigma_y = 0.8$ mm is the expression of the PSF with lateral oscillations. Those parameters have been determined previously as optimal for the lateral oscillations according to our probe for a depth of 30 mm (Figure 3-20).

$$h(x,y) = e^{-\pi\left(\frac{x}{\sigma_x}\right)^2} e^{-\pi\left(\frac{y}{\sigma_y}\right)^2} \cos(2\pi u_y y) \tag{3-58}$$

with, $\sigma_x = 1.4$ mm, $\lambda_y = 1/u_y = 0.2$ mm, $\sigma_y = 0.8$ mm is the expression of the conventional PSF. λ_y corresponds to the wavelength of an acoustic wave of frequency 7Mhz (the central frequency of our probe) propagating in water with constant sound speed equal to 1540m/s.

Once the images are calculated, the last parameters that must be chosen are those concerning the 2D estimation and particularly the axial and lateral windows sizes.

Parameters for the estimation algorithm

The size of both axial and lateral windows used in the algorithm is important. In order to choose the optimal window sizes for our configuration, different window sizes are tested in order to find the optimum sizes that minimize the mean square error of the estimation. These window sizes will then be used for the simulation and experimental results.

Figure 3-23 shows the mean quadratic error of the axial estimate normalized by the true quadratic displacement as a function of the window size. This is expressed in percents. The quadratic error has been averaged only for the points for which the algorithm finds a solution. Indeed, if the result is averaged over all points the plot doesn't show an optimum. More over, when the displacement map is shown as an image, some kind of salt and pepper noise appears.

Figure 3-24 shows the axial estimated displacement and the same map with the points not taken into account in brown. The accidents of estimation or failure appear as some kind of salt and pepper noise.

This led us to introduce a threshold for which the estimation was considered to work. The threshold was set to 0.1 mm, which is roughly half the axial wavelength. This means that the points, for which the difference between the estimate and the true displacement was more than 0.1 mm, have not been considered when calculating the average of the quadratic error. Figure 3-25 shows the percentage of failure for the axial estimation.

The interpretation of this results as well as the choice of the axial window has to take into account information of both plots. The conclusion is actually quite simple. When the estimation works it's better to have larger windows. However larger windows increase the number of false estimations. As a consequence the size of the window is taken equal to 100 samples. This value correspond to 1.54 mm and approximately 7 λ_y.

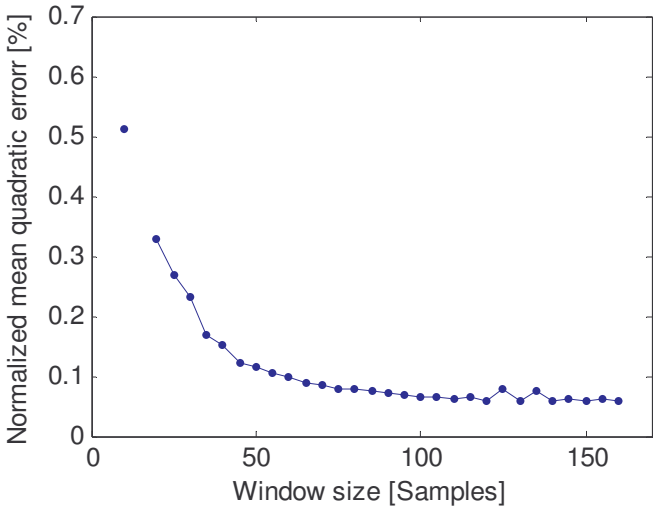

Figure 3-23: Normalized mean quadratic error of the axial estimate with respect to the axial window size. There is no real minimum, the curve is always decreasing. However it gets more flat around 130 samples, which corresponds to 2 mm, or 9 times the axial wavelength

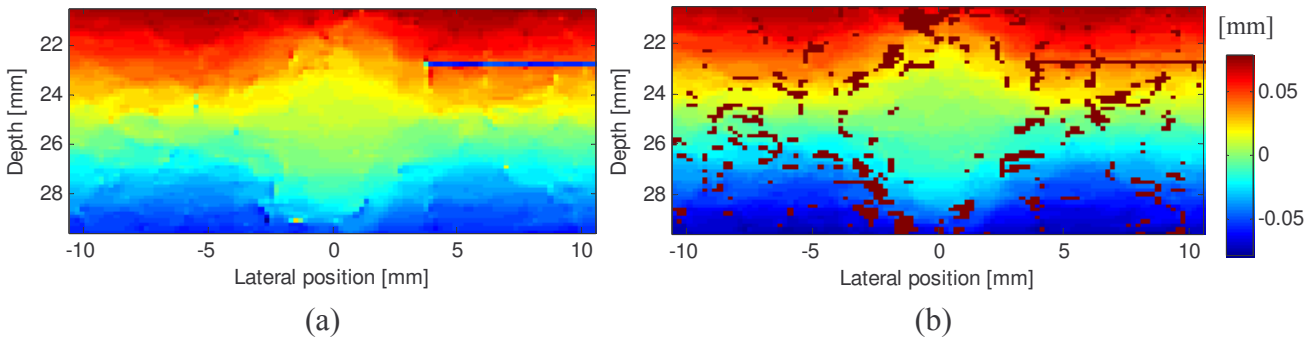

Figure 3-24: (a) Image of the estimated axial displacement, (b) same image with all points not taken into account for calculating the mean quadratic error in the same brown color. For those points the error is more important than the threshold value.

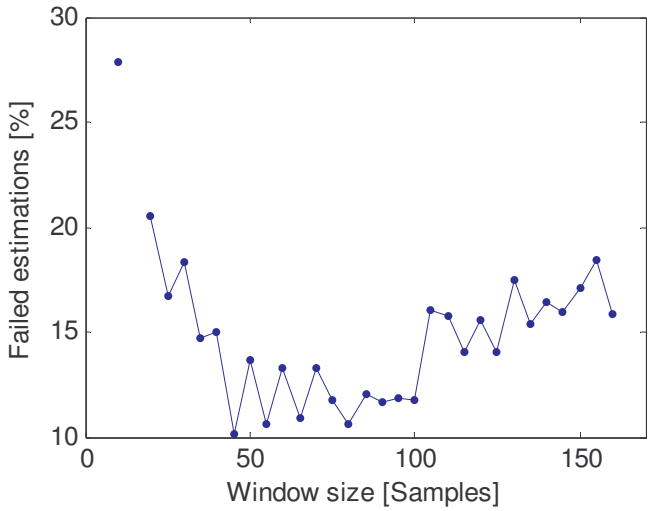

Figure 3-25: Proportion of estimation that fails for the axial estimation. Even if Figure 3-23 shows that the quality of the estimate is increasing with the size of the window, this figure shows that the number of failure also increases with the window size.

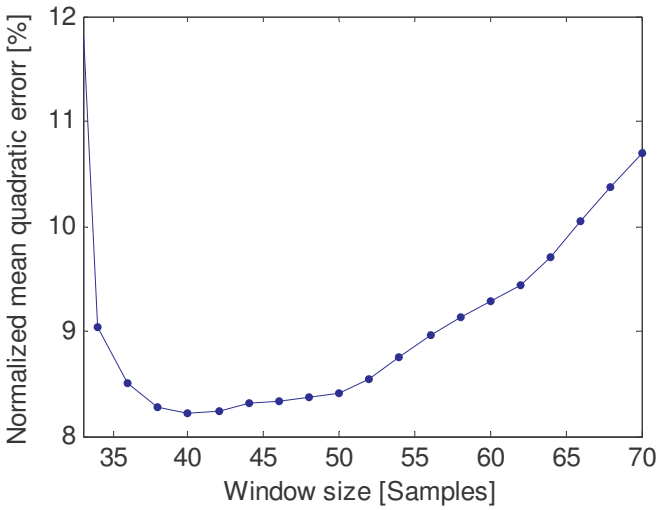

Figure 3-26: Mean quadratic error of the lateral estimate with respect to the lateral window size. The minimum is around 43 samples, which corresponds to 4.3 mm, or 3 times the lateral wavelength

Figure 3-26 shows the mean quadratic error for the lateral estimation with respect to the size of the lateral windows. In this case there was no need to add a second plot showing the number of failure, because the algorithm always finds a solution. What must be understood here is that there is no salt and paper noise in the estimation. The quality of the estimation is the same for all points. The lateral estimation is not better than the axial one. The scale of the plots shows that the mean quadratic error is much larger than for the axial estimate. In the lateral direction it is several percents whereas in the axial direction it is several tens of percents.

Here the optimum is between 40 and 45 samples. The windows size is taken equal to 43 samples. This corresponds to 4.3 mm or approximately $1.5\lambda_x$.

The comparison between axial and lateral estimation shows how much the difference in accuracy and resolution is important. The lateral optimal window is more than three times larger than the axial window.

Now that the parameters for which the result should be optimum have been determined, the simulation results can be shown.

3.7 Simulation results

Two simulation results will be shown. The first result shows the comparison between the displacement estimated from conventional images and the displacement estimated from lateral oscillations images. Here the limitation of the probe is respected. The second results show the estimated displacement obtained if the same axial and lateral characteristics could be achieved for our PSF.

3.7.1. With all optimal parameters according to the probe

Figure 3-27 shows a B-mode image of the medium obtained with the system approach (3-55). The speckle patterns can be recognized.

Figure 3-28 gives an arrow representation of the total true displacement. Figure 3-29 and Figure 3-30 give an arrow representation of the total estimated displacement obtained with conventional images and lateral oscillations images, respectively.

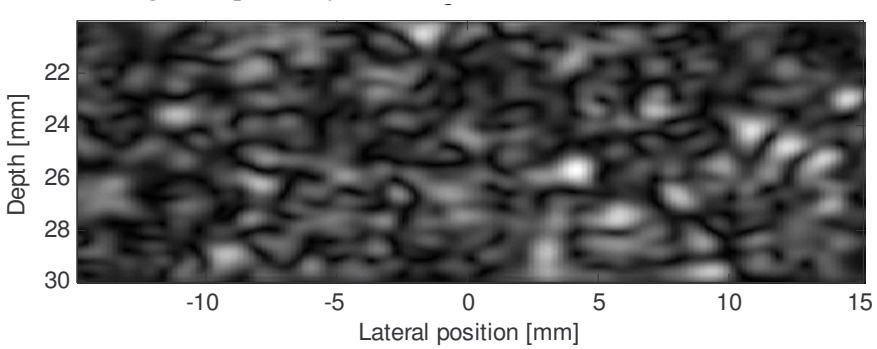

Figure 3-27: B-mode image of the medium

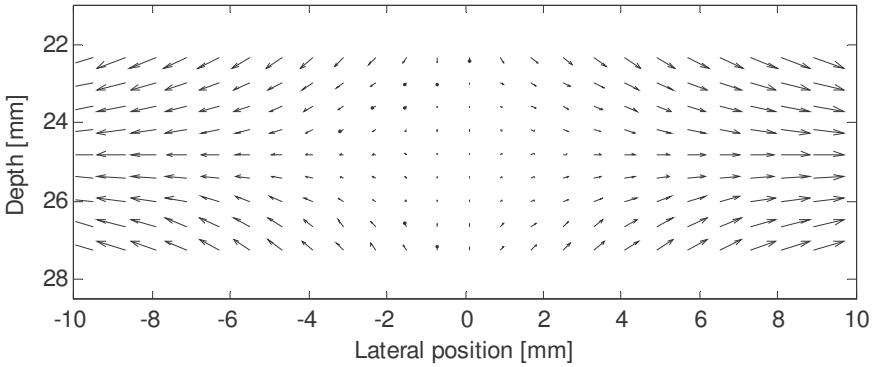

Figure 3-28: Arrow representation of the true displacement

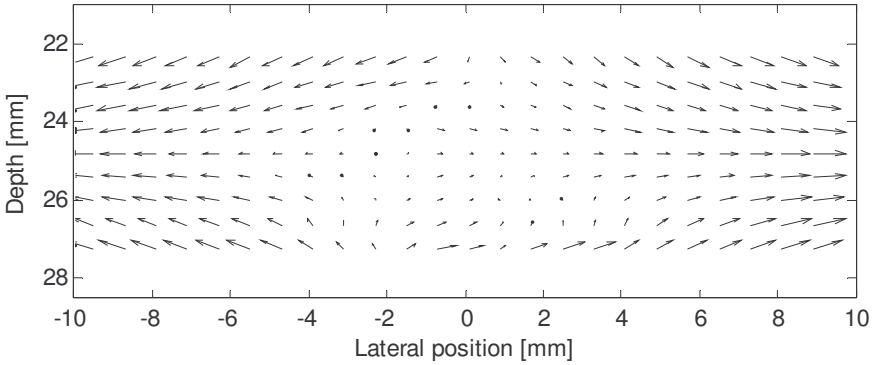

Figure 3-29: Arrow representation of the estimated displacement with conventional images

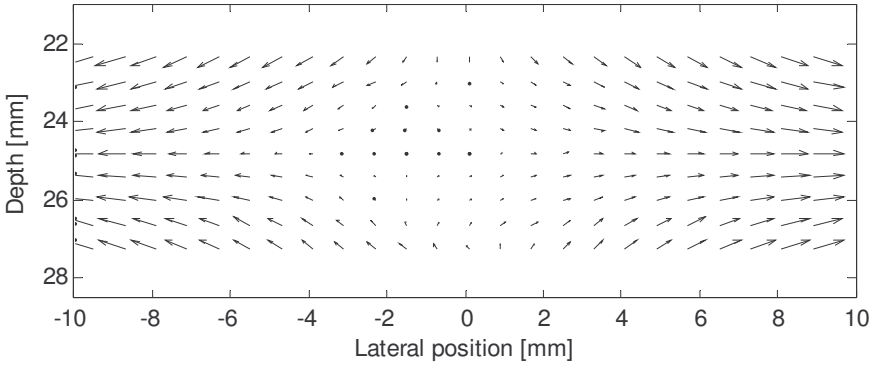

Figure 3-30: Arrow representation of the estimated displacement with the lateral oscillations images

Figure 3-31 shows a comparison between the true and estimated axial displacements for conventional and lateral oscillations images. The estimate is in good agreement with the expected values for both kinds of images. This is expected because the lateral oscillations images are used only for the lateral displacement estimation and the same images are used for axial displacement estimation.

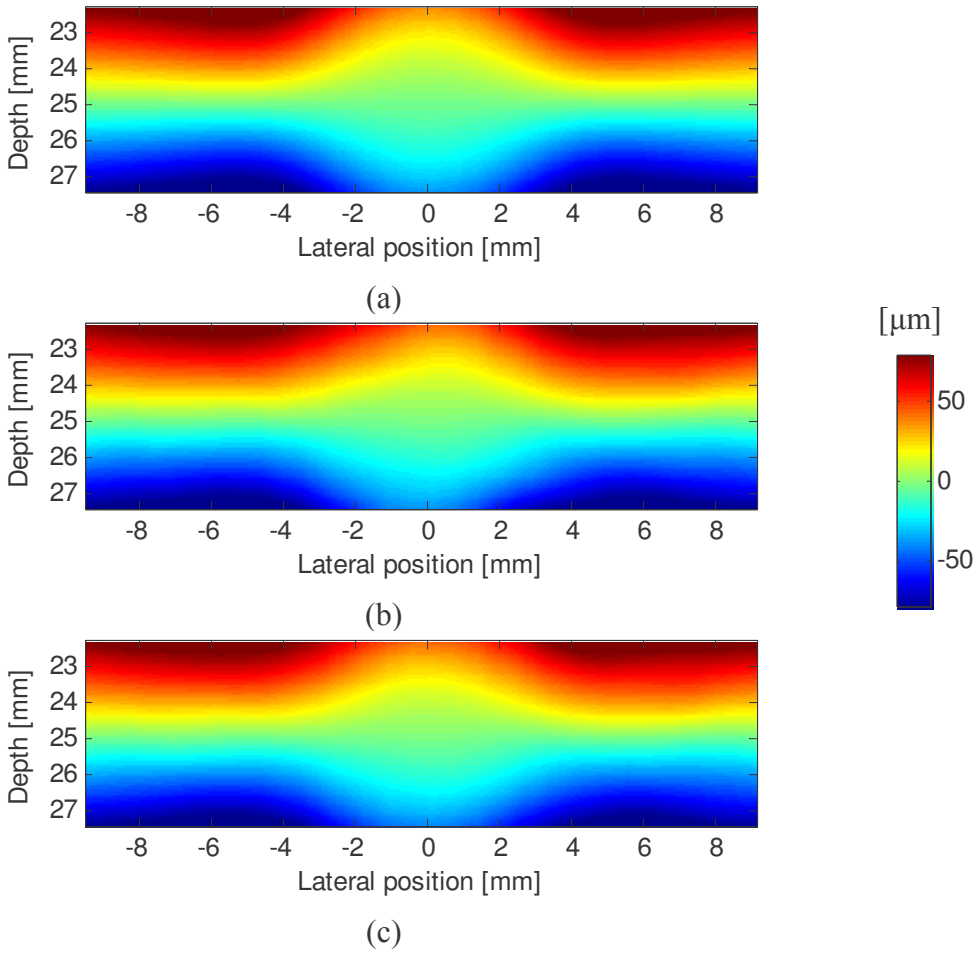

Figure 3-31: (a) True *axial* displacement and (b) estimated *axial* displacement obtained with conventional images and (c) with lateral oscillations.

Figure 3-32 shows a comparison between the true and estimated lateral displacement. The estimate obtained with lateral oscillations images is closer to the expected values than the one obtained with conventional images.

An important difference in accuracy between the axial and the lateral directions exists for both methods. But what is really important to notice here is that the accuracy of the estimation is really improved thanks to the lateral oscillations. Let's now have a look on the error maps.

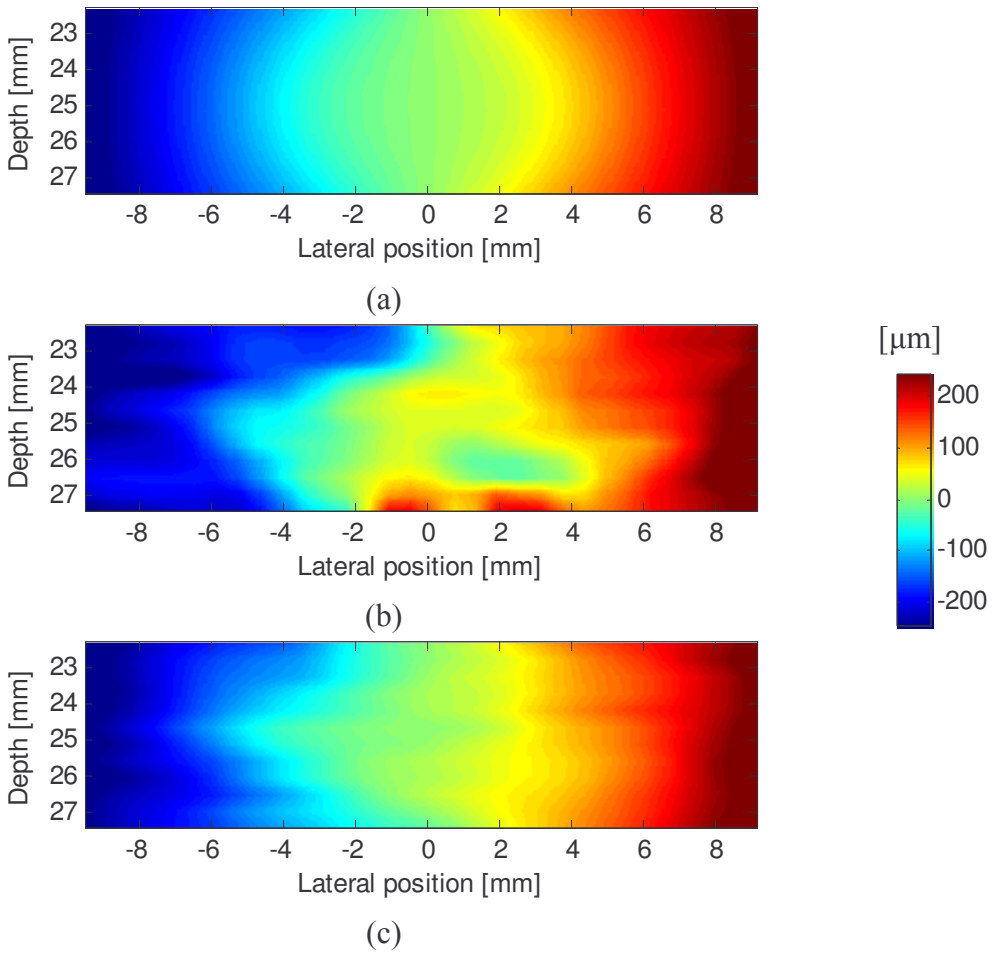

Figure 3-32: (a) True *lateral* displacement and (b) estimated *lateral* displacement obtained with conventional images and (c) with lateral oscillations.

It is important to recall here that for the axial estimation the same images are used. Only the images used for the lateral displacement estimation are different. Figure 3-33 shows the error maps for the axial estimation. As said earlier the two maps are in the same order of magnitude. This indicates that estimating the lateral displacement with other images does not really have an impact on the accuracy of the axial displacement estimation.

However in Figure 3-34 the difference between the error maps for the lateral displacement estimation lets no doubt about the improvement due to the lateral oscillations. The error is much larger without lateral oscillations. Next, the histogram of this error will be considered.

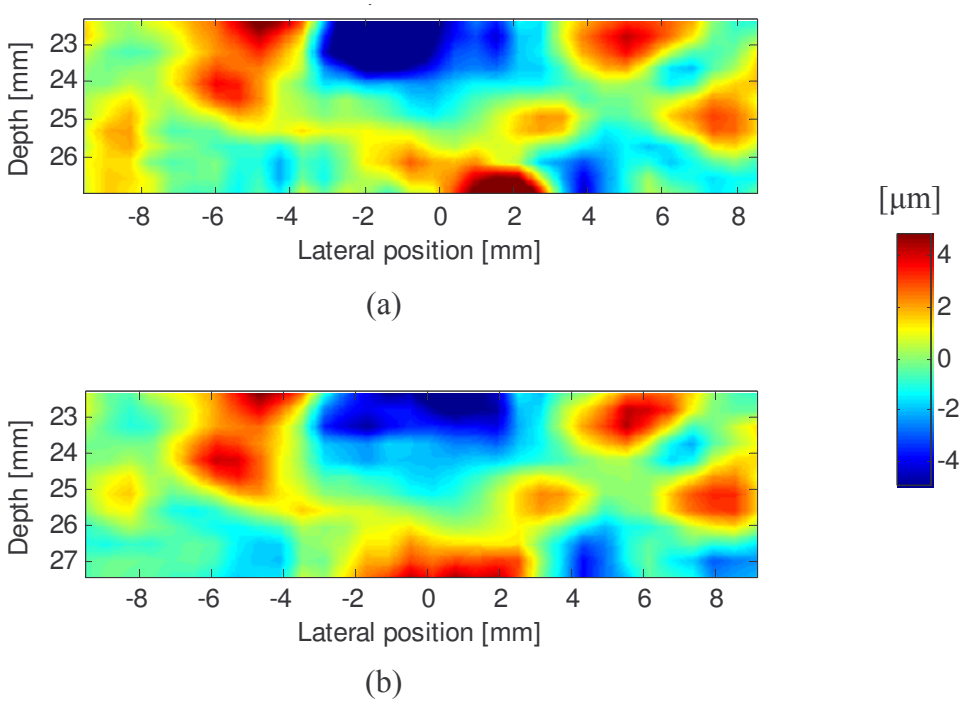

Figure 3-33: Error maps of the axial estimation for conventional images (a) and with the lateral oscillations images (b).

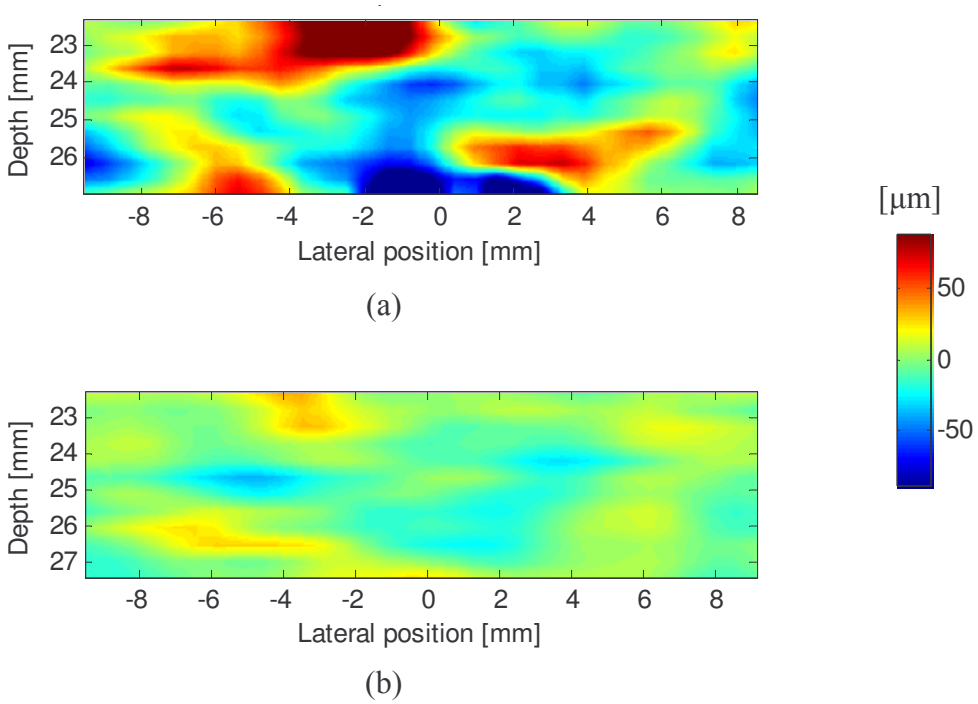

Figure 3-34: Error maps of the lateral estimation for conventional images (a) and with the lateral oscillations images (b).

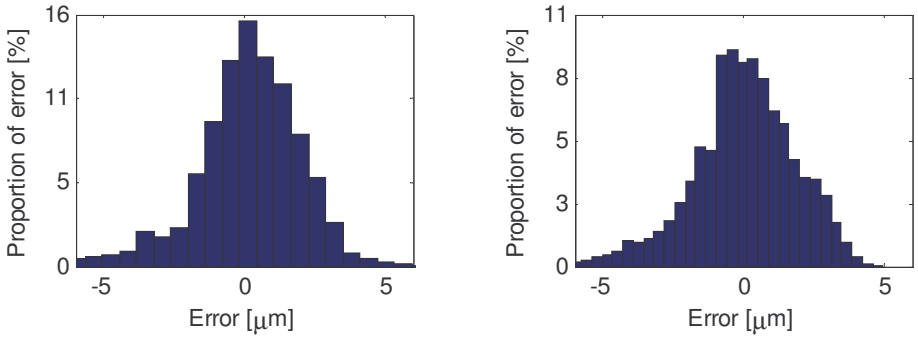

Figure 3-35: Histograms of the error of the axial estimation for the conventional (a) and lateral oscillations images (b)

Figure 3-35 shows the histograms of the axial error for the conventional and lateral oscillations images. The two distributions are really close to each other. The standard deviation of the error for the conventional images is equal to 2.2μm and to 1.8μm for the lateral oscillations. It is a little bit smaller for the lateral oscillations images which could lead us to think that using images that are beamformed differently from conventional images for the lateral estimation also improves the quality of the axial estimation.

But the improvement is more important for the lateral estimation.

Figure 3-36 shows the histograms of the lateral estimation error. Here the difference is really important. The standard deviation of the lateral error is 37.1μm for the conventional images and 11.4μm for the lateral oscillations. This is an improvement of more than a factor 3. There is still an important difference between the qualities of the estimation in both directions.

It is also possible to take a look at the histograms of the difference between the estimated displacements in both cases. Figure 3-37 shows the histogram of the difference between the two axial displacement maps obtained with the lateral oscillations and with the conventional images (Figure 3-31(b) - Figure 3-31(c)). It shows also the histogram of the difference between the two lateral displacement maps obtained with the lateral oscillations and with the conventional images (Figure 3-32(b) - Figure 3-32(c)). As already expected, the axial estimates don't change as much as the lateral ones. The distribution for the lateral estimate is spread over larger values. The standard deviation of the axial difference is 1 μm and for the lateral direction it is 35.3 μm. This distribution is finally really close to the distribution of the error obtained with conventional images. The displacement map obtained with lateral oscillation has an error that can be neglected compared to the one obtained with conventional images.

Even if this case cannot be reached with the actual material, mainly because of the limited size of the probe, it is interesting to take a look at what would be the estimation if the characteristics of the PSF were the same in the axial and lateral directions.

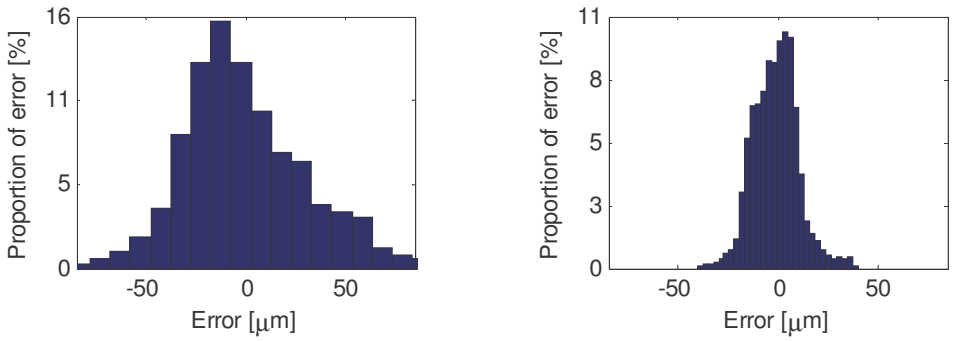

Figure 3-36: Histograms of the error for the lateral displacement estimation (a) for the conventional images and (b) for the lateral oscillations images.

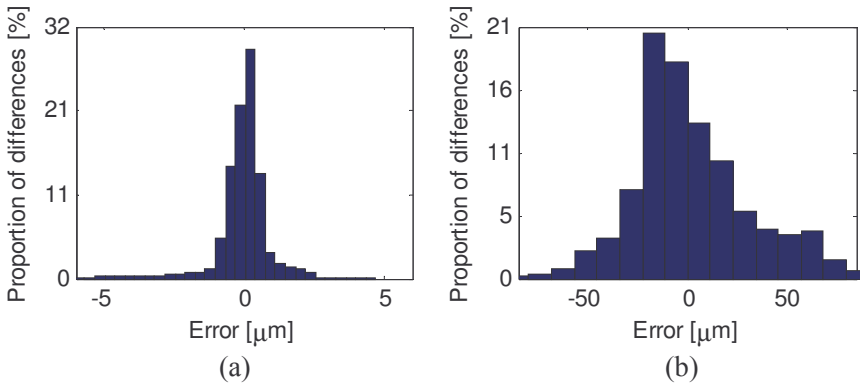

Figure 3-37: (a) Histogram of the difference between the axial displacement estimated with the lateral oscillations images and the axial displacement estimated with the conventional images. (b) Histogram of the difference between the lateral displacement estimated with the lateral oscillations, and the lateral displacement estimated with the conventional images.

3.7.2. If the lateral properties of the PSF could be made identical to the axial properties.

In this section the same approach as previously has been used, *i.e.* the system approach for the generation of the images, and the same set of scatterers.

The difference here is that for the lateral oscillations images, a 90° rotated version of the PSF used for the axial images has been used. The two PSFs can be expressed as

$$h(x,y) = e^{-\pi\left(\frac{x}{\sigma_x}\right)^2} e^{-\pi\left(\frac{y}{\sigma_y}\right)^2} \cos(2\pi u_y y) \tag{3-59}$$

$$h(x,y) = e^{-\pi\left(\frac{x}{\sigma_x}\right)^2} e^{-\pi\left(\frac{y}{\sigma_y}\right)^2} \cos(2\pi u_x x) \tag{3-60}$$

with, $\lambda_y = 1/u_y = \lambda_x = 1/u_x = 0.2$ mm, $\sigma_y = \sigma_x = 0.73$ mm. (3-59) and (3-60) are the conventional and lateral oscillations PSFs used for this simulation, respectively.

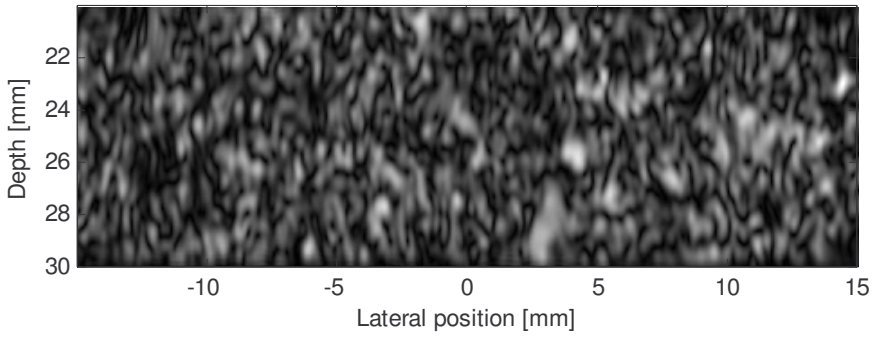

Figure 3-38: B-mode image of the medium.

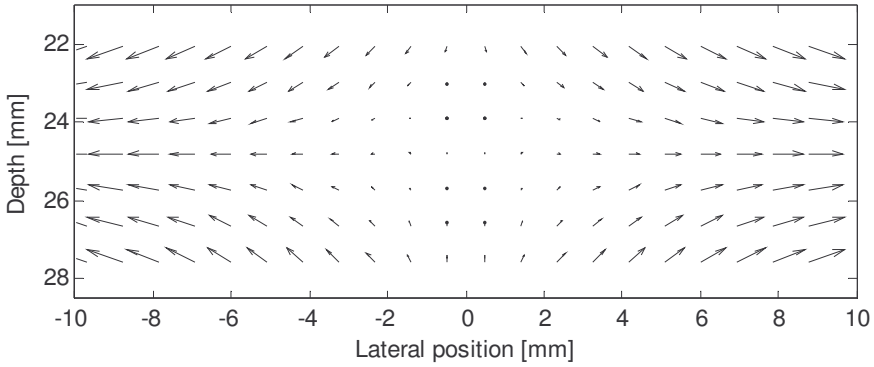

Figure 3-39: Arrow representation of the true displacement

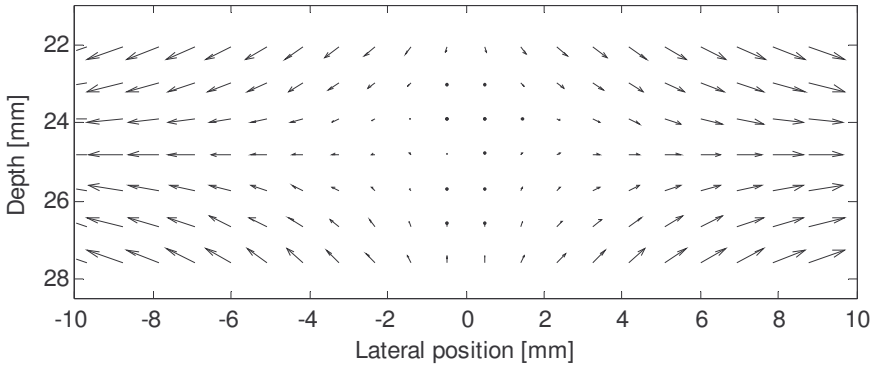

Figure 3-40: Arrow representation of the estimated displacement

Figure 3-38 shows a B-mode image of the medium. The speckle pattern shows more variations in the lateral direction in this case because the lateral oscillations are much faster than previously.

Figure 3-39 and Figure 3-40 show arrow representations of true and estimated displacements, respectively.

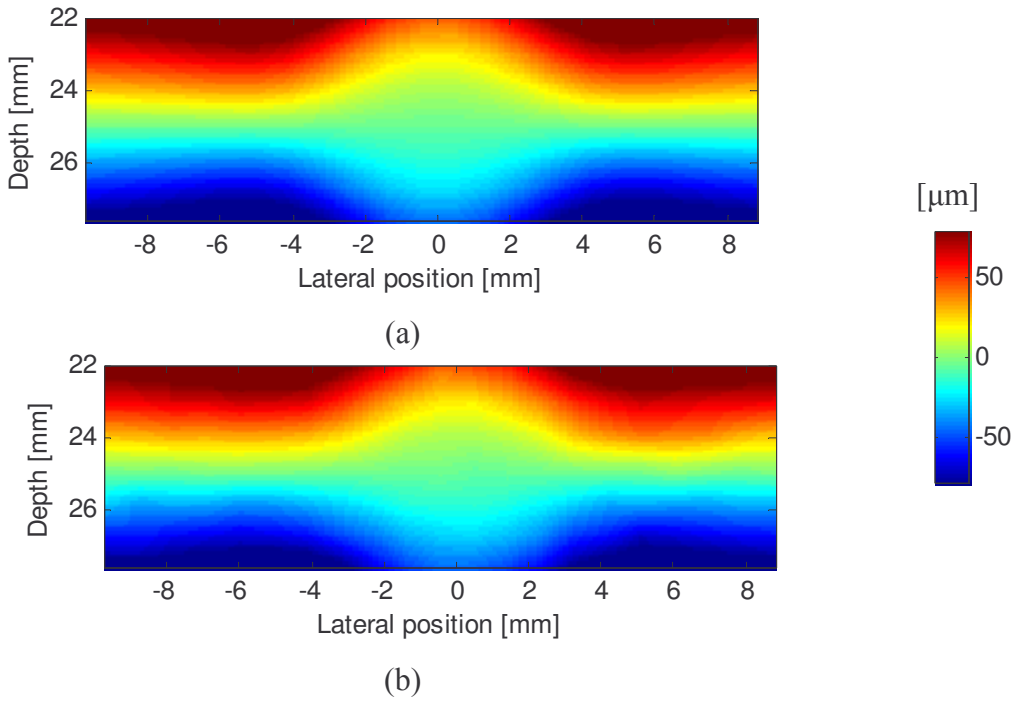

(a)

(b)

Figure 3-41: (a) True and (b) estimated axial displacement in µm

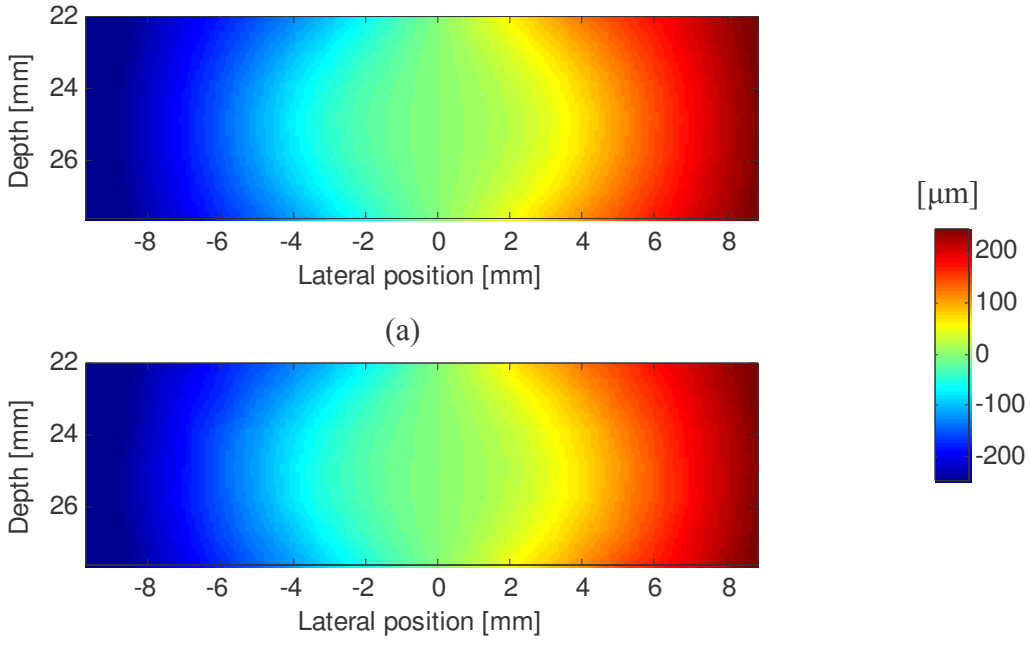

(a)

(b)

Figure 3-42: (a) True and (b) estimated lateral displacement in µm.

Figure 3-41 and Figure 3-42 show a comparison between the true and estimated axial and lateral displacement. Now that the same characteristics have been used for both the conventional and the lateral oscillations images the same accuracy is reached in both directions.

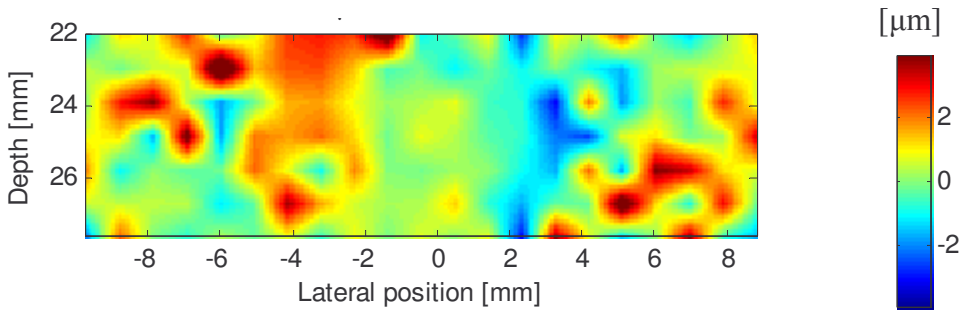

Figure 3-43: Error map of the lateral estimation in µm

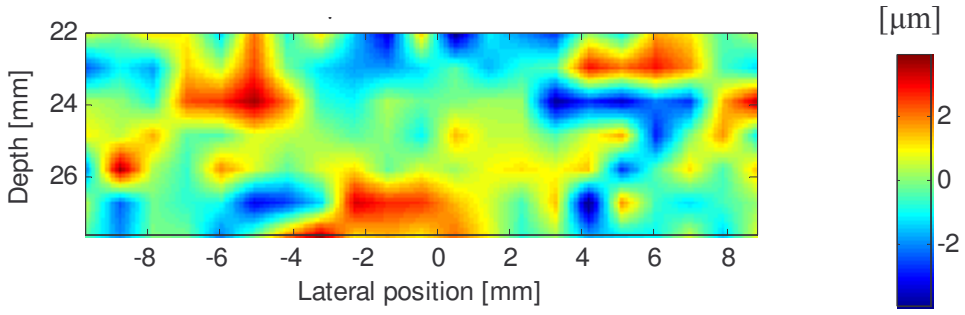

Figure 3-44: Error map of the axial estimation in µm

Indeed Figure 3-43 and Figure 3-44 show the error maps of the lateral and axial estimation. The values seem to be in the same order of magnitude. This is confirmed from the histograms.

Figure 3-45 shows the axial and lateral error histograms. As expected the two error maps are between the same values. The standard deviations of the error are 1.2µm and 1.1µm for the axial and lateral error respectively. This shows that in this case the lateral estimation is of the same quality as the axial estimation.

The mean errors and standard deviations are regrouped in Table 3. The important parameter is the standard deviation which is much larger than the mean error.

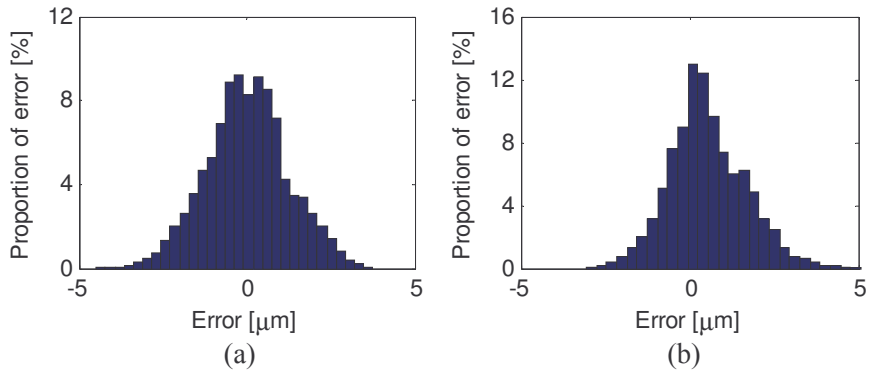

Figure 3-45: Histograms of the error for axial, and lateral displacement estimation (a) and (b) respectively.

This result shows the potential of the method if the same characteristics of the PSF could be achieved in both directions. However, our probe cannot reach this kind of performances.

Let's consider that the frequency of the lateral oscillations can be multiplied by a factor of two due to the heterodyning demodulation. In order to have a final PSF of lateral wavelength 0.2 mm, a beamformer has to be designed that is able to produce a PSF with lateral oscillations of 0.4 mm. If the expected PSF is designed to have three oscillations and the same wavelength as the axial one, this means that the two parameters of the PSF are $\lambda_x = 0.4$ mm, $\sigma_x = 0.7$ mm. The apodization function can be calculated with the back-propagation method for a depth between 15 and 30 mm. The resulting apodization function with the same elements as the 8804 probe is shown in Figure 3-46.

More than 600 active elements should be used for the maximum depth of investigation. As the 8804 inter-elements spacing is equal to 0.208 mm, this would lead to a probe length of 12.4 cm. Neither the number of elements nor the size of the probe is enormous but they are still larger than what is available on the market. In addition, not much tissue can be scanned with such a large probe.

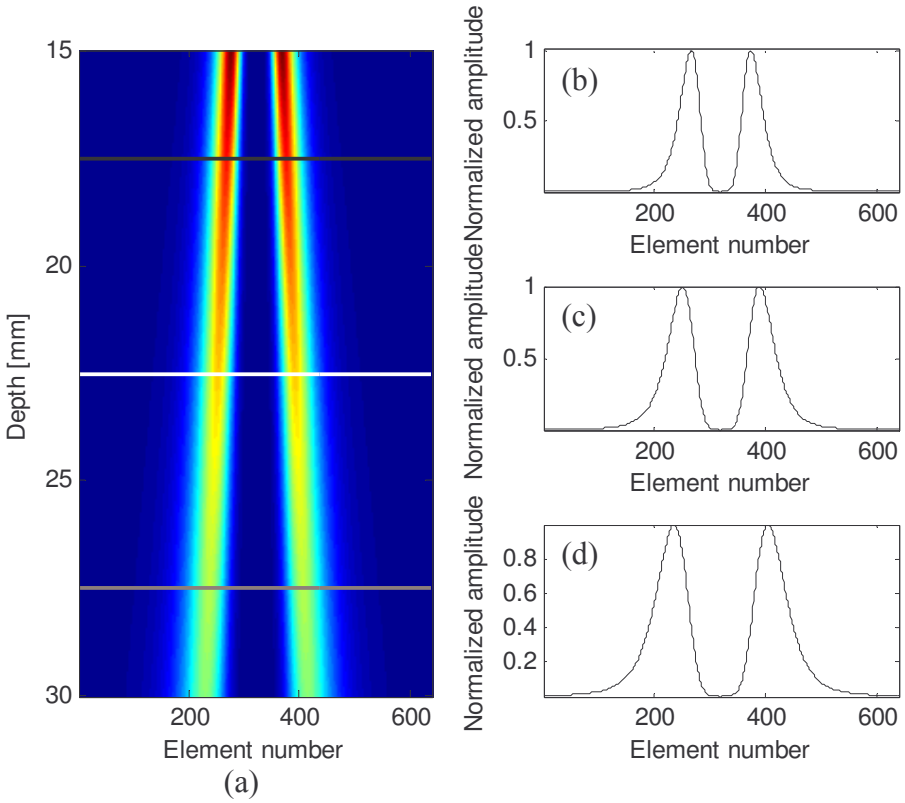

Figure 3-46: Dynamic apodization function with respect to depth between 15 and 30 mm if same axial and lateral PSF would be reached after heterodyning demodulation of the lateral oscillations PSF (a).The profiles at depths of 17.5, 22.5 and 27.5 mm, are given in (b), (c) and (d), respectively.

	Axial direction		Lateral Direction	
	Mean Error	**Standard deviation of the Error**	**Mean Error**	**Standard deviation of the Error**
Conventional images	0.028 µm	2.2 µm	0.603 µm	37.1 µm
Lateral oscillations images with our probe (64 active elements)	0.0188 µm	1.8 µm	0.912 µm	11.4 µm
Lateral oscillations with large probe (600 active elements)	0.0169 µm	1.2 µm	0.52 µm	1.1 µm

Table 3: Summary of the mean error and standard deviation of the error for the different cases simulated: the conventional images, the lateral oscillations images possible with our probe, and the lateral oscillations with a larger probe. Clearly an improvement is shown on the standard deviation of the lateral estimation, first by using lateral oscillations, and even more with a large probe. The important parameter is the standard deviation which is much larger than the mean error.

3.8 Conclusion

In this chapter a new method for estimating lateral displacement between ultrasound RF images has been presented. The phase of the complex correlation between signals is considered. The use of this particular data has led to the development of a specific PSF which is controlled by receive Beamforming. This new PSF is more adapted to lateral displacement estimation than a conventional PSF.

The lateral profile of the PSF, which is Gaussian for conventional images, shows lateral oscillations in our case. The resulting slope of the phase of the complex correlation of the lateral profile of the PSF is 3 times higher with lateral oscillations than with conventional PSF. In simulation it has been shown that the estimation's quality is increased by reducing the standard deviation by a factor of 8 or 9 in the presence of noise compared to conventional images.

A twice 1D approach has been used. The displacement is estimated by seeking for the zero crossing of the phase of the complex cross-correlation between signals taken in the reference and strain images. The zero seeking is achieved using an iterative Newton method. The whole estimation algorithm has been described.

The use of a particular PSF has led us to use a specific beamformer. Especially dynamic apodization functions showing two peaks have been used associated with dynamic quadratic focusing.

All parameters of both beamforming and estimation have been optimized by taking into account the limitations imposed by our ultrasound probe, especially the width of the probe that limits both the lateral oscillations frequency and the standard deviation of the lateral envelope of the PSF. It has been shown that the choice of the parameters doesn't depend on the applied strain. However they are limited by the depth of investigation. For a depth of 30 mm the optimal parameters are a lateral wavelength $\lambda_x = 2.6$ mm, a standard deviation of the Gaussian equal to the width at half maximum $\sigma_x = 2.8\,\text{mm}$

Some simulations have been done using those parameters, and the estimation results are given. It is clear that the accuracy of the lateral estimation is still worse than for the axial estimation. But the quality of the lateral estimation has been improved by a factor of 3 compared to conventional images.

Some results obtained with a lateral oscillations PSF showing the same characteristics in the lateral direction as the conventional PSF in the axial direction have been shown. In this case the axial and lateral estimations have the same precision. The physical characteristics of a probe that could produce such a PSF are given. With 600 elements and a length of 12.4 cm, this probe is bigger than what the current market is able to provide.

In the next chapter some experimental results will be presented which have been obtained using this method on a real custom-built ultrasound scanner.

Chapter 4

Experimental results

In this chapter some results of our method, obtained experimentally with phantoms are presented. First the system that has been used is described. Before presenting the estimation results, the PSF obtained experimentally with a wire phantom are shown. Then two different results will be presented. First, one study presents the result of the estimation with only a lateral displacement. Then a result when a phantom with a hard inclusion inside is compressed with the probe is presented.

4.1 Introduction

It is important to be aware of the difficulty to access experimental equipment able to provide the raw signals that are needed for our method. Indeed as a particular beamformer has to be used, it is of no use to acquire classical RF signals already beamformed by the scanner. Unfortunately, this is still what many research groups have access to, from their ultrasound equipment.

In Lyon, we customized a BK Medical 3535 scanner, in order to access all raw data. We have been able to access not the complete raw data, but a combination of them. The 3535 scanner was developed during the 80's. In this scanner, the signals that are supposed to be processed the same way are summed before applying those processing. This is the case for signals coming from elements situated at symmetrical positions on each side of the beam axis. Indeed those signals are delayed the same way during focusing. Combining the signals like this enables to save half the number of delay lines.

We have been able, with our system, to acquire data from a wire phantom and to show point spread functions with lateral oscillations. This work has been presented at the 2004 IEEE Ultrasonics Symposium in Montréal by Delachartre *et.al* in [64]. However, our system had a non-reparable breakdown some months after the conference.

In parallel, this PhD project has been made in collaboration with Dr. Jens E. Wilhjelm from the Technical University of Denmark who is also associated with the Center for Fast Ultrasound Imaging (CFU) directed by Professor Jørgen A. Jensen. The CFU group has developed an ultrasound scanner dedicated to research and advanced studies in beamforming and synthetic aperture (called RASMUS). RASMUS gives the possibility to acquire all raw data from different ultrasound probes [19], [65]. In the frame of our collaboration it was possible to use the RASMUS scanner which will briefly be presented before describing the measurements.

4.2 The RASMUS scanner

The Remotely Accessible Software configurable MUltichannel Sampling system (RASMUS) is presented in detail in a recent paper by Jensen *et.al.* [19]. The main characteristics of the scanner are recalled here.

RASMUS consists of four distinct modules: transmitters, analog receive and transmit amplifiers (RX/TX amplifiers), receivers, and sync/master unit. The probe is connected to RASMUS through a 128 wire coaxial cable trough RX/TX amplifiers. The transmitter sends the signals through the transmit amplifiers. The receiver unit samples the amplified and buffered signals from the receive amplifiers. The sync/master unit holds a crystal oscillator and controls the central timing of the scanning process. The overall operation of the system is controlled trough a number of single board PCs in the individual units, interconnected trough a standard 100 Mbits/s Ethernet. The waveforms and focusing delay data are transmitted from the control PC to the transmitters and receivers boards. The sampled data can be processed by field programmable gate arrays (FPGA), or stored on a PC.

RASMUS can be controlled at different levels. Low level functions enable a direct access to the different modules of the scanner. More high level functions can also be used. The high level functions are based on the same approach as the Field II simulation program. As a result it is very intuitive to use RASMUS if you have been using the Field II program before. Even some function names are identical.

When the group has developed RASMUS, they have been very concerned with making a tool that can be understood and used within a short time by a novice. That's also a reason why everything has been made controllable by a PC using Matlab commands.

More details on the electronic specifications of RASMUS can be found in [19]. The rest of the measurement setup and the acquisitions that have been done are now presented.

4.3 Description of the acquisitions

4.3.1. Experimental setup

The experimental setup is composed by the following elements. The RASMUS scanner is connected to the ultrasound probe. A BK Medical 8804 linear array probe has been used, which parameters have already been given in Table 1. The probe is fixed on a motorized arm that can be moved in the three orthogonal directions in space. The probe can be moved for compressing the phantom for example. Both RASMUS and the motors that control the position of the probe are linked to a computer where the user can send his commands. The motorized arm is also controlled using Matlab functions. The phantom is in a water tank full of degassed demineralized water. All the different elements are presented in Figure 4-1.

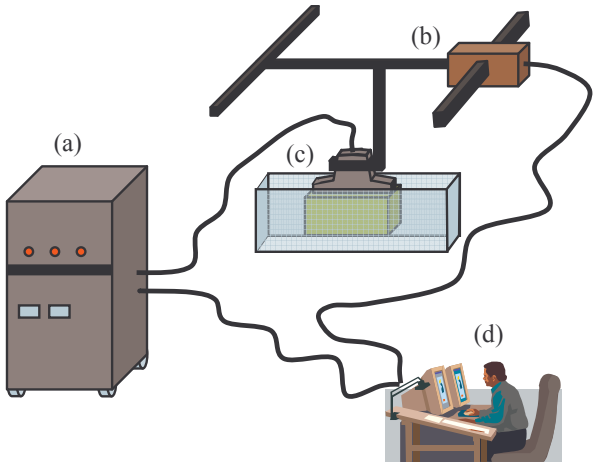

Figure 4-1: Schematic of the experimental setup, (a) the RASMUS scanner, (b) the motorized arm that holds the probe, (c) the probe on top of the phantom in the water tank. The scanner and the motor are connected to the user's computer (d).

4.3.2. Phantoms

We have acquired a good experience in the construction of phantoms dedicated to tissue elasticity imaging with ultrasound. Fromageau *et.al.* in 2003 [20] give a description of the characteristics of the material that is used, which is called cryogel.

Cryogel is a Polyvinyl Alcohol (PVA) solution of concentration 10%. It has the interesting property of getting harder with freeze thaw cycles. As a consequence it is possible to control for example the elasticity contrast between two cryogel mediums by making more freeze cycles for one medium.

Also what is interesting with the cryogel is that the acoustic characteristics and the mechanical characteristics are controlled separately. Indeed a silicate powder is added to the cryogel and plays the role of acoustic scatterers. As the concentration of silicate is independent on the number of freeze cycles two mediums can have the same acoustic characteristics and different stiffness.

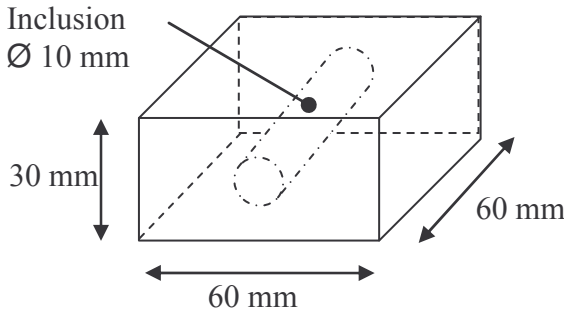

Figure 4-2: Geometry of the phantom. The cylindrical inclusion is stiffer than the rest of the medium; it has a diameter of 10 mm. It is situated in the middle of a parallelepiped of 60x60x30 mm

In order to obtain a phantom that has geometrical parameters approaching the one used in simulation it has been constructed as follows. First the inclusion is constructed. The inclusion is made with a cylinder of radius 5 mm for a length of 60 mm. Two or more freeze cycles, depending on the needed elasticity contrast are made. Moreover, two homogeneous control phantoms are constructed of 10x10x30 mm. Then, the rest of the phantom is made in a parallelepiped mould of 30x30x60 mm with the inclusion fixed in its middle. The geometry of the phantom is given in Figure 4-2. Two control

phantoms are also constructed with the same gel as the one used for the rest of the phantom. A photo of the mould for the whole phantom and for the control phantoms is given in Figure 4-3.

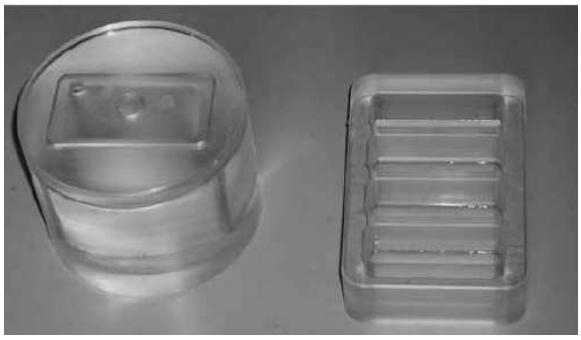

Figure 4-3: Mould for the construction of the phantom and for the control phantoms

Additional information for the cryogel can be found on the following web page, http://home.att.net/~kchu/. Information can also be found in [20] for ultrasound applications or in [66] for MR applications.

4.3.3. Acquisitions

Two types of acquisitions have been made. The aim of the first acquisitions was to test the possibility of estimating purely lateral translations of the medium. This is interesting for evaluating the performance of the estimation without axial estimation first. Indeed, if both are present it would be hard to evaluate the origin of possible errors.

In this case the phantom was standing still in the bottom of the water tank. And the probe was moved by the xyz-translation system, in order to have a pure lateral displacement inside the image plane. The steps between two successive acquisitions were 12.5 micrometers. The principle of those acquisitions is shown in Figure 4-4.

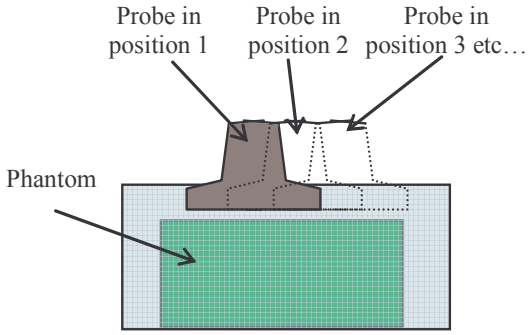

Figure 4-4: Principle of the acquisition with only lateral displacement. The phantom is still in the bottom of the water tank. The first image is acquired with the probe in position 1, the second with the probe in position 2 etc…

The second type of acquisitions consisted on the compression by the ultrasound probe of the phantom. The phantom was standing still in the bottom of the water tank. Before beginning the acquisition the probe was brought in contact of the phantom and a pre-compression of the phantom of about 10 percents was made, in order to insure that the probe and the phantom were in contact for the whole

surface of the probe. This corresponds to applying a displacement of 3 mm on the top of the phantom. Between two successive acquisitions, the probe was moved axially with steps of 150 micrometers.

For both kinds of acquisitions, the configuration of the RASMUS system was the same. 64 elements were excited at the same time by a four cycles sinusoid of same frequency as the center frequency of the 8804 probe, 7MHz. This corresponds to the emission of a plane wave. The transmit elements were weighted with a Gaussian apodization function. The raw data from the same 64 elements as the ones used in emit, were acquired at a frequency of 40 MHz and stored on a PC in order to be processed later. The depth of investigation was set from zero to 30 mm which is the length of the axial dimension of the phantom. The active part of the probe was swept in order to cover the whole aperture. As the total number of elements that can be accessed is equal to 128, the whole acquisition consisted of 65 emissions. As a result each image consists of 65 sets of 64 raw signals each.

Before beamforming according to the parameters given in Chapter 3, the raw signals are match-filtered with the time reversal of the excitation pulse. This enables to increase the signal-to-noise ratio of each raw signal by decreasing the influence of the electrical noise.

4.4 Point spread function

Before showing the results of the estimation, let's first have a look on the shape of the point spread function. The data for those PSFs have been acquired with a wire phantom. The wire phantom is presented in Figure 4-5. The probe is fixed on the top of the phantom. The wires are parallel to the azimuthal direction, perpendicular to the image plane. The wires situated at different depths enable to have the PSF for different depths. In the image plane, the wire appears as a point scatterer, which is the reason why those phantoms are adapted for PSF measurements.

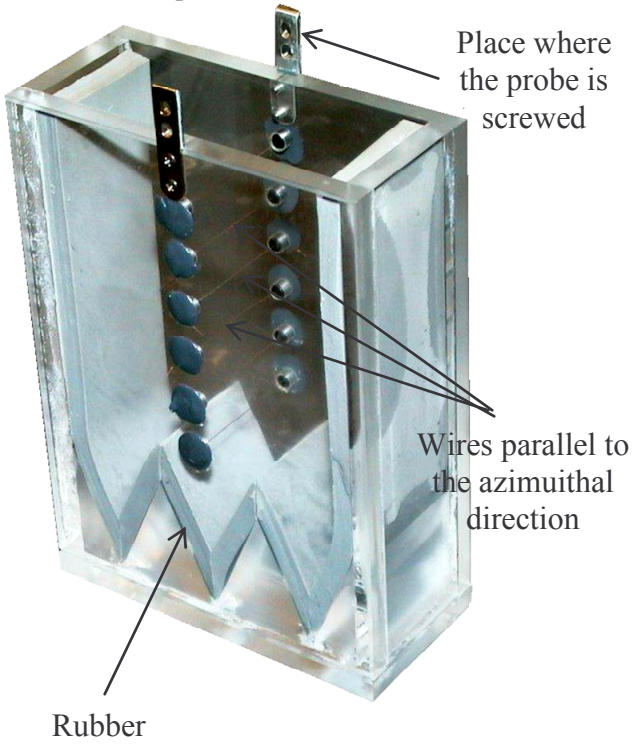

Figure 4-5: Wire phantom. The probe is fixed on the top of the phantom. The wires are parallel to the azimuthal direction. Here rubber has been placed on the bottom and sides of the phantom to avoid high reflections coming from the edges of the phantom. For the same reason, the surface of the bottom of the phantom has different angles.

The raw data are beamformed in receive. Quadratic dynamic focusing is used, and the dynamic apodization function of Figure 4-6 has been used. The emission was a plane wave.

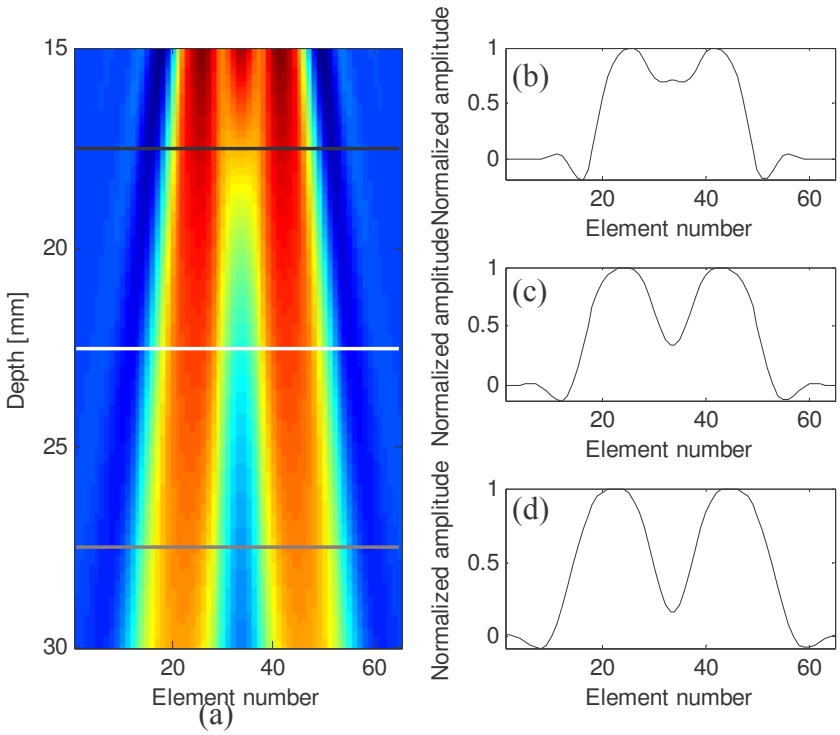

Figure 4-6: Dynamic apodization function used for depths between 15 and 30 mm (a) and profiles corresponding to the black, white and grey lines at depth 17.5, 22.5 and 27.5 mm, (b), (c) and (d), respectively. The apodization function is obtained by the back-propagation method.

The resulting PSFs are shown in Figure 4-7, with the corresponding profiles.

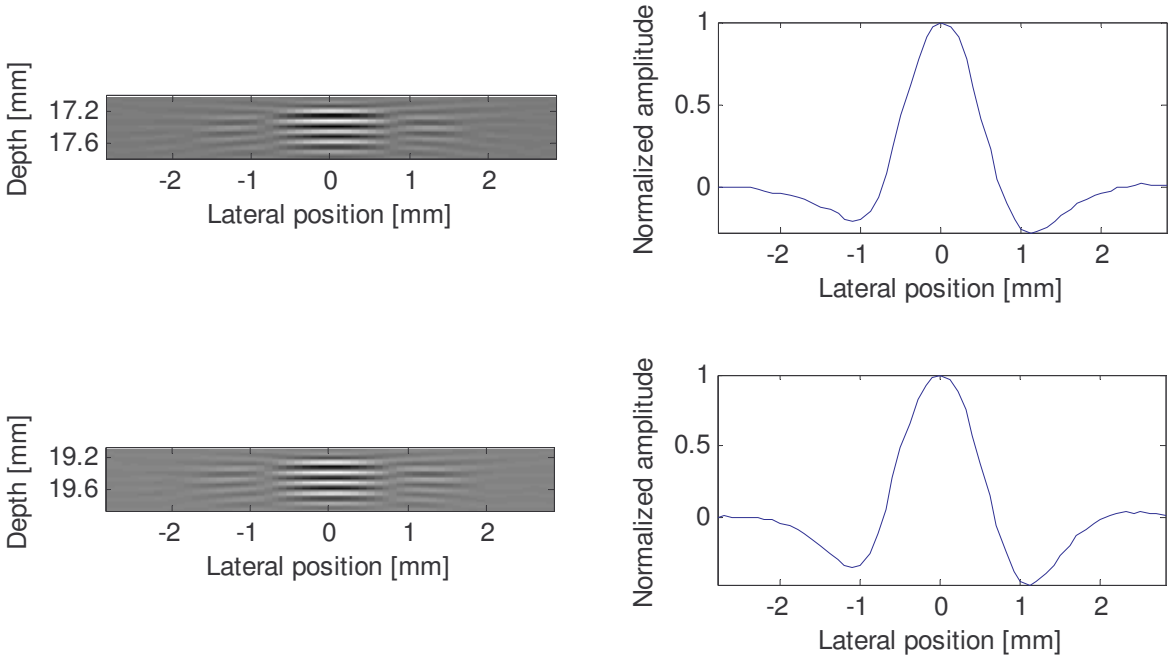

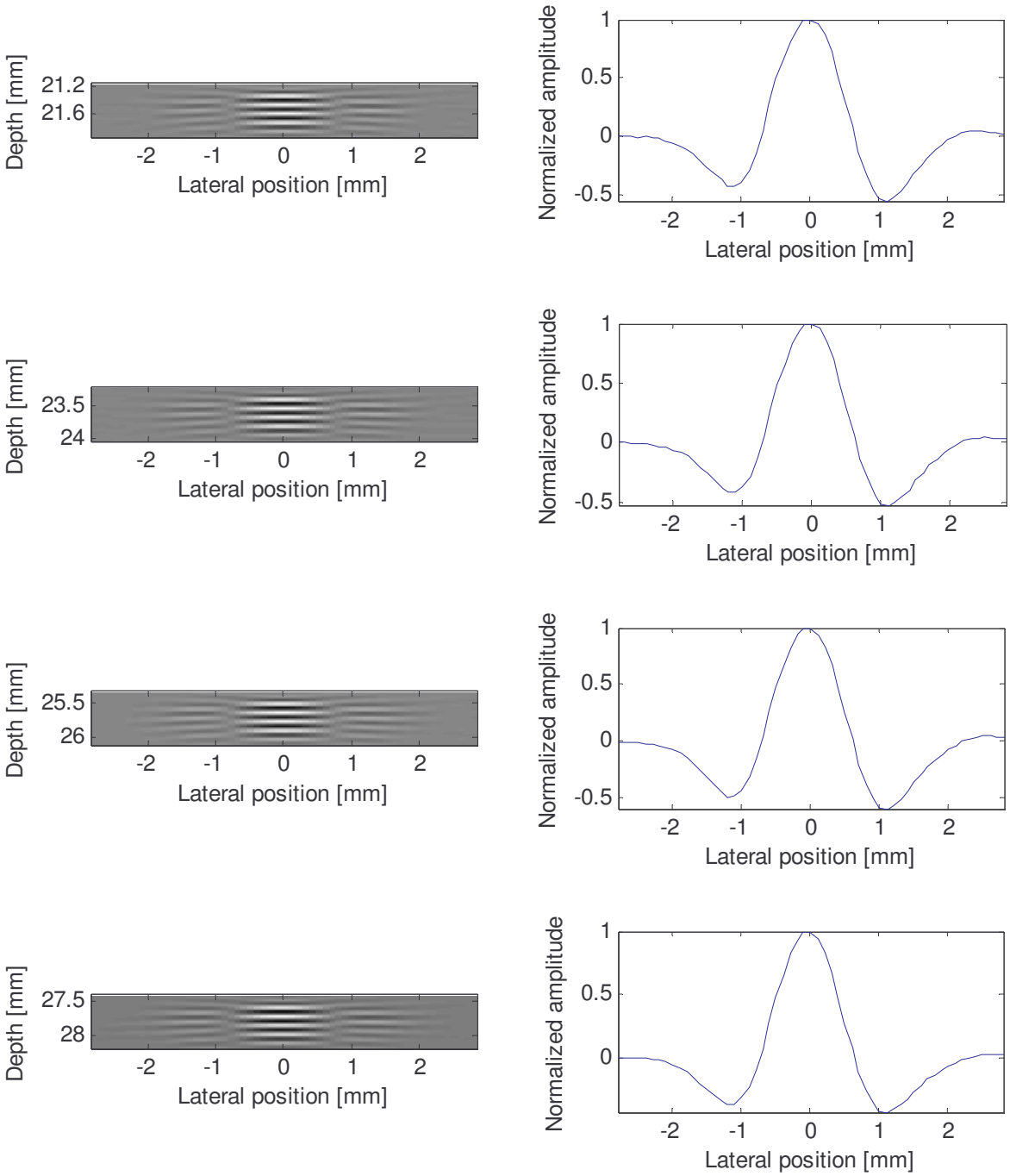

Figure 4-7: Experimental point spread functions acquired with RASMUS using a wire phantom and corresponding lateral profiles. PSFs are shown for depths between 17 and 28 mm.

In Figure 4-7, the lateral profiles show clearly an oscillation, like in the PSF obtained in simulation and shown in Annex B. The expected lateral wavelength is supposed to be 2.6 mm. Here, the distance between the two minimums of the profile measures around 2.2 or 2.3 mm. The obtained wavelength is a bit inferior to the expected one.

The PSFs are also a bit unsymmetrical. The minimum on the right side of the profiles is a bit inferior to the left one. This is probably due to a small angle between the azimuthal direction and the wires. But, what is really interesting here is to see how good it is possible to control the shape of the PSF for the different depths. Indeed the lateral profile remains constant for depths between 17 to 28 mm.

4.5 Results

The results for the case of a purely lateral displacement between the images are given. The result for a 2D case of a compressed phantom having a hard inclusion is also given.

4.5.1. Lateral displacement only

With the first acquisition with only lateral displacement between two images the following procedure has been used. The first image has been used as reference. Then it has been divided into 1D windows. Each window is a part from a lateral RF signal. Then, the lateral displacement between each following image and the reference image has been estimated. As the displacement was supposed to be purely lateral, the axial displacement was not estimated. Each image has been divided like the first one. The phase zero crossing of the complex correlation between two corresponding windows has been estimated with the Newton method.

Before looking at the estimation results, it is interesting to have a look first, as for the simulations, on the shape of the envelope and phase of the complex auto-correlation functions of the lateral RF signals. Figure 4-8 gives a representation of those functions.

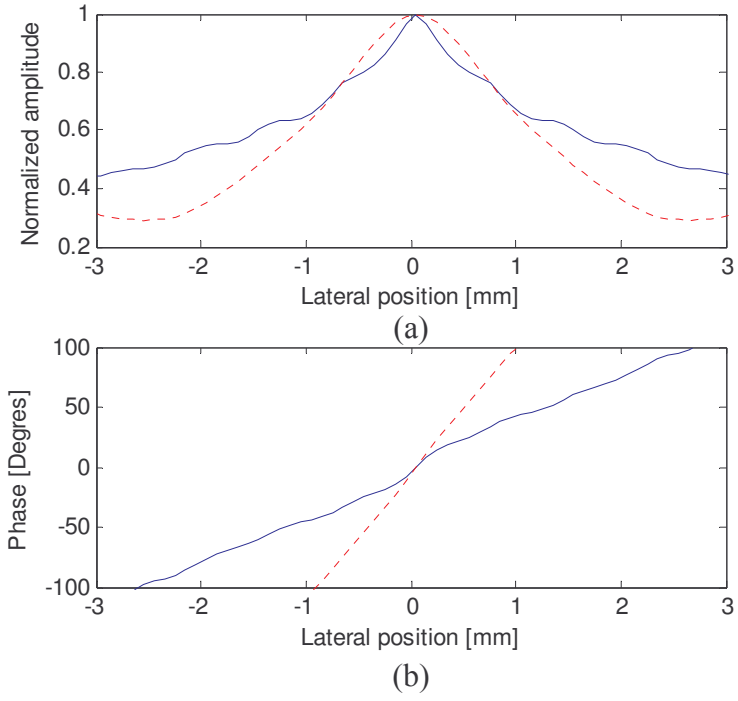

Figure 4-8: Shape of the envelope and phase of the complex correlation functions of the lateral RF signals. (a) solid line for the lateral RF signals of the conventional images, and (b) dotted line for the lateral RF signals of the lateral oscillations images.

As for the simulations, the phase in the case of the lateral oscillations is steeper and more linear than in the conventional images. With the conventional images the phase slope is nearly 42°/mm and for the lateral oscillations it is around 100°/mm. The values are not exactly the same than in simulation but

they are in the same order of magnitude. There is nearly a factor of two between the slopes of the two phase curves, which is the same ratio as in the simulations.

Figure 4-9 shows the mean estimate and standard deviation for each image compared to the true displacement. This representation is done for both the conventional images and the lateral oscillations.

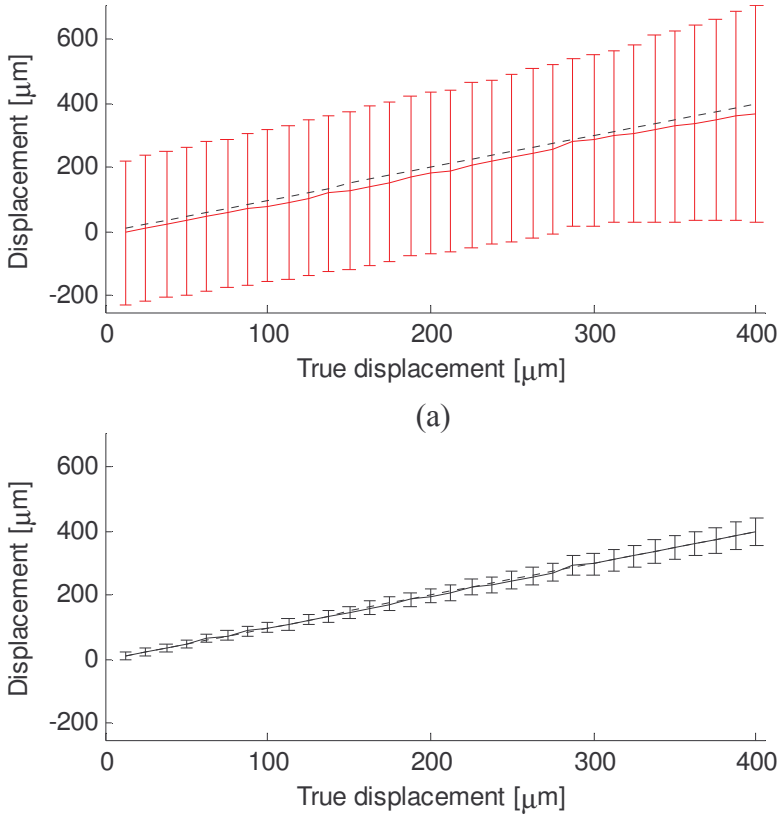

Figure 4-9: Mean estimate and standard deviation with respect to the true displacement for the purely lateral displacement case. (a) with the conventional images, (b) with the lateral oscillations. The dotted line represents the true displacement.

Figure 4-9 shows clearly that the method performs much better with lateral oscillations images than with conventional images. With the lateral oscillations the mean error is equal to 1µm whereas for the conventional images it is around 30 µm.

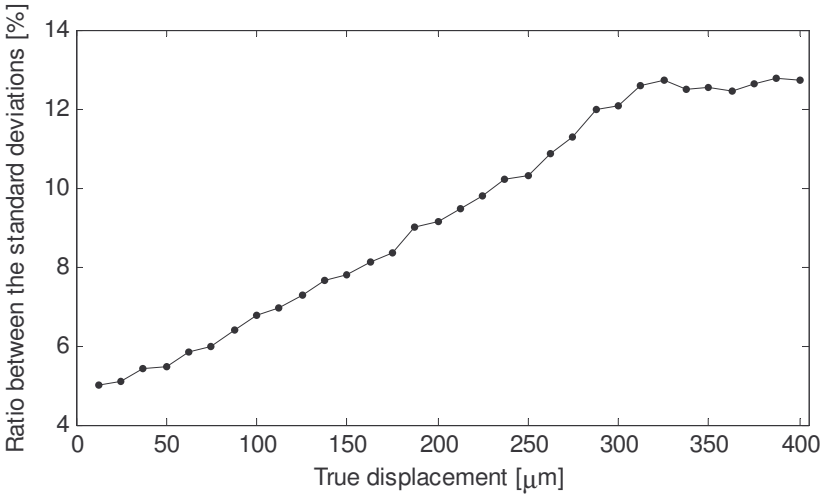

Figure 4-10: Ratio, in percents, between the standard deviation obtained with lateral oscillations and the one obtained with the conventional images, as a function of the lateral displacement to be estimated

Figure 4-9 shows also that the standard deviation in the case of the lateral oscillations is much smaller than with the conventional images. Figure 4-10 shows the ratio in percents between the standard deviation obtained with the lateral oscillations images, and the one obtained with the conventional images as a function of the displacement to be estimated. The ratio is under 10% until 200 μm displacement. For large values, the ratio between the standard deviations seems to stabilize itself around 13%. This still means that the accuracy of the estimation is more than 7.5 times better with the new beamformed images showing lateral oscillations.

It is also possible to take a look at the global histograms of the error in Figure 4-11. The first histogram shows the distribution of the error between the estimated displacement and the true displacement for the whole range of displacement tested, from nearly 10 μm to 400 μm, for the conventional images. The second one shows the same histogram obtained with the lateral oscillations images. And the last one is the histogram of the difference between the two estimates, the one obtained with the conventional images and the one obtained with the lateral oscillations images. In the first histogram for conventional images, the standard deviation of the error distribution is 262 μm, in the second histogram with lateral oscillations it is 26.8 μm, and for the difference between the two estimates it is again 262 μm. The histogram of the difference is really close to the histogram of the error obtained with the conventional images.

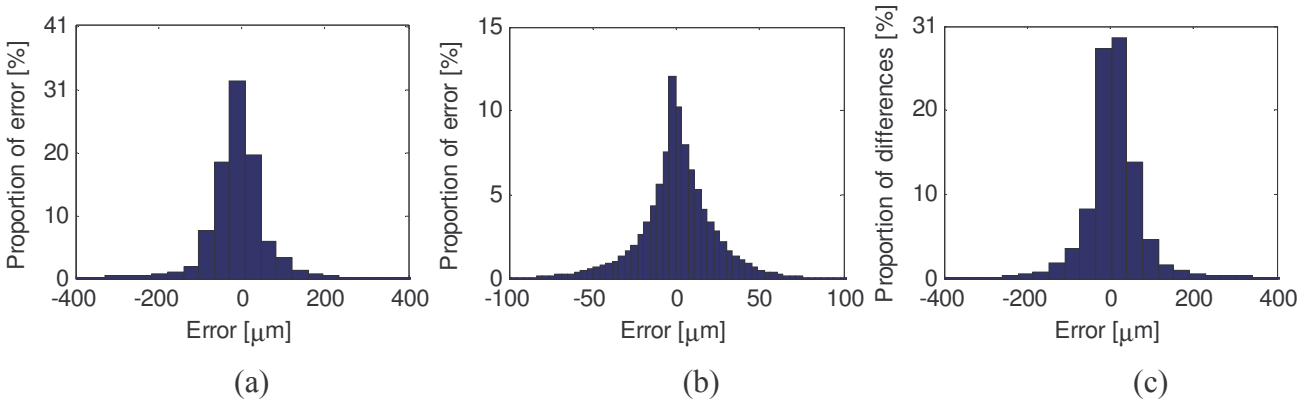

Figure 4-11: Histograms of the error for the purely lateral displacement, (a) with the conventional images, (b) with the lateral oscillations images, (c) the difference between the two estimates

This preliminary study shows that even with experimental data the lateral oscillations images give the possibility to estimate the component of the displacement perpendicular to the beam axis with a good precision. More over the quality of the estimation is improved compared to conventional images.

4.5.2. Phantom with inclusion

The final investigation consists of the estimation of the two components of the displacement along and perpendicular to the beam axis in the case of a compressed phantom. The phantom was a parallelepiped with a cylindrical inclusion.

Figure 4-12 shows an arrow representation of the estimated displacement field inside the phantom superimposed to a B-mode image of the phantom. The coordinate system is supposed to be fixed in the middle of the phantom. This is the reason why the phantom seems to move up in the bottom of the phantom and down in the top of the phantom. It is simply a question of reference. The representation gives the result with conventional images and with our images with lateral oscillations.

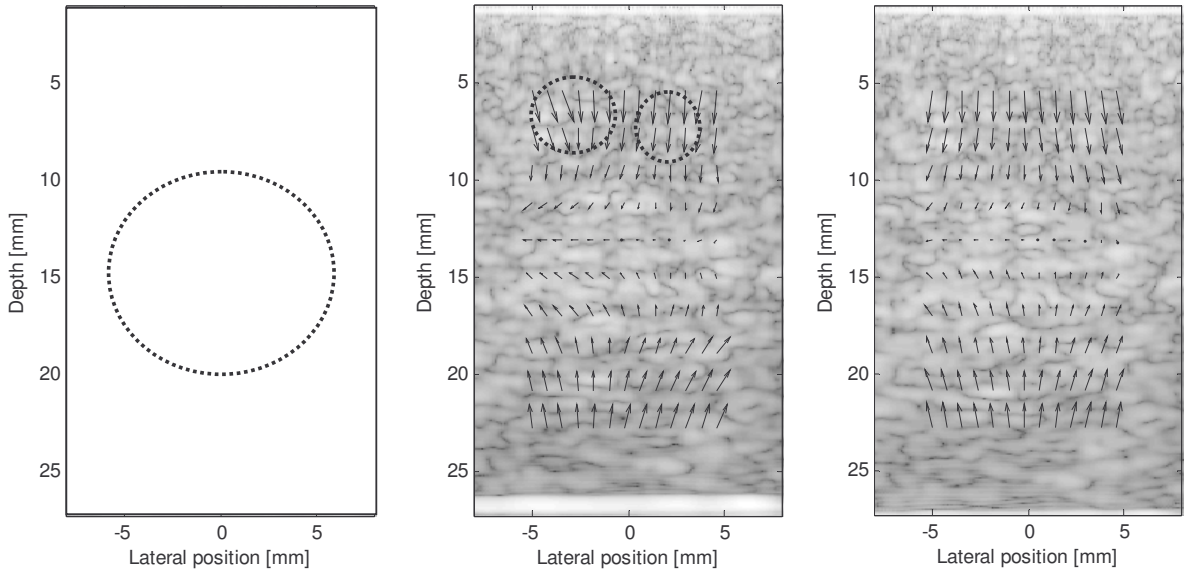

Figure 4-12: (a) gives approximately the geometrical configuration of the phantom with the inclusion indicated by the dotted circle. (b) and (c) are arrow representations of the 2D displacement field calculated from experimental data superimposed on the B mode image, (b) with conventional images, (c) with lateral oscillations,. On (b) the circles indicate places with probably *false* estimated displacement vectors.

Figure 4-13 and Figure 4-14 show separately the estimated axial and lateral displacement maps obtained with the conventional images and those obtained with the lateral oscillations images, respectively.

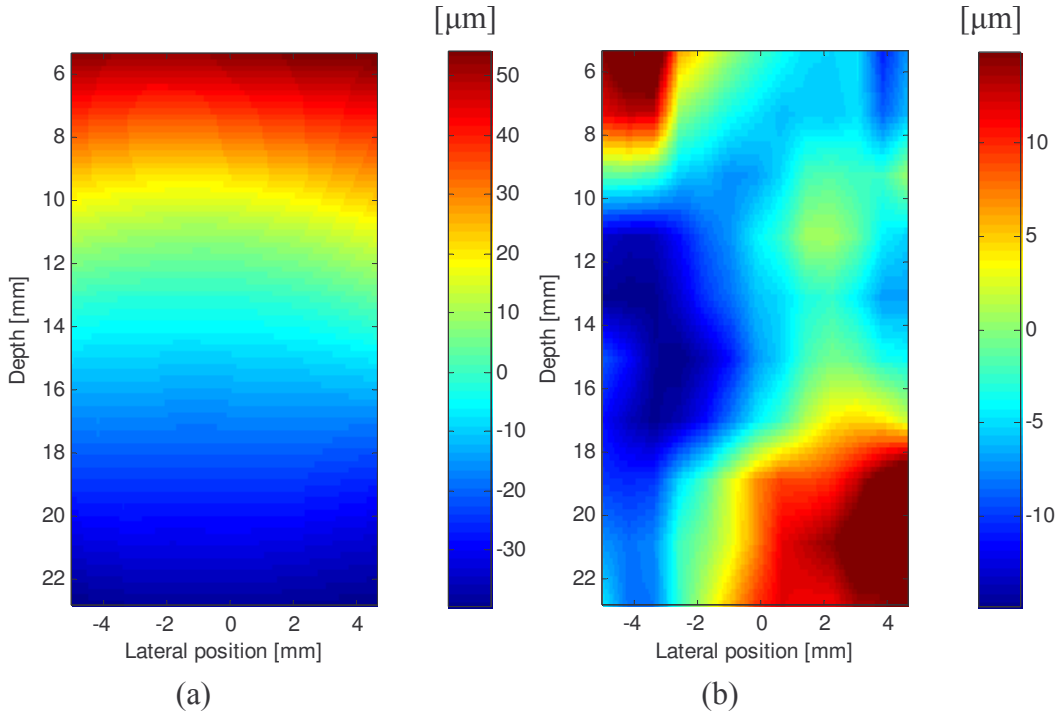

Figure 4-13: (a) Axial and (b) lateral displacement maps estimated with the conventional images, in µm.

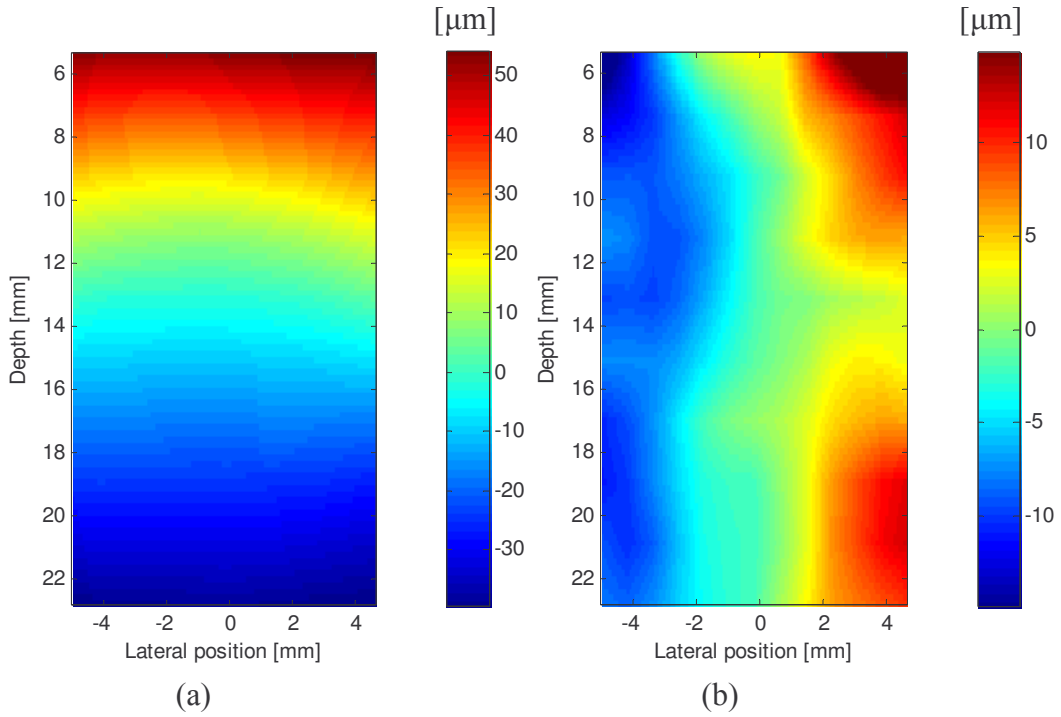

Figure 4-14: (a) Axial and (b) lateral displacement maps estimated with the lateral oscillations images, in µm.

As the probe was standing on the top of the phantom of Figure 4-2, the inclusion is supposed to be here in the middle of the different images.

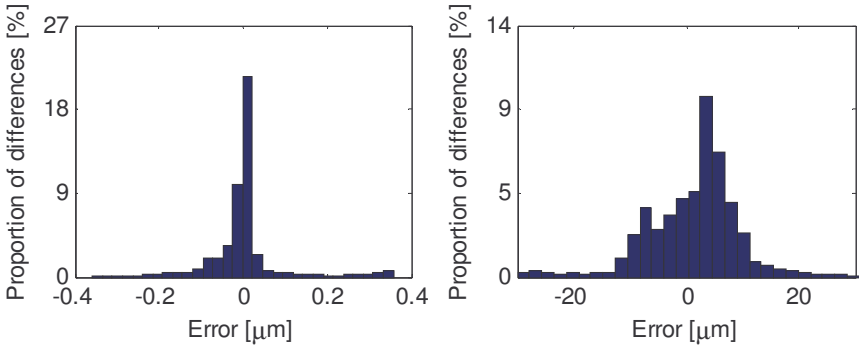

Figure 4-15: Histograms of the difference between (a) the axial estimate with the lateral oscillations and the axial estimate with the conventional images. (b) is the histogram of the differences between the lateral estimate with lateral oscillations and the lateral estimate with the conventional images.

As for the simulations the histograms of the differences between the estimation with the lateral oscillations and the estimation with the conventional images for the axial and lateral estimates are given. The two histograms are given in Figure 4-15. The standard deviation for the axial difference is equal to 0.08 μm and the standard deviation for the lateral difference is equal to 8.41 μm.

4.6 Discussion

First it is important to recall that it is possible to control the shape of the PSF experimentally by receive beamforming the raw single-element data acquired with RASMUS.

The study with only lateral displacement between two acquired images has let us hope for good experimental results also in the 2D case. Indeed it has been possible to estimate a purely lateral displacement with a mean error roughly close to zero. The estimation's accuracy is better with lateral oscillations images. The standard deviation obtained with the new beamformer is more than 7 times smaller than the one obtained with conventional images.

More over Figure 4-11 shows finally that the histogram of the difference between the estimation obtained with conventional images and the one obtained with the lateral oscillations images looks really like the one of the error with conventional images. As there is a ratio of nearly 10 between the two standard deviations, the error in the lateral oscillations images can be neglected compared to the one of the conventional images.

For the compression of the phantom with the probe, as the exact geometry of the phantom and its exact mechanical characteristics are not known, the results can only be commented qualitatively.

Let's first comment the axial estimation. The total axial displacement applied with the motorized arm was 200 μm. In our case the displacement difference between the top and the bottom of the phantom is equal to roughly 100 μm (55 minus -45). And this doesn't take into account the extreme top and the extreme bottom of the phantom. The plot begins at a depth of approximately 6 mm and ends at a depth of approximately 22 mm. If the displacement could be known in the part of the phantom that has not been plotted and added to the total displacement we would probably be closer to 200 μm. More over the part that is plotted is supposed to include the hard inclusion in which the displacement is smaller

than outside the inclusion. It is important to notice that, for the depth of the inclusion (around 14 mm), as its radius is 5 mm, no estimation point is completely outside the inclusion.

No real “accident” in the estimation seems to appear on the maps representing axial displacement in Figure 4-13 and Figure 4-14.

More over it is interesting to notice that there is no real difference between the axial estimation obtained with conventional images, and the one obtained with our images. This was predicted by the simulation results. It can be seen on the histogram of Figure 4-15.

Concerning the lateral displacement it is more complicated. The global tendency seems to be correct when using lateral oscillations images. On one side of the phantom the displacement is positive and on the other side it is negative. This is the resulting displacement scheme due to an axial compression. However, with the conventional images there are incoherent results, particularly on the top of the phantom. On the lateral displacement map of Figure 4-13, there are places in the left part of the phantom that have a positive lateral displacement value. This means that this part of the medium has a displacement vector that points towards the middle of the phantom. This can also be seen on the arrow representation of Figure 4-12, where the places where the accidents are present are inside the dotted circles. This is not coherent and leads to the conclusion that the lateral displacement map estimated on images having lateral oscillations has a better accuracy than the one obtained with conventional images.

The histograms of the differences between the axial and lateral displacement maps, obtained with the two kinds of images, are given in Figure 4-15. They are coherent with the same histograms given in simulation, *i.e.* there is a small difference between the axial displacement maps compared to the difference between the lateral displacement maps. Here the true displacement is not known, but it is reasonable to believe that our displacement map is closer to the true one, especially because in our case there is no “accident” in the estimation. More over the comparison of the estimation’s accuracy for a purely lateral displacement also leads to this conclusion. Indeed in the case of a purely lateral displacement it is shown that the histogram of the difference is really close to the histogram of the error with conventional images.

The standard deviation of the lateral difference is quite large compared to the displacement estimated, it is equal to 8.4 µm for a maximum lateral displacement situated between 15 and 20 µm. But this in not so surprising, because of the accidents where even the sign of the estimated displacement must be false for the conventional images.

In the simulation results the influence of the hard inclusion could be seen with a displacement varying slower inside the inclusion. Here this can hardly be seen in the axial estimate and it is not seen for the lateral estimate. But it is important to notice that the size of the region of interest is very small in the lateral direction. It covers only 1 cm which is the diameter of the inclusion.

Different aspects can be responsible for these results. First it is logical that the axial estimate is still better than the lateral one. In the simulation where the shape of the PSF was perfectly controlled, even for the most optimized parameters the results were not perfect.

In the experimental investigation there can be many sources of error, such as noise, and the results are obligatory worse than for simulation if the simulations don’t take into account all sources of error.

But what this experimentation shows is that even with equipment, and particularly the ultrasound probe, that hasn't been developed for our purpose some results can be obtained. And what is even more interesting is that changing the image formation has really an impact on the obtained results.

This means that not only the signal processing method influences the final results, it is important to take into account the image formation models and the imaging material. All aspects should be designed in parallel to the other ones. Controlling the image formation is a crucial aspect for getting accurate results.

Summary, conclusion and perspectives

In this thesis a new method for estimating 2 components of the displacement between two ultrasound RF images has been introduced in the field of tissue elasticity imaging.

While others have been using conventional ultrasound images for estimating displacement between images, it bas been shown in this thesis that a dedicated PSF can be used for increasing the accuracy of a given lateral displacement estimation method.

The first chapter first recalls the medical interest of ultrasound tissue elasticity imaging. Then the laws of the mechanics have been presented in order to understand why estimating more than just one component of the displacement field is important. Then different methods able to estimate several components of the displacement field are presented (block matching, optical flow, multiple crossed beams, lateral oscillations). The idea that has been the starting point for this thesis is the adaptation of the image formation to the particular case of one given displacement estimator.

In the second chapter ultrasound imaging is presented more precisely, beginning with the presentation of the physical principle involved in echography. A simple system approach enables to describe the formation of the radio-frequency ultrasound image by convolution between a point spread function (PSF) and a distribution of scatterers in the medium under investigation. Beamforming enables to control the shape of the PSF, and we present a beamformer design method. The idea is to emit a broad beam and to beamform only during receive because all beamformer parameters can be adapted dynamically, which is not the case in emit. In this case quadratic dynamic focusing is used. A dynamic apodization function is also calculated using a back-propagation approach. Fourier relation given by Frauhnoffer approximation is presented as a good tool to give interpretation of the shape of the apodization functions. It has the advantage of being analytical, but it is less precise than back-propagation.

In the third chapter our new estimation method is presented. The estimation is based on the study of the phase of the complex cross-correlation between two displaced versions of a given signal. This phase crosses zero for the true displacement value. Starting from the statement that lateral RF signals have this particularity, the phase of the complex correlation is forced to be linear. This leads to choose a point spread function being a Gaussian envelope modulated by a sinusoid. The apodization function that leads to such a PSF shows two Gaussian peaks. The distance between the peaks is proportional to the frequency of the oscillations, and the width of the peaks is inversely proportional to the width of the PSF. The optimal parameters of the PSF with respect to the size of our probe are given. The estimation is tested in simulation and a comparison between the estimation with conventional images and with images having lateral oscillations is presented. The improvement for a purely lateral displacement is a factor of 8 or 9. The optimal window sizes for the twice 1D estimation are also given. In the 2D case the improvement is around a factor of 3. As final example the estimation result for a case where the lateral oscillations could be as fast as the axial ones is given. In this case, as expected, the estimation accuracy is the same in both directions.

In the last chapter experimental results are shown. The RASMUS scanner from the Center for Fast Ultrasound imaging has been used. It is a customized scanner dedicated to beamforming and more generally advanced techniques for research in ultrasound imaging. The point spread functions acquired on a wire phantom are presented. Then the estimation in the case of a purely lateral displacement is presented showing that the method has a good potential for estimating lateral displacements. A cryogel phantom of controlled geometry has been constructed. It contains a hard cylindrical inclusion. The stiffness of the cryogel is controlled by the number of freeze-defreeze cycles applied to the medium. A comparison between the estimation on lateral oscillations images, and on conventional images is given. Our displacement map seems coherent whereas with conventional images there seem to be some accidents.

This thesis work shows that a given signal processing method doesn't work the same way with any kind of image. The formation of the image has an extremely high impact on the quality of the estimation. As a consequence, it is extremely important to design the image formation techniques, the ultrasound transducers, and the signal processing methods together, in order to reach optimal results.

In the future different points have still to be investigated more deeply.

The beamformer design is the first point. The back-propagation method is interesting and seems to give PSF in good agreement with the expected ones. However it is obvious that emitting a broad plane wave is not optimal. The energy is spread over a large area. It could be interesting to use synthetic aperture in order to be able to focus and change the apodization function also in emit. Synthetic aperture meets difficulties for application in blood flow because of the fast blood velocity. But in elastography the compression, even in a freehand system could be applied much slower. The aim here would be to increase even more the quality of the estimation by having a higher lateral oscillations frequency and a better resolution (thinner PSF).

An interesting aspect is to investigate the beamforming techniques used in radar and in communication. Synthetic aperture is one example already studied in the ultrasound community which carries high potential for controlling even more the shape of the PSF.

Another idea is to change the estimation method and to adapt the image formation to this new estimation method. In the thesis it has been chosen to work with a specific estimator working with the phase, because it was shown to be very efficient for axial displacement estimation. It has the advantage to be very quick and is a good candidate for real time applications. But for 2D displacement estimation it is perhaps not the most adapted approach. First it is probably possible to investigate the adaptation of the image formation to existing 2D estimation approaches, like block matching or optical flow. But the investigation of new 2D estimators based on lateral oscillations is also a promising way. For example considering two dimensional windows probably improves the robustness of the estimation.

Also it is interesting to work not only with two images, but with a sequence of images. This probably brings also some additional robustness to the calculation. And it can also give some additional information. For example the nonlinearity of the displacement of a given part of the medium, when regular compression steps are applied to the medium.

Annex A: Fraunhoffer approximation.

In this section it will be shown how Fraunhoffer approximation is reached at the focal point. It will also be shown that with some hypothesis it is possible to highlight a Fourier transform relation between the aperture function and the pressure profile

Fraunhoffer approximation for calculating the pattern due to diffraction of a monochromatic wave by any two dimensional aperture can be found in [15]. Here we will make a first simplification by considering only a two dimensional problem. Everything is considered inside the image plane.

Let's first consider a linear aperture consisting of discrete point sources situated at depth $y_0 = 0$. These sources are considered to produce a spherical monochromatic continuous wave. We are interested in the field profile. A weighting function $w(x_i)$ is applied to the elements of the aperture. In this case the pressure at depth y and lateral position x is equal to

$$p(x,y) = \sum_{i=-\infty}^{+\infty} w(x_i) g(x_i, x, y) \tag{A-1}$$

where $g(x_i, x, y)$ is the Green function that corresponds to the propagation from the ith element at position x_i to the point of interest. The number of active elements is of course no infinite, and a number of N elements, corresponding to the number of active elements, have a non-zero weighting coefficient $w(x_i)$. By introducing in (A-1) the expression of Green function in infinite space it is possible to write

$$p(x,y) = \sum_{i=1}^{N} w(x_i) \frac{e^{\frac{j2\pi r_i}{\lambda}}}{r_i} \tag{A-2}$$

λ is the wavelength of the emitted beam and $r_i = \sqrt{y^2 + (x_i - x)^2}$ is the length of the path from the ith aperture element to the point of interest that can also be written as

$$r_i = y\sqrt{1 + \left(\frac{x_i - x}{y}\right)^2} \tag{A-3}$$

Fraunhoffer approximation can be reached either in the far field or at the focal point. In order to satisfy the second point we introduce the delays that enable to be focused.

The reference for the delays is the centre of the probe. Introducing delays is equivalent to introducing in (2-18) the corresponding path lengths defined by

$$\Delta r_i = c\Delta t_i \tag{A-4}$$

and equal to

$$\Delta r_i = \sqrt{y^2 + x_i^2} - y = y\sqrt{1 + \left(\frac{x_i}{y}\right)^2} - y \tag{A-5}$$

In this case the pressure profile is equal to

$$p(x,y) = \sum_{i=1}^{N} w(x_i)\frac{e^{\frac{j2\pi(r_i - \Delta r_i)}{\lambda}}}{r_i - \Delta r_i} \tag{A-6}$$

If Fresnel approximation can be made, it is possible to replace (A-3) and (A-5) by the two first terms of their binomial expansion. This leads to

$$r_i \approx y + \frac{1}{2}\frac{(x_i - x)^2}{y} \tag{A-7}$$

and

$$\Delta r_i \approx \frac{1}{2}\frac{(x_i)^2}{y} \tag{A-8}$$

Fresnel approximation is reached if

$$y^3 >> \frac{\pi}{4\lambda}\left[(x_i - x)^2\right]^2_{max} \tag{A-9}$$

In this case equation (2-18) can be written as

$$p(x,y) = \frac{1}{z}e^{j\frac{2\pi y}{\lambda}}e^{j\frac{\pi x^2}{\lambda y}}\sum_{i=1}^{N} w(x_i)e^{\frac{-2j\pi x_i x}{y\lambda}} \tag{A-10}$$

This expression has been derived using focusing. It can also be reached in the far field. In this case Fraunhoffer approximation is valid if

$$y >> \frac{\pi^2 x_{max}}{\lambda} \tag{A-11}$$

If $\frac{x}{y\lambda}$ is interpreted as a frequency variable, the term inside the sum corresponds to the Fourier transform of the discrete function $w(x_i)$. And regrouping all the terms outside the sum under the variable $\frac{1}{C}$ in (A-10) leads then to

$$p(x,y) = \frac{1}{C}\sum_{i=1}^{N} w(x_i) e^{\frac{-2j\pi x_i x}{y\lambda}} \qquad \text{(A-12)}$$

In some cases only the Fourier transform is considered and the terms outside are not taken into account. This can be done without degrading too much the results in certain physical limits: for example at relatively important depths for thin apertures as given by (A-11).

But more important it gives an extremely interesting feeling of the shape of the aperture functions that can lead to specific pressure profiles. So even if it is less precise this approach has to be kept in mind.

Annex B: Point spread functions

Here the point spread functions of scatterers situated between 2 and 28 mm depth are shown for the optimal parameters obtained with the simulation given in chapter 3, which are: a lateral wavelength $\lambda_x = 2.6$ mm and a standard deviation of the Gaussian envelope $\sigma_x = 2.8$ mm. The aim is to show that the point spread function remains quite constant for the whole depth.

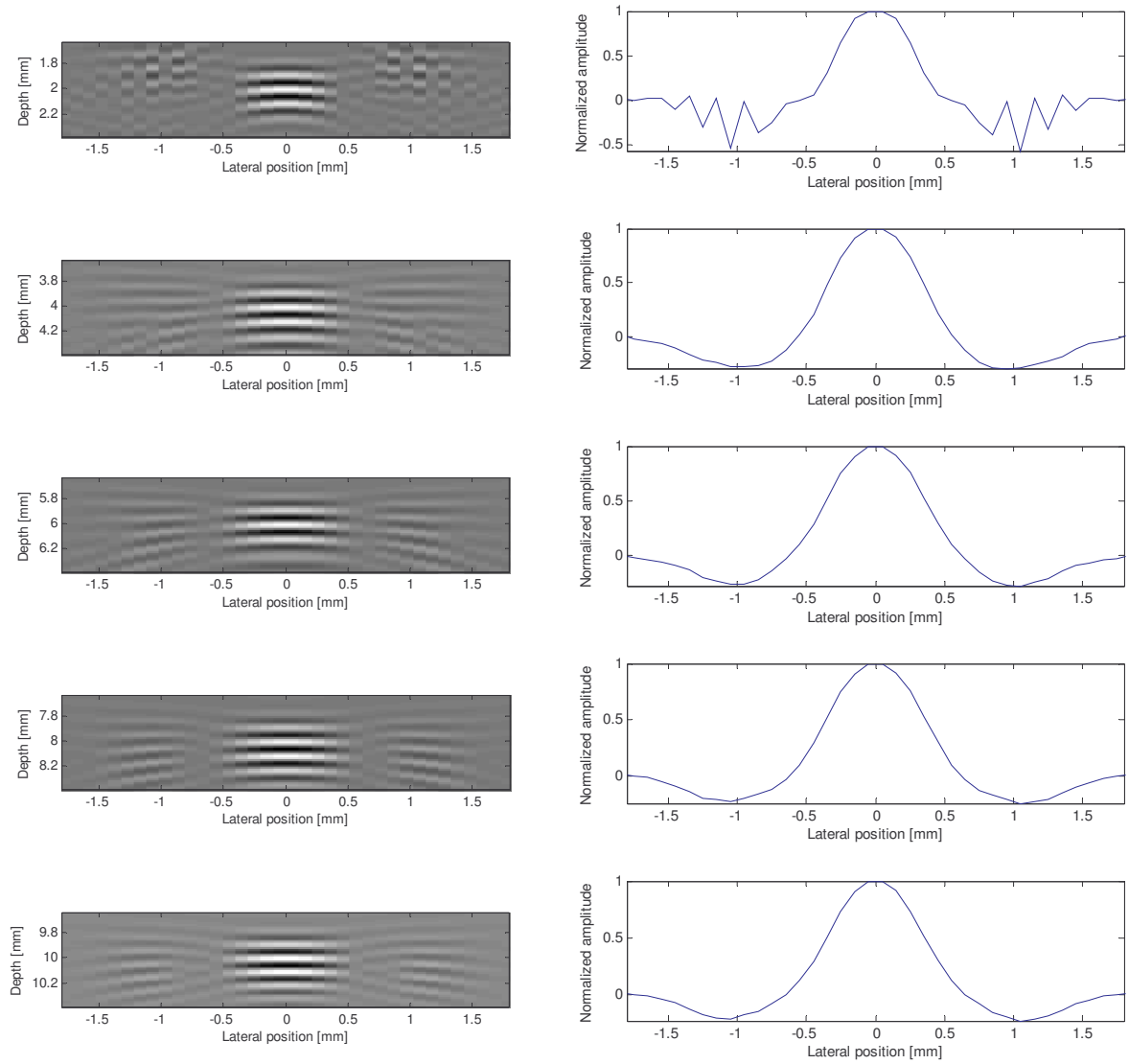

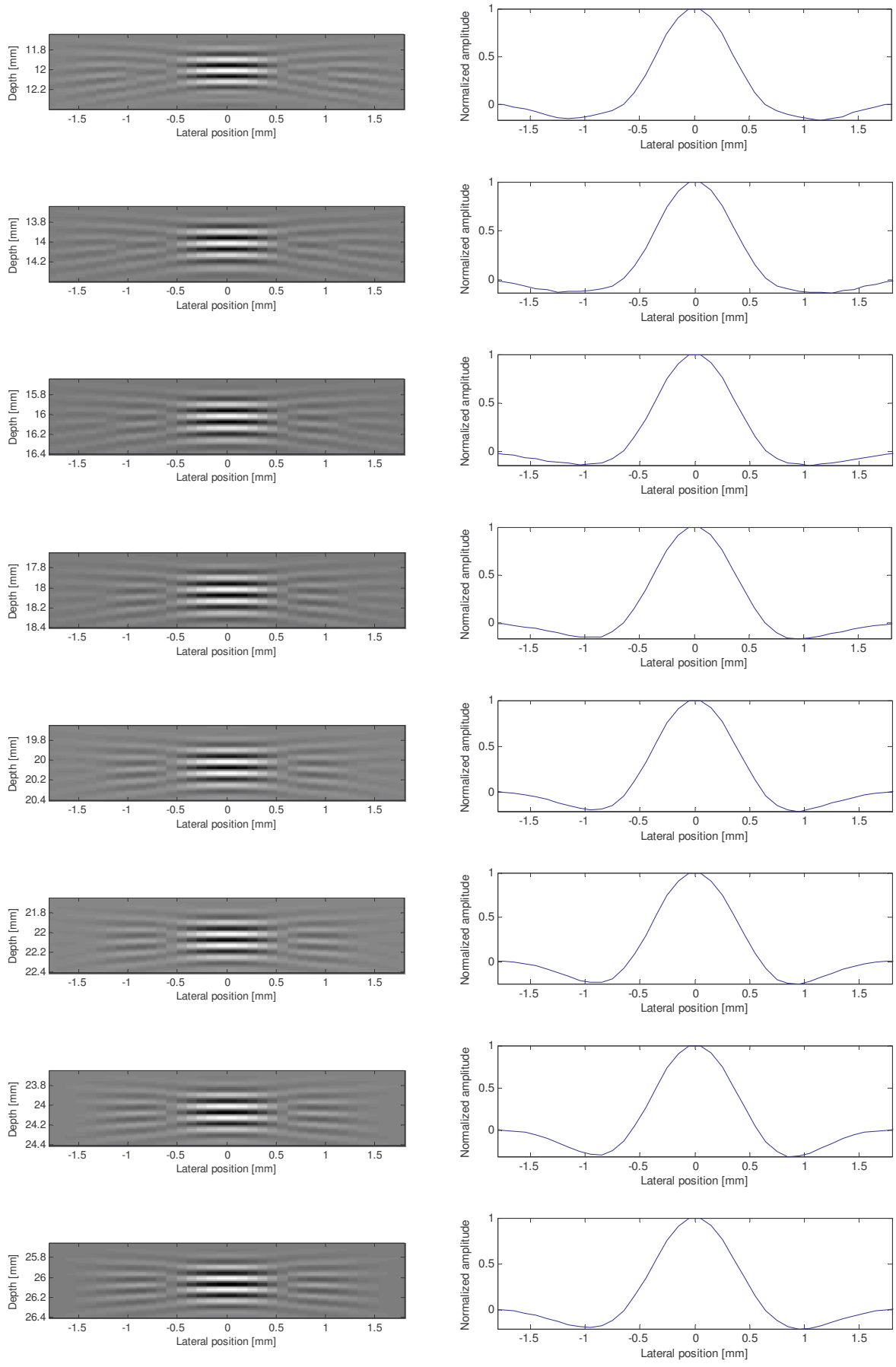
Depth [mm]
11.8
12
12.2
Lateral position [mm]
Normalized amplitude
13.8
14
14.2
15.8
16
16.2
16.4
17.8
18
18.2
18.4
19.8
20
20.2
20.4
21.8
22
22.2
22.4
23.8
24
24.2
24.4
25.8
26
26.2
26.4
-1.5
-1
-0.5
0
0.5
1
1.5

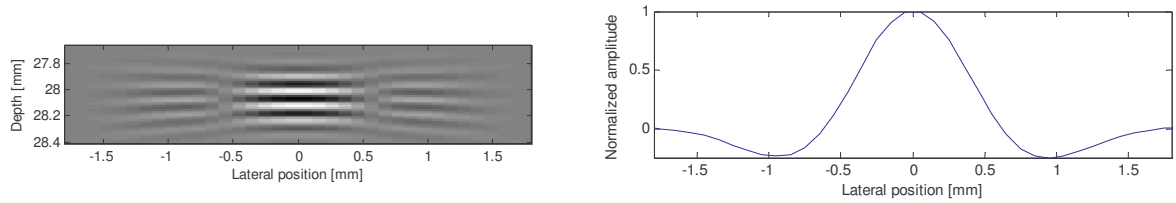

Figure B-1: 2D obtained PSF for depths between 2 and 28 mm, and associated lateral profiles

The observation of the different point spread functions, and their corresponding profiles learns us first that it is not possible to control the lateral profile with a precise accuracy at the very near field. The PSFs at 2, 4 and even 6 mm depth are clearly different from the others. However, for more important distances away from the transducer the PSF remains quite constant.

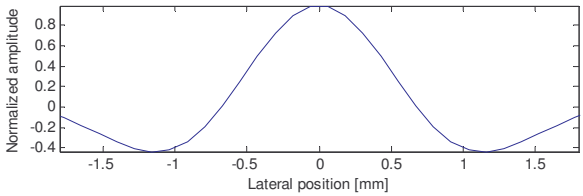

Figure B-2: Expected lateral profile

The shape of the profile doesn't really change, and the correlation coefficient between the expected lateral profile and the obtained profile of Figure B- is always higher than 95% for any depth between 4 and 28 mm.

Here the conclusion that the lateral profile of the PSF can be controlled can be made.

Annex C: Definition of the notion of strain

This annex recalls the way the strain tensor has been defined. It can be found in many books. Here the notations are inspired from Fung's book on biomechanics [67].

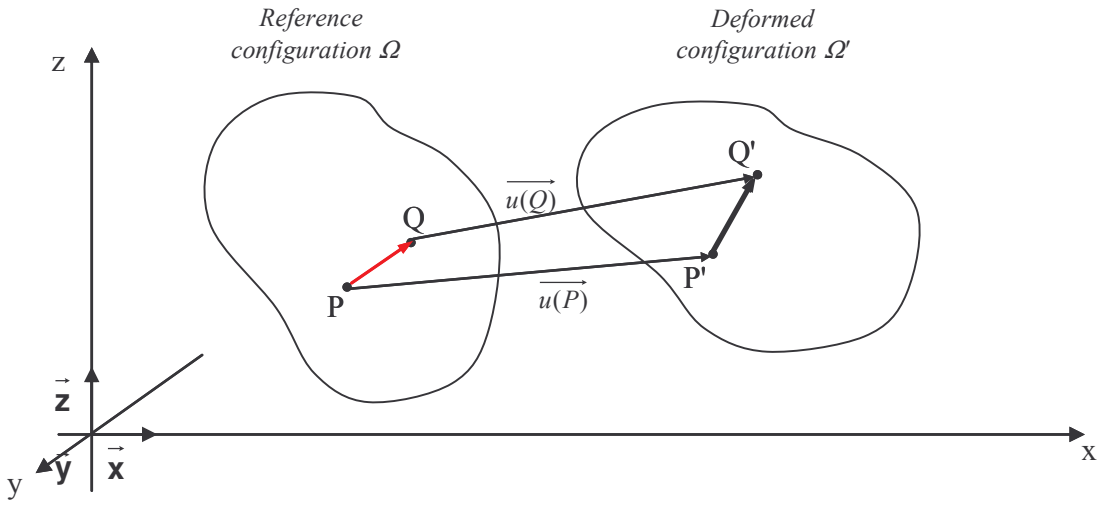

Figure C-1: A vector PQ in the initial configuration becomes P'Q' in the new configuration

Let's consider the configuration shown in Figure C-1, representing a continuous medium in a reference state Ω and in a deformed state Ω'. Every particle of the medium has a set of coordinates. In the deformed medium every particle takes a new position described by a new set of coordinates. For example a particle P is initially at position (x_1, x_2, x_3) and it is moved to a new position P' of coordinates (x_1', x_2', x_3').

The vector **PP'** or **u** is called the displacement vector. The components of the displacement vector are

$$u_i = x_i' - x_i, \text{ with } i = 1,2,3 \tag{C-1}$$

If there is a mapping from (x_1,x_2,x_3) to (x_1',x_2',x_3') that describes the new coordinates of any particle as a function of the reference coordinates, the deformation is known. The mapping consists of a set of functions defined as

$$x_i' = f_i(x_1, x_2, x_3), (i = 1,2,3) \tag{C-2}$$

This transformation is assumed one to one, *i.e* the function in (C-2) are single valued, continuous and have a unique inverse. In this case it is possible to write that

$$x_i = g_i(x_1', x_2', x_3'), (i = 1,2,3) \tag{C-3}$$

If a particle Q of coordinates $(x_1+dx_1, x_2+dx_2, x_3+dx_3)$, infinitely close to P, is considered. The square of the length ds_0 of the vector $\mathbf{PQ}$ is given by Pythagoras rule because the space is assumed to be Eucledian, this length is equal to

$$ds_0^2 = dx1^2 + dx2^2 + dx3^2 \tag{C-4}$$

Here the kronecker symbol is introduced as

$$\delta_{ij} = \begin{cases} 1, \text{if } i = j \\ 0, \text{elsewhere} \end{cases} \tag{C-5}$$

In the following equation we will use Einstein's notation in order to lighten the equations. This notation uses the convention of a summation over an indice which is present twice in an expression. Using this notation (C-4) can be written as

$$ds_0^2 = \delta_{ij} dx_i dx_j \tag{C-6}$$

If P and Q are deformed into P' and Q' of coordinates (x_1', x_2', x_3') and $(x_1'+dx_1', x_2'+dx_2', x_3'+dx_3')$ the square of the length ds of the new vector $\mathbf{P'Q'}$ is written

$$ds^2 = \delta_{ij} dx'_i \, dx'_j \tag{C-7}$$

From (C-2) we can write that

$$dx'_i = \frac{\partial f_i}{\partial x_1} dx_1 + \frac{\partial f_i}{\partial x_2} dx_2 + \frac{\partial f_i}{\partial x_3} dx_3 \tag{C-8}$$

And from (C-3) we can write that

$$dx_i = \frac{\partial g_i}{\partial x_1'} dx_1' + \frac{\partial g_i}{\partial x_2'} dx_2' + \frac{\partial g_i}{\partial x_3'} dx_3' \tag{C-9}$$

As a consequence the difference between the squared lengths can be expressed as

$$ds^2 - ds_0^2 = (\delta_{\alpha\beta} \frac{\partial f_\alpha}{\partial x_i} \frac{\partial f_\beta}{\partial x_j} - \delta_{ij}) dx_i dx_j \tag{C-10}$$

Or

$$ds^2 - ds_0^2 = (\delta_{ij} - \delta_{\alpha\beta} \frac{\partial f_\alpha}{\partial x_i} \frac{\partial f_\beta}{\partial x_j}) dx_i' dx_j' \tag{C-11}$$

The strain tensor is defined as

$$E_{ij} = (\delta_{\alpha\beta} \frac{\partial f_\alpha}{\partial x_i} \frac{\partial f_\beta}{\partial x_j} - \delta_{ij}) \tag{C-12}$$

or

$$e_{ij} = (\delta_{ij} - \delta_{\alpha\beta} \frac{\partial f_\alpha}{\partial x_i} \frac{\partial f_\beta}{\partial x_j}) \tag{C-13}$$

So that

$$ds^2 - ds_0{}^2 = 2E_{ij} dx_i dx_j \tag{C-14}$$

or

$$ds^2 - ds_0{}^2 = 2e_{ij} dx_i dx_j \tag{C-15}$$

The strain tensor E_{ij} was introduced by Green and St Venant and is called Green's strain tensor. The strain tensor. e_{ij} has been introduced by Cauchy for infinitesimal strains and by Almansi and Hamel for finite strains and is known as Almansi's strain tensor. In analogy with terminology in hydrodynamics, Eij is known as Lagrangien and eij as Eulerian. Both of them are symmetric.

If the components of the displacement are such that their first derivatives are so small that the squares and product of the partial derivatives of u_i are negligible compared with the first order terms, then e_{ij} reduces to Cauchy infinitesimal strain tensor

$$\varepsilon_{ij} \approx \frac{1}{2} (\frac{\partial u_i}{\partial_j} + \frac{\partial u_j}{\partial_i}) \tag{C-16}$$

In the infinitesimal displacement case, the distinction between the Lagrangien and Eulerian strain tensors disappears.

References

[1] J. Ophir, I. Césepedes, H. Ponnekanti, Y. Yazdi, and X. LI, "Elastography: a quantitative method for imaging the elasticity of bilogical tissues," *Ultrasonic Imaging*, vol. 13, n. 111-134, 1991.

[2] L. N. Bohs and G. E. Trahey, "A novel method for angle independent ultrasonic imaging of blood flow and tissue motion," *IEEE Transactions on Biomedical Engineering*, vol. 38, n. 3, pp. 280-286, 1991.

[3] S. Langeland, J. D'Hooge, H. Torp, B. Bijnens, and P. Suetens, "Comparison of time-domain displacement estimators for two-dimensional RF tracking," *Ultrasound in Medecine and Biology*, vol. 29, n. 8, pp. 1177-1186, 2003.

[4] B. S. Ramamurthy and G. Trahey, "Potential and limitations of angle independent flow detection algorithm using radio frequency and detected echo signals," *Ultrasonic Imaging*, vol. 13, n. 252-268, 1991.

[5] S. Golemati, A. Sassano, J. Lever, A. A. Barath, S. Dhanjil, and A. N. Nicolaides, "Carotid artery wall motion estimated from B-mode ultrasound using region tracking and block mathcing," *Ultrasound in Medecine and Biology*, vol. 29, n. 3, pp. 387-399, 2003.

[6] Y. Zhu and T. J. THall, "A modified block matching method for real-time freehand strain imaging.," *Ultrasonic Imaging*, vol. 24, n. 161-176, 2002.

[7] M. Tanter, J. Bercoff, L. Sandrin, and M. Fink, "Ultrafast Compound Imaging for 2-D Motion Vector Estimation: Application to Transient Elastography," *IEEE Transactions on Ultrasonics, Ferroelectrics and Frequency Control*, vol. 49, n. 10, pp. 1363-1374, 2002.

[8] J. A. Jensen, "Directional velocity estimation using focusing along the flow direction I: theory and simulation," *IEEE Transactions on Ultrasonics, Ferroelectrics and Frequency Control*, vol. 50, n. 7, pp. 857-872, 2003.

[9] J. A. Jensen and R. Bjenrgaard, "Directional velocity estimation using focusing along the flow direction II: experimental investigation," *IEEE Transactions on Ultrasonics, Ferroelectrics and Frequency Control*, vol. 50, n. 7, pp. 873-880, 2003.

[10] B. K. P. Horn and B. G. Shunck, "Determining optical flow," *Artificial intelligence*, vol. 17, n. 185-203, 1981.

[11] J. A. Jensen and P. Munk, "A new method for estimation of velocity vectors," *IEEE Transactions on Ultrasonics, Ferroelectrics and Frequency Control*, vol. 45, n. 3, pp. 837-851, 1998.

[12] X. Chen, M. J. Zohdy, E. SY, and M. O'Donnell, "Lateral speckle tracking using synthetic lateral phase," *IEEE Transactions on Ultrasonics, Ferroelectrics and Frequency Control*, vol. 51, n. 5, pp. 540-550, 2004.

[13] P. M. Morse and K. I. Ingard, *Theoretical Acoustics*. New-York: Mc Graw Hill, 1968.

[14] M. Fink, "Time reversal of ultrasonic fields--I: Basic principles," *IEEE Transactions on Ultrasonics, Ferroelectrics, and Frequency Control*, vol. 39, n. 5, pp. 555-566, 1992.

[15] J. W. Goodman, *Introduction to Fourier optics*. New York: McGraw-Hill, 1968.

[16] J. A. Jensen, "Field: A Program for Simulating Ultrasound Systems," *Medical & Biological Engineering & Computing*, vol. 34, n. Supplement 1, Part 1, pp. 351-353, 1996.

[17] A. Pesavento, C. Perrey, M. Krueger, and H. Ermert, "A time-efficient and accurate strain estimation concept for ultrasonic elastography using iterative phase zero estimation," *IEEE Transactions on Ultrasonics, Ferroelectrics and Frequency Control*, vol. 46, n. 5, pp. 1057-1067, 1999.
[18] M. E. Anderson, "A heterodyning demodulation technique for spatial quadrature," presented at Ultrasonics symposium, San Juan, Puerto Rico, 2000.
[19] J. A. Jensen, O. Holm, L. J. Jensen, H. Bendsen, S. Nikolov, B. G. Tomov, P. Munk, M. Hansen, K. Salomonsen, J. Hansen, K. Gormsen, H. M. Pedersen, and K. L. Gammelmark, "Ultrasound research scanner for real-time synthetic aperture data acquisition," *IEEE Transactions on Ultrasonics, Ferroelectrics and Frequency Control*, vol. 52, n. 5, pp. 881-891, 2005.
[20] J. Fromageau, E. Brusseau, D. Vray, G. Gimenez, and P. Delachartre, "Characterization of PVA cryogel for intravascular ultrasound elasticity imaging," *IEEE Transactions on Ultrasonics, Ferroelectrics and Frequency Control*, vol. 50, n. 10, pp. 1318-1324, 2003.
[21] N. Nitta and T. Shina, "A method of tissue estimation based on three-dimensional displacement vector," *Japanese Journal of Applied Physics*, vol. 39, n. 3225-3229, 2000.
[22] P. E. Barbone and J. C. Bamber, "Quantitative elasticity imaging: What can and cannot be inferred from strain images," *Physics in Medicine and Biology*, vol. 47, n. 12, pp. 2147-2164, 2002.
[23] O. Bonnefous, "Measurment of the complete (3D) velocity vector of blood flows," *IEEE Ultrasonics symposium*, n. 795-799, 1988.
[24] J. A. Jensen, "Algorithms for estimating blood velocities using ultrasound," *Ultrasonics*, vol. 38, n. 1-8, pp. 358-362, 2000.
[25] I. A. Hein and W. O' Brien, "Current Time-domain methods for assessing tissue motion by analysis from reflected ultrasound echoes," *IEEE Transactions on Ultrasonics, Ferroelectrics and Frequency Control*, vol. 40, n. 2, pp. 84-102, 1993.
[26] F. Yeung, S. F. Levinson, and K. J. Parker, "Multilevel and motion model-based ultrasonic speckle tracking algorithms," *Ultrasound in Medecine and Biology*, vol. 24, n. 3, pp. 427-441, 1998.
[27] R. F. Wagner, S. W. Smith, J. M. Sandrik, and H. Lopez, "Statistics of speckle in ultrasound B-scans," *IEEE Transactions on Sonics and Ultrasonics*, vol. 30, n. 3, pp. 156-163, 1983.
[28] C. Stiller and J. Konrad, "Estimating motion in image sequences, a tutorial on modeling and computation of 2D motion," *IEEE Signal Processing Magazine*, vol. 16, n. 4, pp. 70-91, 1999.
[29] R. L. Maurice, J. Ohayon, Y. Fretigny, M. Bertrand, G. Soulez, and G. Cloutier, "Noninvasive vascular elastography: theoretical framework," *Medical Imaging, IEEE Transaction on*, vol. 23, n. 2, pp. 164-180, 2004.
[30] D. P. Shattuck, M. D. Weinshenker, S. W. Smith, and O. T. von Ramm, "Explososcan: a parallel processing technique for high speed ultrasound imaging with linear phase arrays.," *Journal of the Acoustical Society of America*, vol. 75, n. 4, pp. 1273-1282, 1984.
[31] L. N. Bohs, S. C. Gebhart, M. E. Anderson, B. J. Geiman, and G. E. Trahey, "2-D motion estimation using two parallel receive beams," *IEEE Transactions on Ultrasonics, Ferroelectrics, and Frequency Control*, vol. 48, n. 2, pp. 392-408, 2001.
[32] E. Konofagou and J. Ophir, "A new elastographic method for estimation and imaging of lateral displacements, lateral strains, corrected axial strains and Poisson's ratios in tissues," *Ultrasound in Medicine and Biology*, vol. 24, n. 8, pp. 1183-99, 1998.

[33] B. J. Geiman, L. N. Bohs, M. Anderson, S. M. Breit, and G. Trahey, "A novel interpolation strategy for estimating subsample speckle motion," *Physics in Medicine and Biology*, vol. 45, n. 1541-1552, 2000.
[34] A. Giachetti, "Matching techniques to compute image motion," *Image and Vision Computing*, vol. 18, n. 247-260, 2000.
[35] Y.-S. Chen, Y.-P. Hung, and C.-S. Fuh, "Fast block matching algorithm based on the winner-update strategy," *IEEE Transactions on Image Processing*, vol. 10, n. 8, pp. 1212-1222, 2001.
[36] M. D. Fox, "Multiple crossed-beam ultrasound doppled velocimetry," *IEEE Transactions on Sonics and Ultrasonics*, vol. SU-25, n. 5, pp. 281-286, 1978.
[37] N. Nitta and T. Shina, "Real-time three dimensional velocity vector measurement using the weighted phase gradient method.," *Japanese Journal of Applied Physics*, vol. 37, n. 3058-3063, 1998.
[38] J. A. Jensen, "Vector velocity estimation in synthetic aperture flow and B-mode imaging," presented at IEEE International Symposium on Biomedical Imaging, Arlington, VA, USA.l, 2004.
[39] G. E. Mailloux, F. Langlois, P. Simard, and M. Bertrand, "Restoration of the velocity field of the heart from two-dimensional echocardiograms," *Medical Imaging, IEEE Transaction on*, vol. 8, n. 2, pp. 143-153, 1989.
[40] M. Anderson, "Multi-dimensional velocity estimation with ultrasound using spatial quadrature," *IEEE Transactions on Ultrasonics, Ferroelectrics and Frequency Control*, vol. 45, n. 3, pp. 852-861, 1998.
[41] J. A. Jensen, "A new estimator for vectory velocity estimation," *IEEE Transactions on Ultrasonics, Ferroelectrics, and Frequency Control*, vol. 48, n. 4, pp. 886-894, 2001.
[42] J. Udesen and J. A. Jensen, "Experimental investigation of transverse flow estimation using transverse oscillation," presented at 2003 IEEE Ultrasonics Symposium - Proceedings, Oct 5-8 2003, Honolulu, HI, United States, 2003.
[43] J. Udesen and J. A. Jensen, "An in-vivo investigation of transverse flow estimation," presented at Medical Imaging 2004 - Ultrasonic Imaging and Signal Processing, Feb 18-19 2004, San Diego, CA, United States, 2004.
[44] J. J. Wild and J. M. Reid, "Application of echo-ranging techniques to the determination of structure of biological tissues.," *Science.*, vol. 115, n. pp 226-230, 1952.
[45] J. A. Jensen, *Estimation of blood velocities using ultrasound. A signal processing approach*. New York: Cambridge University Press, 1996.
[46] C. M. Sehgal and J. F. Greenleaf, "Diffraction of ultrasound by soft tissues: the inhomogeneous continuous model.," presented at Acoustical Imaging Volume 13 (Proceedings of the Thirteenth International Symposium on Acoustical Imaging). Minneapolis, MN, USA, 1984.
[47] J. C. Bamber and R. J. Dickinson, "Ultrasonic B-scanning : a computer simulation," *Physics in medicine and biology*, vol. 25, n. 3, pp. 463-479, 1980.
[48] P. Shankar, "A general statistical model for ultrasonic backscattering from tissues," *IEEE Transactions on Ultrasonics, Ferroelectrics and Frequency Control*, vol. 47, n. 3, pp. 727-736, 2000.
[49] K. Ranganathan and W. F. Walker, "A novel beamformer design method for medical ultrasound. Part I: theory," *IEEE Transactions on Ultrasonics, Ferroelectrics and Frequency Control*, vol. 50, n. 1, pp. 15-24, 2003.
[50] G. R. Lockwood, J. R. Talman, and S. S. Brunke, "Real-time 3-D ultrasound imaging using sparse synthetic aperture beamforming," *Ultrasonics, Ferroelectrics and Frequency Control, IEEE Transactions on*, vol. 45, n. 4, pp. 980-988, 1998.

[51] J. A. Jensen, "Simulation of advanced ultrasound systems using field II," presented at 2004 2nd IEEE International Symposium on Biomedical Imaging: Macro to Nano, Apr 15-18 2004, Arlington, VA, United States, 2004.
[52] J. A. Jensen and N. B. Svendsen, "Calculation of pressure fields from arbitrarily shaped, apodized and excited ultrasound transducers," *IEEE Transactions on Ultrasonics, Ferroelectrics and Frequency Control*, vol. 39, n. 2, pp. 262-267, 1992.
[53] J.A. Jensen: Linear description of ultrasound imaging systems, Notes for the International Summer School on Advanced Ultrasound Imaging, Technical University of Denmark July 5 to July 9, 1999, Technical University of Denmark, June, 1999.
[54] K. Ranganathan and W. F. Walker, "A novel beamformer design method for medical ultrasound. Part II: simulation," *Ultrasonics, Ferroelectrics and Frequency Control, IEEE Transactions on*, vol. 50, n. 1, pp. 25-39, 2003.
[55] P. Munk and J. A. Jensen, "Improved beamforming performance using pulsed plane wave decomposition," presented at 2000 IEEE Ultrasonics Symposium, Oct 22-25 2000, San Juan, 2000.
[56] J. T. Ylitalo and H. Ermert, "Ultrasound synthetic aperture imaging: monostatic approach," *IEEE Transactions on Ultrasonics, Ferroelectrics, and Frequency Control*, vol. 41, n. 3, pp. 333-339, 1994.
[57] F. Gran and J. A. Jensen, "Multi element synthetic aperture transmission using a frequency division approach," presented at 2003 IEEE Ultrasonics Symposium - Proceedings, Oct 5-8 2003, Honolulu, HI, United States, 2003.
[58] M. Soumekh, "Bistatic synthetic aperture radar inversion with application in dynamic object imaging," *IEEE Transactions on Signal Processing*, vol. 39, n. 9, pp. 2044-2055, 1991.
[59] M. Soumekh, "A system model and inversion for synthetic aperture radar imaging," *IEEE Transactions of Image Processing*, vol. 1, n. 1, pp. 64-76, 1992.
[60] P. Stepanishen, "The time-dependent force and radiation impedence of a piston in a rigid infinite planar baffle.," *J. Acoust. Soc. Am.*, vol. 49, n. 3 pt 2, pp. 841-9, 1971.
[61] G. E. Tupholme, "Generation of acoustic pulses by baffled plane pistons," *Mathematika*, vol. 16, n. 209-224, 1969.
[62] J. Fromageau and P. Delachartre, "Description of a new strain and displacement estimator for elastography," presented at 2003 IEEE Ultrasonics Symposium - Proceedings, Oct 5-8 2003, Honolulu, HI, United States, 2003.
[63] P. M. Shankar and V. L. Newhouse, "Speckle reduction with improved resolution in ultrasound images.," *IEEE Transactions on Sonics and Ultrasonics*, vol. SU-32, n. 4, pp. 537-543, 1985.
[64] P. Delachartre, H. Liebgott, S. Michelet, M. Pernot, and D. Vray, "Hardware implementation for receive beamforming and transverse elasticity imaging," presented at 2004 IEEE Ultrasonics Symposium - Proceedings, Aug 24-27 2004, Montreal, Canada, 2004.
[65] J. A. Jensen, O. Holm, L. J. Jensen, H. Bendsen, H. M. Pedersen, K. Salomonsen, J. Hansen, and S. Nikolov, "Experimental ultrasound system for real-time synthetic imaging," presented at Ultrasonics symposium, Lake Tahoe, USA., 1999.
[66] M. J. Gordon, K. C. Chu, A. Margaritis, A. J. Martin, C. R. Ethier, and B. K. Rutt, "Measurement of Gd-DTPA diffusion through PVA hydrogel using MR imaging," *Biotechnology And Bioengineering*, vol. 65, n. 476-484, 1999.
[67] Y. C. Fung, *Biomechanics: Mechanical Properties of Living Tissues,* New York, Springer-Verlag, 1993.

Publications

Hervé Liebgott, Jérémie Fromageau, Jens E. Wilhjelm, Didier Vray and Philippe Delachartre,"*Beamforming scheme for 2D displacement estimation in ultrasound imaging*", EURASIP Journal on Applied Signal Processing, 2005, vol 8, pp 1212-1220.

Philippe Delachartre, **Hervé Liebgott**, François Lacouture, Fabrice Morestin, Andrej Lyshchik, Tatsuya Higashi, Ryo Asato, *« Modélisation bilinéaire et estimation du déplacement pour l'imagerie de l'élasticité appliquée au cancer de la thyroïde »,* to be published in the french journal, Traitement du Signal for a special issue on cancer.

International conferences with proceedings

Walid Aoudi, **Hervé Liebgott**, Andrew Needles, Victor Yang, Stuart Foster, Didier Vray, *« Estimation 3D du flux sanguin par imagerie ultrasonore haute fréquence : application à l'étude de la microcirculation »,* GRETSI 2005, Louvin la Neuve, (BELGIUM), September 2005.

Walid Aoudi, **Hervé Liebgott**, Andrew Needles, Victor Yang, Stuart Foster, Didier Vray, *« Estimation methods for flow imaging with high frequency ultrasound»,* WCU 2005, Beijing, (CHINA), August 2005.

Ghada Saïd, Didier Vray, **Hervé Liebgott**, Jérémie Fromageau, Elisabeth Brusseau, Olivier Basset, "*Young modulus imaging based on axial and lateral strain estimation from ultrasound data using a standard linear probe*" Proceedings of SPIE Medical Imaging meeting, Ultrasonic Imaging and Signal Processing, San Diego (USA), February 2005.

Hervé Liebgott, Jérémie Fromageau, Jens E. Wilhjelm, Didier Vray and Philippe Delachartre, *"Direct estimation of the lateral strain field using a double oscillating point spread function with a scaling factor estimator*", Proceedings of SPIE Medical Imaging meeting, Ultrasonic Imaging and Signal Processing, San Diego (USA), February 2004, vol. 5, N° 27, pp 163-172

Philippe Delachartre, **Hervé Liebgott**, Sylvain Michelet, Mathieu Pernot and Didier Vray, "*Hardware implementation for receive beamforming and transverse elasticity imaging*", Proceedings of The IEEE Ultrasonics Symposium, Montréal (CANADA), August 2004.

Arnaud Jarrot, **Hervé Liebgott**, Philippe Delachartre and Marc C. Robini, *"Edge-Preserving Image Reconstruction for Young's Modulus Recovery from Ultrasonic Data"* Proceedings of The IEEE Ultrasonics Symposium, Honolulu, (USA), October 2003, pp. 1919-1922.

Jérémie Fromageau **Hervé Liebgott**., Elisabeth Brusseau, Gérard Gimenez., Philippe Delachartre , Didier Vray, *"Correction of stress decay in intravascular elastography by*

combination of radial and tangential strain", Proceedings of The IEEE Ultrasonics Symposium,, Munchen (GERMANY), October 2002:1877-1880.

International conferences without proceedings

Jérémie Fromageau, **Hervé Liebgott**, Elisabeth Brusseau and Philippe Delachartre. *"Description of a new iterative algorithm for scaling factor estimation* Third International Conference on the Ultrasonic Measurement and Imaging of Tissue Elasticity, Lake Windermere, (UNITED KINGDOM), October, 2004

National conferences without proceedings

Hervé Liebgott, Jens E. Wilhjelm, Didier Vray, Philippe Delachartre, *"Contrôle dynamique d'une forme d'onde pour l'imagerie de l'élasticité par échographie"*, Nouvelles Formes d'Ondes en Imagerie, Localisation et Communication, Paris (FRANCE), March 2005.